ABSTRACT

Title of Document: UNCERTAINTY IN PYROLYSIS MODELING: PARAMETERS ESTIMATION AND UNDTEADY CONDITIONS

Zohreh Ghorbani
Master of Science, 2013

Directed By: Professor Arnaud Trouve
Department of Aerospace Engineering

Flammability of composite materials represents one of the major bottlenecks in Aviation industry. PVC as a representative charring material and PMMA as a representative non-charring material were considered for this study. The predictive capability of pyrolysis models developed via a calibrated semi-empirical approach is examined through a series of numerical experiments. These configurations feature conditions that are significantly different from the reference conditions used in the model calibration phase. It is found that the domain of validity of semi-empirical pyrolysis models is limited to the conditions that were used during model calibration and that extrapolation to non-calibrated conditions results in a significant error. To further examine the uncertainty in pyrolysis modeling, the effect of unsteady incident radiant heat flux was considered. Results indicate that in a time-average sense, the oscillation in the incoming heat flux does not affect the rate of formation of flammable vapor. However, the timeline analysis of charring and non-charring materials response shows quite different trends.

UNCERTAINTY IN PYROLYSIS MODELING: PARAMETER ESTIMATIONS AND UNDTEADY CONDITIONS

By

Zohreh Ghorbani

Thesis submitted to the Faculty of the Graduate School of the
University of Maryland, College Park, in partial fulfillment
of the requirements for the degree of
Master of Science
2013

Advisory Committee:
Professor Arnaud Trouve, Chair
Professor James Baeder
Professor Stanislav Stoliarov

Table of Contents

List of Tables

List of Figures

Chapter 1 : Introduction

This section will discuss the motivation for this research and the application to the field of Aerospace Engineering.

1.1 Application of composites in aircraft

Over the past 60 years, there has been a sharp increase in the use of polymer matrix composites in high-technology applications, including the aviation industry. Modern aircrafts utilize several tons of plastics for cabin interior components due to their many outstanding physical, chemical and mechanical properties. Key advantages of composite materials over metal alloys include low weight, customizable material properties, high specific stiffness and specific strength, excellent corrosion resistance, outstanding thermal insulation, low thermal expansion and easy processability. This translates into expanded opportunities for substitution of metal, such as steel and aluminum alloy, in the aviation industry to reduce weight and fuel consumption.

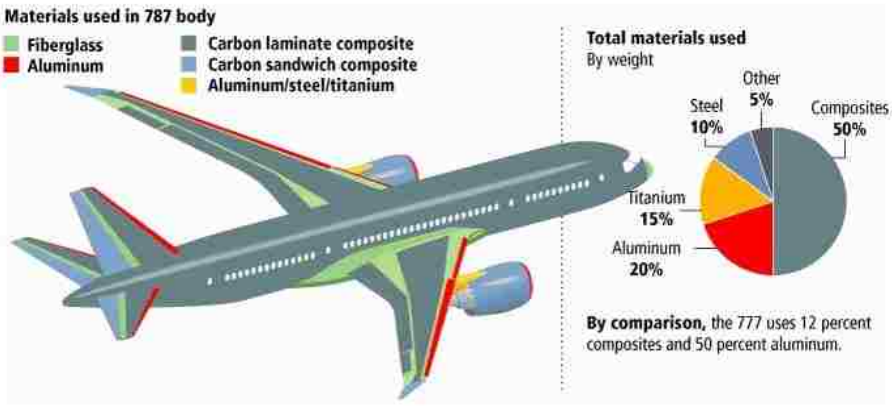

Figure 1-1. Usage of various materials in the Boeing 787 [1].

The level of advanced composite usage in large commercial transports has been increasing in recent years. For example, the usage of composite materials in the Boeing 777 (1995) structure was roughly 12% composite material by weight, and in the Boeing 787 (2011), shown in figure 1.1, it increased to 50% composite material

[1]. Figure 1.2 shows the growth of composite usage in large civil aircrafts, military aircrafts and helicopters. Application of these new polymer-based materials is the most promising long-term prospect for energy conservation and emission reduction in transportation vehicles.

There are a wide range of composite materials used in aircraft. The two most common composite are: glass fiber/phenolic resin and carbon fiber/epoxy resin. Glass reinforced phenolic composites are mainly used in aircraft cabins either as a single skin laminate or a sandwich material. Phenolic composites account for 80-90% of the interior furnishings of aircraft, e.g., ceiling panels, wall panels, cabinet walls, etc. [3-4]. Carbon reinforced epoxy composites are used mainly in wing and tail components, control surfaces, landing gear door, etc. Most types of carbon/epoxy laminates used in aircraft structures are flammable and pose a serious fire hazard [5].

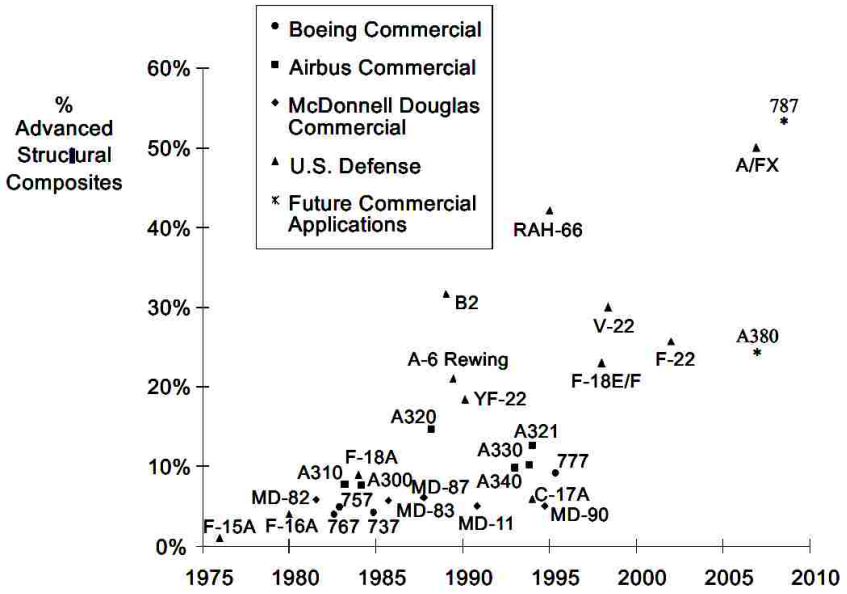

Figure 1-2. Growth in use of composite by weight in aviation industry [2].

Composite materials are essentially plastics that are reinforced with carbon fibers. A major disadvantage associated with the widespread use of polymers is their inherent flammability. Most polymers contain a large fraction of carbon and hydrogen atoms, which makes their composition similar to fossil fuels. At high value of temperature, typically above 400ºC, the composite material decomposes and

contributes to the generation of heat, smoke, and toxic volatiles. The flammability of composite material in the cabin interior is a concern and improvements to flammability standards were deemed necessary by the Federal Aviation Administration (FAA) [3-4]. The flame-retardant research community responded to these concerns by mounting an effort to develop flame-resistant composites using flame-retardant additives [4, 6]. Flame retardant epoxies are extensively used increasingly in carbon-fiber composite aircraft structures. Figure 1.2 shows the approximate cost of commercial plastic used in aviation industry versus flammability. Flammability, which generally refers to the ability of a substance to ignite and burn rapidly during an exposure to fire, is an indicator of fire hazard; lower flammability value attributes to better fire performance. As it is illustrated in figure 1.3, the price of commercial plastic is inversely proportional with their flammability. It is apparent that many resin systems, despite their outstanding fire performance, i.e. low flammability value, are expensive. In addition, the processability of most of the flame retardant polymers are difficult due to the highly viscous nature of these materials [3, 8]. Moreover, their environmental durability is a concern. In Europe and the United States, a concerted political effort is being made to restrict or ban usage of many popular additives [6, 8].

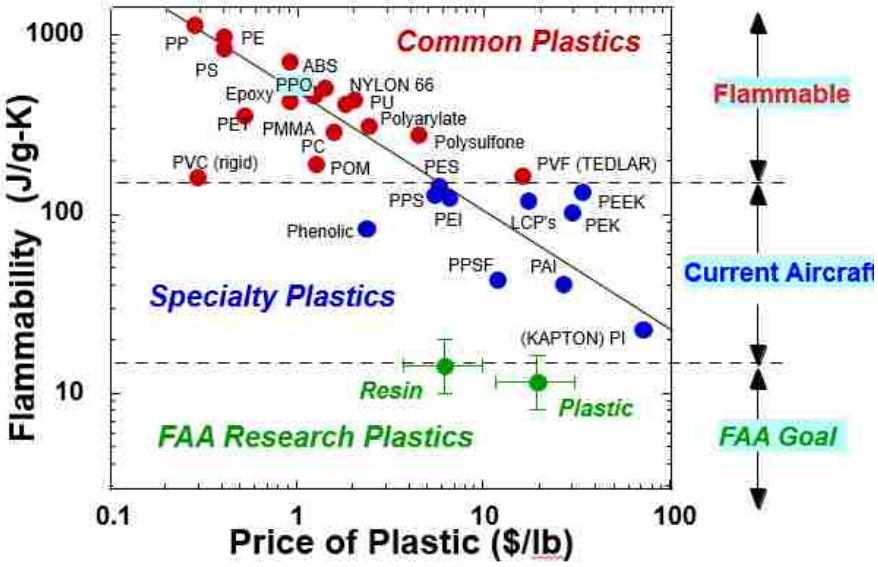

Figure 1-3. Flammability ranking by cost [9]

1.2 Aircraft fire hazard

The growing use of composite materials in aircrafts has the potential to increase the fire hazard due to the flammable nature of these materials. Life threatening aircraft cabin fires entail two distinct fire scenarios: (1) in- flight fires and (2) post-crash fires.

In-flight fires mostly occur in accessible areas such as the galley or toilet and are typically detected and extinguished promptly. On rare occasions in-flight fires originating in inaccessible areas become uncontrollable leading to aircraft fatalities [6, 10]. Post-crash fires involve survivable crashes where the structural integrity of the aircraft may be compromised by impact with the ground or another object before the initiation of a fire. In post-crash fires, the fire is initiated outside the cabin usually due to a fuel spill. The fire then penetrates into the aircraft cabin, generating heat, smoke and toxic decomposition products [6]. These fires are often uncontrollable and are further complicated by the disorientation and injury of passengers after the impact.

The growing use of composites in aircraft together with their flammable nature motivate the importance of understanding the behavior of these materials in fires to ensure passenger safety. To this end, strict fire safety regulations are enforced by the Federal Aviation Administration (FAA) on the use of materials inside aircraft cabin [3-4, 6-9]. The fire safety regulations for commercial aircraft required by FAA have been became more strict and demanding. In addition, the Fire Research Program was initiated by the FAA in 1993 with the ultimate goal of developing a fireproof aircraft cabin and eliminating burning cabin materials as a cause of death in aircraft accidents [4, 6-7]. The focus of the fire research program is on developing composites that can maintain survivable aircraft cabin conditions for at least 10 to 15 minutes in post-crash fuel fires in order to reduce fatalities by two-thirds since 40% of fatalities in aircraft accidents are due to the fire and smoke [6].

A substantial amount of experimental and theoretical studies have been performed over the past few decades to understand the behavior of composite polymers;

however significant gaps remain in the understanding of how these materials respond to fire. A key component to assess polymer flammability is to understand ways to increase thermal stability, which provides a path for making them non-combustible. This is a critical first step towards developing non-combustible polymeric aircraft materials, which would potentially save many lives in a post-crash fire situation.

1.2.1 Fire response characteristics of composites

In order to develop non-combustible aircraft materials, it is necessary to establish the relationship between the chemical structure of materials and the fire response parameters that provide a measure of fire hazard. Fire response parameters is the main indictors of the fire hazard associated with the composites polymers. Fire response parameters describe the flammability and combustion properties of a material during the early stages of fire, contributing to the growth of fire [3, 8]. The main fire response parameters include: time-to-ignition, heat release rate (HRR), flame spread rate, oxygen index, and toxicity of fire effluent.

Time-to-ignition may be defined as a time during which a combustible material can withstand exposure to an incident heat flux before igniting. The ignition time is often used as an approximate measure of the flammability resistance of a material. It is desirable to develop materials with long ignition times for design and manufacture of cargo interior and structural component of aircraft. The heat release rate (HRR) is defined as the amount of thermal energy released by a material that is exposed to a fire. HRR rate is a time dependent parameter, meaning its value varies with time as the burning material is being consumed. It is often expressed by average heat release rate and peak heat release rate. The peak heat release rate is an important parameter because it controls the maximum temperature and flame spread rate. It is noteworthy that materials with low values for peak and average release rates are more suitable in applications that require minimum spread and growth of fire [3, 8, 39].

The oxygen index may be defined as the minimum oxygen content required to sustain the combustion process of a material. Flame retardant materials have a high the oxygen index, meaning they have the potential to self-extinguish when the fire

becomes deprived of oxygen. The flame spread rate describes the rate of travel of a flame front over the surface of a combustible material. The flame spread characteristics of a material are obtained through a range of flame spread experiments; the gravitational and wind effects play an important role in the growth of fire [39].

Smoke density and gas toxicity are the concentration of smoke particles and fire effluents within the plume of a fire, respectively. The toxic gases that released during the burning of composites materials includes carbon monoxide, hydrogen chloride, dioxins, etc. Note that the production of smoke and toxic gases depends on chemical composition of the composite material, oxygen availability, heat intensity, etc. [8]. These two parameters have a major impact on the ability of humans to survive a fire and may contribute to long-term damages [3].

1.2.2 FAA fire safety regulations

Strict regulations prescribed in fire safety standards are enforced by the Federal Aviation Regulation (FAR) of the US Federal Aviation Administration (FAA) on materials used inside aircraft. The fire safety regulations for commercial aircraft required by FAA have been became more strict and demanding over the past few decades [6-8]. "For example, an early version of FAA regulations for non-metallic materials used in the pressurized cabins of aircraft required a peak heat release below 100 kW/m^2 and a total heat release of 100 kW/m^2. In 1990 the regulations were made more restrictive by reducing the peak and total allowable heat release values to 65 kW/m^2 as well as enforcing an upper limit on smoke density" [3].

All composite materials used inside the cargo of commercial aircraft that carry more than 19 passengers are required to comply with the fire testing regulation of Title 14 Code of Federal Regulations. There are several fire tests that are specified in FAR 25.853 in order to assess the flammability and fire performance of these materials [6-7]. The fire tests required by the FAA include: heat release, heat release rate, smoke density, ignition resistance, fire resistance, burning rate and flame spread [6]. The goal of FAA for mandating these tests is to delay the cabin flash-over and

consequently increase the escape time for passengers [3]. A detailed description of FAA regulations can be found in Ref [3, 7-8].

1.3 Material flammability assessment

The characteristic of fire scenarios is exponential growth which originates from the continued participation of surrounding materials as fuel in the fire event. In order to design safer aircraft and minimize the hazard associated with fire growth, a detailed understanding of the conjugate heat and mass transfer processes that define fire spread and the behavior of this material in fire is required. The assessment of material flammability could be done through a series of either experimental or numerical tests, and the results may be used for further improvement of material flammability and minimization of their fire growth.

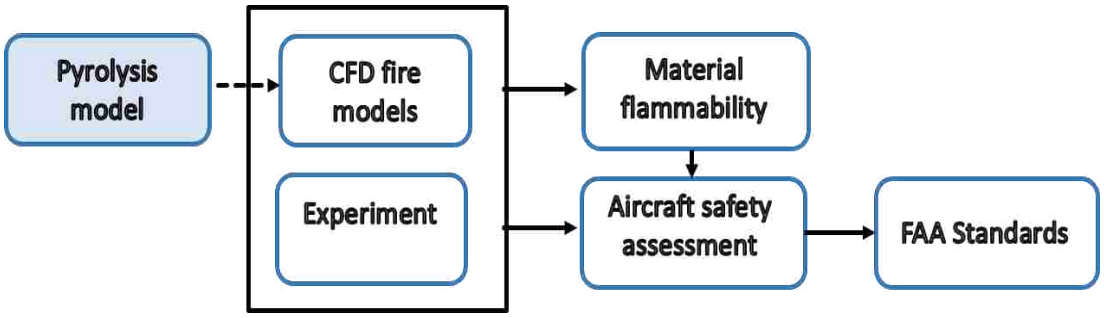

Figure 1-4. Diagram of potential material flammability assessment procedures.

Figure 1-5. Bench apparatuses adopted from Ref. [4, 6]: Cone calorimeter (left), and oxygen index (right)

1.3.1 Experimental assessments

Experimental techniques used to measure the fire response parameters of the polymers as described in section 1.2.1, range in size from bench-scale apparatuses for small specimens to full-scale tests for large structures. Some examples of bench-scale apparatuses are cone calorimeter (CC), fire propagation apparatus (FPA), thermo gravimetric analysis (TGA), differential scanning calorimetry (DSC), oxygen index, etc. [3-4, 6-8].

Bench scale apparatuses are widely used to determine the fire behavior of these materials, usually flame spread rate and ignitability, due to lower cost and simplicity of conducting the experiment. The data generated by such tests is then used to assess the fire performance properties of composite materials and their flammability. It is noteworthy that the test specimens are often not representative of real fire scenario conditions, and they generally ignore the effect of fire growth. Consequently, the fire performance of these materials could change in a real fire scenario. As a result, it is necessary to evaluate the performance of composites in the actual application, which includes intermediate-scale and full-scale fires [10, 12].

Figure 1-6. Post-crash fire simulation in a full-scale indoor fire test facility [11]

Figure 1-7. Full scale cabin mock up: development of Fire Test for Aircraft Seat Cushion [11]

The FAA fire research program conducted a series of full-scale in-flight and post-crash fire tests to examine the fire behavior of composite materials used in the cabin of commercial aircraft [3, 10, 12-13]. The fuselage of narrow-body Boeing 707 and McDonnell Douglas DC-10 were configured to perform a range of tests including cargo compartment fire, fuselage burn-through tests, seat flammability comparison, smoke detection, etc. The temperature measurements, heat flux, smoke levels, and gas sampling and combustion products were monitored during the experiment. Even though the full-scale fire tests provide a better understanding in assessment of the material flammability and fire growth in aircraft cabin, they are extremely expensive test to perform.

1.3.2 CFD-based fire modeling

The use Computational Fluid Dynamics (CFD)-based fire modeling is potentially useful to predict the fire response properties of material in the interior cabin together with their flame spread and fire growth behavior in real world geometries. It provides a cost-effective alternative to expensive full-scale fire tests. In addition, when it is not practical to perform full-scale fire testing due to size, CFD fire modeling is the best available tool to predict full-scale heat release rate of complex polymers and the rate of the flame spread. Using numerical simulator packages can also provide a fundamental understanding of material combustion and their behavior in fires.

Moreover, CFD-based fire modeling may be used in the process of forensic fire investigation and post-fire reconstruction. This would provide a tool to analyze an aircraft accident and understand how the fire may have evolved. Fire modeling can provide the progression of events during the course of a fire. This would assist in the analysis of evacuation processes and survivability of passengers, comparison of injuries to fire development, and possibility of egress.

CFD-based models designed to predict the flame spread and fire growth of a full-scale aircraft cargo fire require several sub-models for simulation of the gaseous phase and the condensed phase. Multiple sub-models are required because the spatial

and temporal scales required for accurate resolution of the condensed phase processes are different from those required for the processes that occurs in the gas phase.

Flame spread is a transient phenomenon, consists of interactions between the gas phase and the solid phase. During this process, the solid is subjected to an external heat flux, i.e. in the form of radiation coming from flames or another source at ignition. Under an external heat flux, the material undergoes degradation due to the rise in temperature. Thermal degradation begins at the surface, penetrating into the solid and causing the release of volatiles. These flammable gases flow out of the solid—due to pressure gradients generated at the pyrolysis zone—mix with air, and lead to a combustion process in the gas phase. More precisely, this process features a closed-loop heat feedback mechanism, where a large amount of heat is released during gaseous combustion and then transferred to the surrounding unburnt solid by radiation and convection ahead of the flame. That is, in return, producing more flammable gas during the pyrolysis of the solid, which burns and leads to a larger turbulent flame.

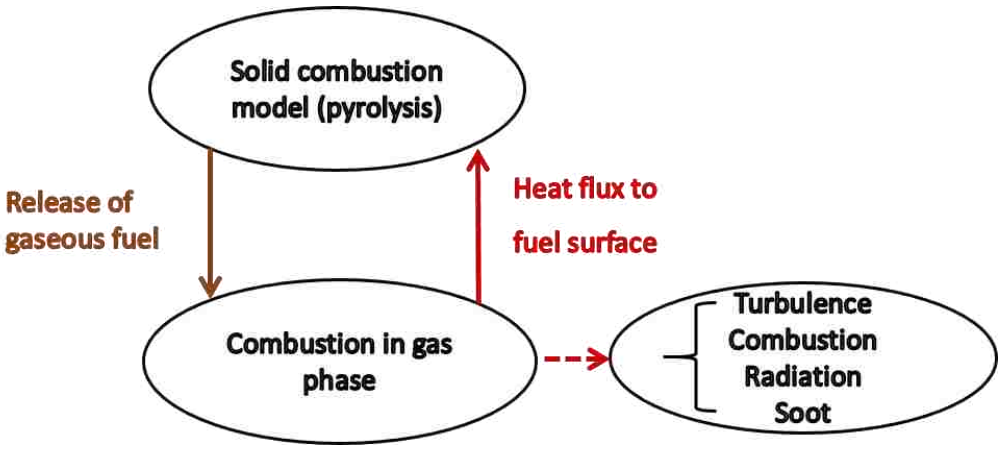

Figure 1-8. Schematic of sub-module for CFD-based fire modeling

Accurate modeling of flame spread and fire growth is an enormous task due to the complex underlying chemical and physical processes. Turbulence, gas-phase chemical reactions, radiative heat losses, and solid combustion sub-models need to be incorporated in an appropriate solver to properly represent the multi-physics phenomena taking place during the spread of the flame.

In many fire scenarios, solid materials make a substantial amount of the fuel loads. Understanding the processes involved in the pyrolysis of condensed phase fuels is important to characterize ignition, growth phase of fires, and the production rate of flammable vapor. The fuel release rate is the amount of gaseous fuel generated by thermal degradation of the solid material and determines in turn the intensity of the combustion process. Thus, a condensed phase pyrolysis sub-model that accurately predicts the temperature and volatiles release rate is essential for CFD-based fire modeling. The main focus of this work is on the solid phase combustion modeling.

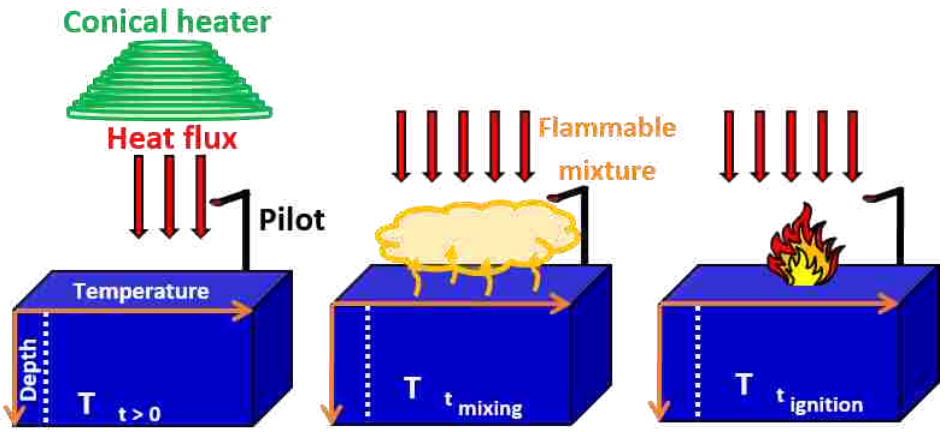

Figure 1-9. Pyrolysis of solid fuel sample.

1.3.2.1 Pyrolysis modeling

The burning process of a generic solid fuel sample is shown in figure 1.9. When the solid sample—initially at ambient temperature—is exposed to an external heat flux, the solid temperature begins to increases and its molecules are stimulated. The molecular bonds finally break-up, producing flammable gases. These pyrolysis gases leave the top surface due to pressure gradient generated at the pyrolysis zone and mix with the surrounding air to form a flammable mixture which moves upwards and ignites as it reaches the ignition source.

These are a range of phenomena that occurs during the pyrolysis process. The primary in-solid heat transfer process is heat conduction but in-depth radiation and heat convection are important. The chemical processes, i.e. decomposition and

oxidation chemical reactions that result in the production of gas/solid residues (char/ash) needs to be taken into account. The drying processes —in the case of solids with moisture— needs to be taken into account; in case of solids with an intermediate liquid state, e.g., polymers, featuring melting, bubble formation and bubble transport is important. Changes in the material porosity and permeability, swelling or shrinkage are also important. In addition, physical and geometrical changes, e.g., crack formation, changes in the material porosity and permeability, swelling or shrinkage are important.

A significant amount of experimental and theoretical studies have been conducted over the past few decades for the analysis and prediction of pyrolysis processes of charring and non-charring materials [14-22]. It is not the intent of the present study to give a thorough review on pyrolysis modeling, but a brief overview will be presented. Current pyrolysis models feature a variety of approaches and may be categorized into fully empirical, semi-empirical or comprehensive formulations. Fully empirical formulations prescribe the formation rate of flammable vapor based on data obtained in reference bench-scale or furniture calorimeter experiments. While fully empirical formulations offer the advantage of simplicity, they rely on the implicit assumption that conditions found in reference experiments are representative of those found in fire problems of interest. This assumption is generally incorrect and can lead to large errors [14]. On the other hand, comprehensive models consider detailed descriptions of physical and chemical processes as described in the previous section. Semi-empirical models correspond to an intermediate approach between the fully empirical and comprehensive model, and they rely on the dominant physical phenomena but neglect some of the physical processes that occurs during the condensed phase. They have the following distinguishing features: one-step finite-rate pyrolysis chemistry instead of detailed multi-step chemistry; single-phase homogeneous medium; constant material properties, one-dimensional treatment of degradation process; and neglecting the in-depth radiation and gas transport effects. In addition, material properties and chemical parameters are considered model parameters rather than "true" properties and are calibrated against reference micro-scale/bench-scale tests.

The semi-empirical modes are the dominant approach adopted in CFD-based fire modeling. Semi-empirical models will be discussed in more detail in Chapter 2.

1.4 Objectives and thesis organization

This thesis is written in a manuscript format. As such, each chapter is a standalone document suitable for a journal publication. An introduction of each paper is presented as follows:

1.4.1 Chapter 2

This chapter was published in the Fire Safety Journal [40]. The predictive capability of pyrolysis models developed via a calibrated semi-empirical approach was examined. Detailed pyrolysis models require a large number of input parameters, including chemical kinetic parameters for each pyrolysis reaction, thermal diffusion properties for each chemical species (virgin, char and intermediate species), and thermal radiation properties of the solid. In general, there are two different approaches to determine material pyrolysis properties: 1) measure individual material pyrolysis properties using specialized laboratory instruments such as thermo gravimetric analysis (TGA), differential scanning calorimetry (DSC), etc. 2) obtain the required properties from the Cone Calorimeter (CC), fire propagation apparatus (FPA), or similar experiments using optimization [23, 25-27]. Measuring the pyrolysis parameters should be the best way to determine the set of model inputs, however with this approach it is not feasible to measure all properties (e.g. intermediate species) or to measure some parameters due to material, structure, or heating-rate issues. Thus, optimization techniques remain an inherent part of obtaining material properties of the solid phase combustion [26]. In general, the pyrolysis model parameters are determined by finding the optimum agreement between the estimated model outputs (mass-loss rate, front surface temperature, and back wall surface temperature) and the equivalent experimental value obtained from Cone Calorimeter (CC) or fire propagation apparatus (FP).

For this study we chose to examine polyvinyl chloride (PVC) as a representative charring material and six different semi-empirical models were developed to simulate pyrolysis of PVC. The study then considered an evaluation of the predictive capability of the six pyrolysis models through a series of numerical experiments, including several cone calorimeter tests and one vertical upward flame spread problem; these configurations feature conditions that are significantly different from the reference conditions used in the model calibration phase. It is found that predictions from the PVC pyrolysis models start to diverge for conditions that lie outside of the calibration range. Most notably, the models lead to conflicting results when applied to a flame spread problem. These results suggest that the domain of validity of semi-empirical pyrolysis models is limited to the conditions that were used during model calibration and that extrapolation to non-calibrated conditions may result in a significant loss of accuracy.

1.4.2 Chapter 3

This chapter will be submitted to Fire Safety Journal; a previous version has been presented at 8th US National Meeting. The effect of time dependent irradiation on pyrolysis processes was examined. Recent experimental and numerical studies on pyrolysis processes have focused only on a constant incoming heat flux. However, in most fire scenarios, the flame grows in size and becomes turbulent. The turbulent gaseous flow, is characterized by random, fluctuating movements and consists of eddies of differing time and length scales. The influence of these turbulent fluctuations on radiative heat flux is pronounced and consequently the gas-to-solid rate of heat transfer features strong unsteady variations. The thermal feedback from the flame is the driving mechanism of the pyrolysis process. As a result, the pyrolysis process takes place in a strongly unsteady environment. This aspect is usually overlooked in experimental, theoretical, or numerical analysis in which a quasi-steady point of view is often adopted.

In the present study, the effect of fluctuating incident radiant heat exposure on the pyrolysis processes was examined. We chose to examine polymethyl methacrylate

(PMMA) and polyvinyl chloride (PVC). The pyrolysis model developed for this study allows for sample shrinkage or swelling and constant or time-varying radiant exposures. A mathematical solution to a reference analog problem corresponding to heat conduction in a semi-infinite solid, thermally loaded by an unsteady heat flux, is used as the basis for data analysis. The analytical model was further modified to predict the amplitude of temperature and mass loss rate fluctuations for time dependent radiant exposure. The response of the PMMA and PVC samples under harmonic periodic variations in irradiation was analyzed in terms of the amplitude of the fluctuations in both solid temperature and fuel mass loss rate. It was found that the response of charring and non-charring materials is quite different. In the case of PMMA, the effects of time-varying radiant exposure are pronounced during the entire pyrolysis process, from ignition to burn-out. In contrast, in the case of PVC, the effects of time-varying radiant exposure are only pronounced during a limited time. This limited time corresponds to a regime in which the pyrolysis front is within a certain spatial distance of the exposed surface of the material. The analysis leads to an evaluation of the importance of unsteady heat flux effects on pyrolysis processes.

Chapter 2 : Limitations in the Predictive Capability of Pyrolysis Models Based on a Calibrated Semi-Empirical Approach

2.1 Summary

Pyrolysis models used in Computational-Fluid-Dynamics-based fire models are typically semi-empirical, include a large number of unknown parameters (i.e., material properties and parameters of the chemical reactions) and require a careful calibration phase. During the calibration phase, the pyrolysis model coefficients are determined by comparisons with reference experimental data, for example data taken from thermo-gravimetric and/or bench-scale experiments. The present study examines the predictive capability of pyrolysis models developed via a calibrated semi-empirical approach. The study first introduces six different semi-empirical models developed to simulate pyrolysis of polyvinyl chloride (PVC). All of the models are similar and use a global one-step Arrhenius-type pyrolysis reaction. The models differ in assumptions made that impact the number of unknown model parameters and/or because of the optimization technique used to determine the unknown parameters (a genetic algorithm or a stochastic hill-climber algorithm). The six models are calibrated and, by design, provide similar results under conditions that are close to those of reference cone calorimeter experiments.

The study then considers an evaluation of the predictive capability of the six pyrolysis models through a series of numerical experiments, including several cone calorimeter tests and one vertical upward flame spread problem. These configurations feature conditions that are significantly different from the reference conditions used in the model calibration phase. It is found that predictions from the PVC pyrolysis models start to diverge for conditions that lie outside of the calibration range. Most notably, the models lead to conflicting results when applied to the flame spread problem. These results suggest that the domain of validity of semi-empirical pyrolysis

models is limited to the conditions that were used during model calibration and that extrapolation to non-calibrated conditions may result in a significant loss of accuracy.

2.2 Introduction

Pyrolysis models proposed to describe the thermal degradation of solid fuel sources and the associated rate of production of flammable vapors (i.e., the fuel mass loss rate) represent one of the major bottlenecks in fire modeling. Current pyrolysis models feature a variety of approaches and may be categorized into fully empirical, semi-empirical or comprehensive formulations. Fully empirical formulations prescribe the evolution of the fuel mass loss rate based on data obtained in reference bench-scale or furniture calorimeter experiments. While fully empirical formulations offer the advantage of simplicity (they conveniently bypass the need for a pyrolysis model), they rely on the implicit assumption that conditions found in reference experiments are representative of those found in fire problems of interest. This assumption is generally incorrect and can lead to large errors [14].

In contrast, comprehensive models consider detailed descriptions of the many physical and chemical processes that occur inside solid fuel sources in response to the gas-to-solid thermal loading [15-22], including: in-solid heat transfer processes (primarily heat conduction but also in-depth radiation and possibly heat convection); chemical processes (decomposition and/or oxidation chemical reactions) that result in the production of gas, liquids (tar) and solid residues (char, ash); drying processes (in case of solids with moisture); liquid phase processes (in case of solids with an intermediate liquid state, e.g., polymers featuring melting, bubble formation and bubble transport); physical and geometrical changes (e.g., crack formation, changes in the material porosity and permeability, swelling or shrinkage); etc. While comprehensive models offer the promise of a versatile and accurate treatment of pyrolysis, they require a fundamental understanding of the dominant processes involved, as well as suitable experimental and/or theoretical methods to evaluate the material properties and chemical parameters that are required in the detailed

mathematical formulation. To date, detailed comprehensive models are only available for a limited number of materials (primarily wood and plastic materials) [14-14, 18].

Semi-empirical models correspond to an intermediate approach based on simplified descriptions of in-solid heat transfer and chemical processes [21, 23-28]. Semi-empirical models are similar to comprehensive models to the extent that they are based on physics-based descriptions of in-solid heat transfer and chemical processes. However, they differ from comprehensive models and have the following distinguishing features: they emphasize cost-effectiveness rather than completeness and accuracy; they rely on a number of simplifications or assumptions (often due to knowledge gaps and because a comprehensive approach is simply not available); and they consider material properties and chemical parameters as model parameters (i.e., apparent properties) rather than "true" physical and chemical properties of the material. Examples of simplifications adopted in semi-empirical models include: the assumption of infinitely fast or global single-step pyrolysis chemistry (instead of detailed multi-step chemistry), the assumption of a single-phase homogeneous medium (instead of a multi-phase, multi-constituent treatment), or the assumption of a constant volume (instead of allowing for swelling or shrinkage). Model parameters (apparent properties) are determined through a careful calibration phase by comparisons with reference experimental data, for instance data coming from thermo-gravimetric and/or bench-scale experiments, and by error minimization algorithms based on advanced optimization techniques. Semi-empirical models correspond to the dominant approach adopted in Computational-Fluid-Dynamics-based (CFD-based) fire models.

It is worth pointing out that the exact limit between comprehensive and semi-empirical models remains difficult to define and that what may look to some as a comprehensive model may be considered by others as a sophisticated version of a semi-empirical model. We propose that the main criterion for a differentiation is whether the underlying physical and chemical properties (taken in totality or at least to a dominant fraction) may be considered as true or apparent properties of the

material, i.e. whether these properties have been directly measured or simply inferred from multi-physics calibration tests.

While semi-empirical formulations provide an attractive solution to the problem of treating pyrolysis in CFD-based fire simulations, it is worth emphasizing that their domain of validity remains typically unspecified. First, while by construction, semi-empirical pyrolysis models are expected to be accurate for conditions close to those used during model calibration, there is no guarantee that they will remain accurate for conditions that lie outside of the calibration range. This guarantee exists in comprehensive models but is lost in semi-empirical models because of the built-in simplifications and use of apparent properties. In addition, despite the importance of these choices, there is no established guideline on the nature, quality and completeness of the reference experimental data that are used during calibration. In fact, the literature features a wide variety of choices for calibration data, ranging from relying exclusively on data obtained in bench-scale experiments (e.g., cone calorimeter or fire propagation apparatus tests) to using data obtained in both bench-scale and micro-scale experiments (thermo-gravimetric analysis, differential scanning calorimetry, etc.). Additional choices for calibration data range from using data obtained in a limited set of bench-scale experiments, for instance experiments performed with high values of the radiant panel intensity (greater than 50 kW/m^2 - a typical value used to represent post-flashover compartment fires) to using data obtained in a larger set of bench-scale experiments featuring high and low values of the radiant panel intensity (including intensities below 25 kW/m^2 - a typical value used to represent flame spread). Choices also includes relying exclusively on fuel mass loss rate data from bench-scale tests versus using both mass loss rate and in-solid temperature data.

The general objective of the present study is to evaluate the predictive capability of semi-empirical pyrolysis models. We chose to examine polyvinyl chloride (PVC) as a representative charring material. We first introduce six different semi-empirical models developed to simulate PVC pyrolysis (Section 3); the six models use the same mathematical formulation but differ because of differences in the number of unknown

model parameters and/or because of differences in the values adopted for the unknown parameters; the six models are calibrated using cone calorimeter test data obtained at high values of the radiation intensity. Next, we present a comparison of predictions made by the six PVC pyrolysis models in a series of cone calorimeter tests and for conditions that are significantly different from those used during model calibration (Section 4). Finally, we present a similar comparison in CFD simulations of a laboratory-scale test corresponding to a vertical upward flame spread problem (Section 5).

2.3. PVC Pyrolysis Model

This section presents the development of six different (albeit similar) models to describe PVC pyrolysis. The development of these models is based on: (1) cone calorimeter test data borrowed from Ref. [22] (Section 3.1); (2) a standard one-dimensional model formulation to describe pyrolysis processes occurring inside the PVC material (Section 3.2) – the formulation features as many as 13 unknown parameters; and (3) a parameter estimation approach based on two optimization techniques (a genetic algorithm and a stochastic hill-climber algorithm) and detailed comparisons between model simulations and cone calorimeter test data (Section 3.3).

2.3.1 Cone calorimeter test data

Test data were obtained from Ref. [22]. The configuration is a classical air-supplied cone calorimeter set-up in which the top surface of horizontal samples of PVC were exposed to controlled levels of radiation intensity as provided by a calibrated radiant panel. PVC was obtained from HPG International and is produced under the trade name Versadur 150. The samples were 6 mm thick; the bottom surface of the samples was lined with a 20 mm thick dense Kaowool blanket which rested on top of a 13 mm thick Kaowool M board; the bottom and sides of each sample were wrapped with aluminum foil. The samples were subjected to piloted ignition conditions as provided by an electric pilot (spark) located near their exposed top surface.

The samples were observed to thermally degrade and gasify in response to the radiation loading and to eventually transition to flaming combustion. The levels of radiation intensity were constant in time; the experimental matrix included several tests corresponding to different levels of radiation intensity at 50, 75 and 92 kW/m^2 [22]. Experimental diagnostics included an oxygen consumption calorimetry system to provide information on the time variations of the oxygen depletion occurring inside the cone, i.e., a measure of the heat release rate (HRR). The heat of combustion is simply calculated from the ratio of the total energy release (defined as the time-integrated value of HRR) divided by the total sample mass loss. The experimental data from Ref. [22] are then recast as HRR divided by the effective heat of combustion, thereby providing information on the time variations of the fuel mass loss rate (MLR). The experimental uncertainties associated with HRR measurements are estimated to be 13%; the uncertainties associated with the estimate of the heat of combustion are estimated to be 3%. The cone calorimeter tests produced MLR curves featuring an "ignition" delay and two distinct peaks. Lower (higher) levels of radiation intensity corresponded to longer (shorter) ignition delays, lower (higher) values of the mass loss rates and longer (shorter) burn out times.

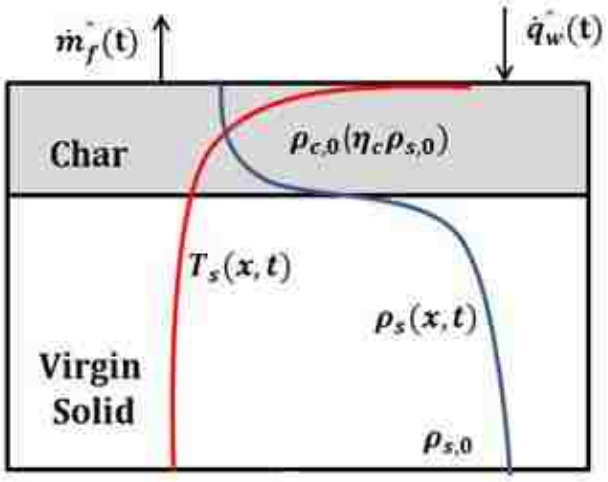

Figure 2-1. One-dimensional pyrolysis model

2.3.2 Pyrolysis modeling

The present study considers a classical pyrolysis modeling approach in which thermal degradation across the flammable solid is formulated as a local one-dimensional problem in the direction normal to the exposed solid surface (Fig. 2.1).

The model formulation is based on simple conservation statements for heat and mass, coupled with a global one-step finite-rate decomposition chemistry model proposed for charring materials. Note that results from the micro-scale experiments presented in Ref. [22] suggest that an accurate description of PVC pyrolysis chemistry requires a sequence of at least two consecutive reactions. However, we are interested here in exploring the limitations of the semi-empirical approach and we consider that for many practical flammable materials, this approach will not be informed by micro scale experiments and will rely on a global one-step reaction model (see for instance Refs. [23] and [25]). Therefore, we choose to ignore the information presented in Ref. [22], assume that the PVC material is only characterized by bench-scale experiments (see Section 2.1), and consider in the following one-step pyrolysis chemistry. Similarly, possible in-depth radiation effects are neglected in the model formulation.

The main equations of the model formulation are:

$$\rho_s c_s \frac{\partial T_s}{\partial t} = \frac{\partial}{\partial x}\left(k_s \frac{\partial T_s}{\partial x} \right) - \dot{\omega}_s''' \Delta H_R \qquad (1)$$

$$\frac{\partial \rho_s}{\partial t} = -\dot{\omega}_s''' \qquad (2)$$

where ρ_s, c_s, k_s and T_s designate the mass density, heat capacity, thermal conductivity and temperature of the solid material, x the spatial coordinate normal to the exposed surface, $\dot{\omega}_s'''$ the mass reaction rate (i.e., the amount of virgin solid mass transformed into volatiles by pyrolysis processes per unit time per unit volume) and ΔH_R the heat of pyrolysis (i.e., the heat required to generate unit mass of volatiles at temperature T_s). Equation (1) describes heat conduction inside the solid and accounts

for endothermic pyrolysis processes. Equation (2) describes solid mass loss due to phase change and the associated production of flammable vapors.

The mass reaction rate is formulated using an Arrhenius-like expression:

$$\dot{\omega}_s''' = \begin{cases} 0 & , T_s \le T_{thr} \\ (\rho_s - \eta_c \rho_{s,0})\, A \exp(-E/RT_s) & , T_s > T_{thr} \end{cases} \tag{3}$$

where T_{thr} is a threshold temperature, $\rho_{s,0}$ the initial mass density of the solid material, η_c the char yield (one minus the yield of volatiles noted η_v), A a pre-exponential factor and E an activation energy.

The fuel mass loss rate (per unit exposed surface area) is by definition the mass flux of volatiles from the exposed surface of the solid material and may be expressed as:

$$\dot{m}_f''(t) = \int_0^L \dot{\omega}_s'''(x,t)\,dx \tag{4}$$

where L is the sample thickness. Note that Eq. (4) neglects any possible gas transport effect from the depth of the solid sample to the exposed surface.

The solid material is treated as optically opaque. The heat flux at the exposed surface of the solid material (at $x = 0$) is:

$$\dot{q}_w''(t) = \underbrace{\varepsilon G - \varepsilon\sigma(T_{s,w}{}^4 - T_\infty{}^4)}_{\text{radiation}} - \underbrace{h(T_{s,w} - T_\infty)}_{\text{convection}} \tag{5}$$

where ε is the surface emissivity, G the irradiation from the radiant panel, σ the Stefan-Boltzmann constant, $T_{s,w}$ the solid surface temperature (at $x = 0$), T_∞ the ambient gas temperature, and h the convective heat transfer coefficient. In the following, h is assumed to be constant, $h = 10$ W/m^2/K [22]. Also, in some of the models considered below, a flame heat flux is added to the RHS of Eq. (5) in order to represent the additional contribution of the flame to heat transfer once flaming is established, $\dot{q}''_{flame} = 0$ as long as $T_{s,w} \le T_{thr}$ and $\dot{q}''_{flame} = 10$ kW/m^2 once $T_{s,w} > T_{thr}$; the value of $\dot{q}''_{flame}$ is a representative mean value of data provided for several polymers in

Refs. [29-30].

The back PVC surface (at $x = L$) is either assumed to be adiabatic or is treated using a more realistic two-layer model that simulates the experimental conditions in which the back surface of the PVC sample is in contact with a 20 mm thick Kaowool blanket. The thermal properties of the Kaowool layer are taken from Ref. [22]: $r_{KL} = 48$ kg/m^3; $c_{KL} = 0.8$ kJ/kg/K; $k_{KL} = 0.08$ Wm/K.

Equations (1)-(2) are coupled partial differential equations; these equations are numerically solved using an algorithm based on second-order central differencing for spatial discretization and second-order Crank Nicolson for time integration, and using MATLAB as the programming language. The equations can be numerically stiff and typical values for the spatial and time increments are: $\Delta x \approx 50\,\mu$m and $\Delta t \approx 0.05$ s.

Virgin solid and char material properties	
ρ_{vs}, ρ_c	mass density
c_{vs}, c_c	specific heat capacity
k_{vs}, k_c	thermal conductivity
$\varepsilon_{vs}, \varepsilon_c$	emissivity

Reaction parameters	
η_v	fuel (volatile) yield
ΔH_R	heat of pyrolysis
T_{thr}	threshold temperature
A	pre-exponential factor
E	activation energy

Table 2-1. Input parameters for the pyrolysis model.

Table 2.1 presents the complete list of model parameters for the single-step finite-rate-chemistry char-producing pyrolysis model described in Eqs. (1)-(5). The model features 13 parameters to describe material properties and chemical reaction coefficients. Unless specified otherwise, these parameters are considered as unknown. Note that the material properties for the virgin solid and char residue are assumed to be constant (i.e., temperature-independent). Note also that for a single-step char-producing reaction, the char yield (also called the residue yield) is equal to 1 minus

the volatile yield (also called fuel yield).

The number of unknown model parameters may be reduced by considering that some of the solid properties are known from experimental measurements or that some simplifying assumptions can be made. For instance, in some of the models considered below, the following simplifications are made: the chemical kinetic parameters A and E are estimated using thermo-gravimetric analysis (TGA); the concept of a threshold temperature is removed from the model formulation (in other words, the threshold temperature is the ambient temperature); the surface emissivities are close to 1 and assumed to be equal to 0.9; the solid sample is assumed to have constant volume (i.e., the PVC sample does not swell, nor shrink), which leads to a relationship between virgin solid mass density, char mass density and char yield. When making all these simplifications, the number of unknown model parameters is reduced to 7. While further reduction of the number of unknown parameters is certainly possible in the case of PVC (see Ref. [22] for experimentally-based estimates), we choose in the present study to treat the flammable solid as a poorly characterized material and use mathematically-based parameter estimation techniques to evaluate a significant number (from 7 to 12) of the model parameters.

2.3.3 Parameter estimation

The present study considers different parameter estimation methodologies based on two optimization techniques – a genetic algorithm (Section 2.3.3.1) and a stochastic hill-climber algorithm (Section 2.3.3.2) – and detailed comparisons with cone calorimeter test data. The genetic and stochastic hill-climber algorithms have been written to automatically and iteratively adapt the values of the unknown model parameters in order to minimize the error between model predictions and experimental data.

2.3.3.1 Genetic algorithm

In recent years, genetic algorithms (GA) have been successfully applied to the problem of parameter estimation in pyrolysis modeling [17, 31-33]. The logic of

genetic algorithms can be described in four distinct processes: (1) initialization; (2) selection; (3) reproduction; and (4) termination. The initial traits of individuals (in the present application, an individual represents a particular set of values of the unknown model parameters) within a population (defined as a group of individuals) are randomly generated within a user-defined parameter space. Population size is also a user-defined quantity and, depending on the problem, can range from hundreds to tens of thousands of individuals; we use population sizes equal to a few hundreds. With each successive generation, a percentage of the population is selected for reproduction. Probability of selection is customarily based on fitness. In the present application, fitness can be interpreted as an inverse error function where the error measures the mean distance between model predictions and cone-calorimeter-based experimental data. Fitness functions quantify the extent to which individuals are adapted to the conditions of their environment. Reproduction is the process by which a new generation is derived from a previous one. Reproduction is accomplished through the genetic processes of crossover (also called recombination) and/or mutation. These genetic-like processes ensure convergence of the search process towards individuals with the highest fitness values. The evolutionary process is continued until a user-defined termination condition is reached; in the present study, convergence requires several hundred generations.

The error function adopted in the GA-based algorithm uses both mass loss rate and solid temperature data, for two levels of radiation intensity, $G = G1 = 75$ kW/m^2 and $G = G2 = 92$ kW/m^2; the error function ε is defined as:

$$\varepsilon = \theta_{MLR}(\varepsilon_{MLR}^{G1} + \varepsilon_{MLR}^{G2}) + \theta_T(\varepsilon_T^{G1} + \varepsilon_T^{G2}) \quad (6)$$

where ε_{MLR}^{G1} and ε_{MLR}^{G2} (ε_T^{G1} and ε_T^{G2}) designate error functions for MLR data (temperature data) for the two $G = G1$ and $G = G2$ tests, and where θ_{MLR} and θ_T are user-specified weight coefficients; we use $\theta_{MLR} = 0.7$ and $\theta_T = 0.3$ (because of limitations in the quality and scope of temperature data, the algorithm assigns a higher value to MLR data – see below). ε_{MLR}^{Gi} and ε_T^{Gi} are defined as:

$$\varepsilon_{MLR}^{Gi} = \frac{\left(\frac{\sum_n \left(MLR_{\text{sim}}^{Gi}(t_n) - MLR_{\text{exp}}^{Gi}(t_n)\right)^2}{n}\right)^{1/2}}{\frac{\sum_n MLR_{\text{exp}}^{Gi}(t_n)}{n}} \tag{7}$$

$$\varepsilon_{T}^{Gi} = \frac{\left(\frac{\sum_n \left(T_{\text{sim}}^{Gi}(t_n) - T_{\text{exp}}^{Gi}(t_n)\right)^2}{n}\right)^{1/2}}{\frac{\sum_n T_{\text{exp}}^{Gi}(t_n)}{n}} \tag{8}$$

where *MLR* and *T* refer to mass loss rate and solid temperature data, t_n and *n* refer to time data, and where the subscripts "sim" and "exp" designate simulation and experimental data, respectively. Note that temperature measurements inside a thermally degrading solid are notoriously difficult to perform and not always reliable. Consequently, the temperature data used in Eq. (8) are limited to the back surface location ($x = L = 6$ mm) and to temperature values below 135 ºC. Thus, while influenced by temperature data, the GA-based search algorithm used here is primarily focused on matching MLR data.

The present study considers three different parameter estimation methodologies corresponding to different weights given to the random mathematical search: the models are called (GA-a), (GA-b) and (GA-c). In (GA-a), the PVC surface emissivities are assumed equal to 0.9; also, the char mass density is calculated as the virgin material mass density multiplied by the char yield (constant volume is assumed), $\rho_c = \rho_{s,0} \times \eta_c = \rho_{s,0} \times (1 - \eta_v)$. The GA search is then applied to the remaining set of 10 model coefficients and is only constrained by user-defined limits. (GA-b) is similar to (GA-a) except that the virgin solid mass density, char mass density and char yield are treated as unknown (independent) parameters.

	GA-a	GA-b	GA-c
ρ_{vs} (kg/m^3)	1729.75	1673.05	2826.51
c_{vs} (kJ/kg/K)	1.1113	0.7202	0.734
k_{vs} (W/m/K)	0.17046	0.0783	0.182
ε_{vs}	0.9	0.9	0.9
ρ_c (kg/m^3)	397.8425	0.03489	28.265
c_c (kJ/kg/K)	3.8943	3.9841	0.03634
k_c (W/m/K)	0.102	0.1549	0.01
ε_c	0.9	0.9	0.9
η_v	0.77	0.81	0.99
ΔH_R (kJ/kg)	291.8	366.3	252.8
T_{thr} ($^\circ$C)	230.09	317.89	20.0
A (1/s)	2.98E+13	9.95E+14	5.98E+03
E (J/mol)	192886	251583	7.16E+04

Table 2-2. Values of the input parameters for the GA-based pyrolysis models.

The number of degrees of freedom in (GA-b) is therefore 11. (GA-c) is similar to (GA-a) except that the chemical kinetic parameters *A* and *E* are assumed to be known from TGA test data (the values of *A* and *E* are extracted from analysis of TGA data from Ref. [22]. The analysis starts from an initial three-parallel-step reaction model, then eliminates two of the three steps assuming that these reactions produce primarily

inert volatiles – i.e. chlorine – and subsequently treats the remaining step as a reaction that transforms 47% of the initial virgin solid mass into volatiles and char. Note that the values of A and E provided by this analysis are different from those reported in Ref. [22] where a two-step reaction model is assumed); also, the concept of a threshold temperature is removed from the model formulation. The number of degrees of freedom in (GA-c) is now 7. Finally, (GA-a) and (GA-b) assume $\dot{q}''_{flame} = 10\,\mathrm{kW/m^2}$ and treat the back PVC surface as adiabatic, whereas (GA-c) neglects $\dot{q}''_{flame}$ but adopts a more realistic model in which the back surface of the PVC sample is in contact with a Kaowool layer.

Table 2.2 presents the values of the model parameters after GA-based optimization. Parameters shaded in grey have been assumed. The last column in Table 2 presents the experimental data reported in Ref. [22]. Note that some of the values of the model parameters reported in Table 2 are clearly unrealistic, for instance the very low value for the mass density of the char in (GA-b). This may be explained by the underdetermined nature of the optimization problem, which results in the existence of multiple solutions. The values of the model parameters in Table 2 correspond to one of several valid solutions of the mathematical optimization problem but should not be considered as the (presumably unique) physical solution.

Figure 2.2 presents a comparison between cone calorimeter data and model predictions. The figure shows that all 3 models are successful at reproducing the global features of the time variations of the fuel mass loss rate (MLR) observed in the experimental study, in particular the (short) ignition delay, the timing of the first peak (within 17%), the magnitude of the first peak (within 10%), the timing of the second peak (within 28%), the magnitude of the second peak (within 14%), the total burn out time (within 10%), and the total mass loss (within 4%). The L2-norm error calculated over the entire time evolution of MLR and made non-dimensional by the average value of MLR (calculated between ignition and burn-out time) is approximately 20% for (GA-a) and (GA-b). For (GA-c), it is approximately 20% in the case G = 92 kW/m^2 but increases to 37% in the case G = 75 kW/m^2.

Figures 2.3 and 2.4 present the corresponding time variations of the front and back surface temperature. The figures show that all 3 models are successful at reproducing the early variation of the back surface temperature (the model performance is excellent in the case G = 92 kW/m^2 but only fair in the case G = 75 kW/m^2). Subsequent measured variations are considered unreliable and are not used, nor plotted. It is interesting to note that the 3 pyrolysis models predict significantly different evolutions of $T_s(L,t)$. Model (GA-b) in particular features the smallest value of thermal inertia and predicts back surface temperatures that are approximately 150 degrees higher than those predicted by model (GA-a).

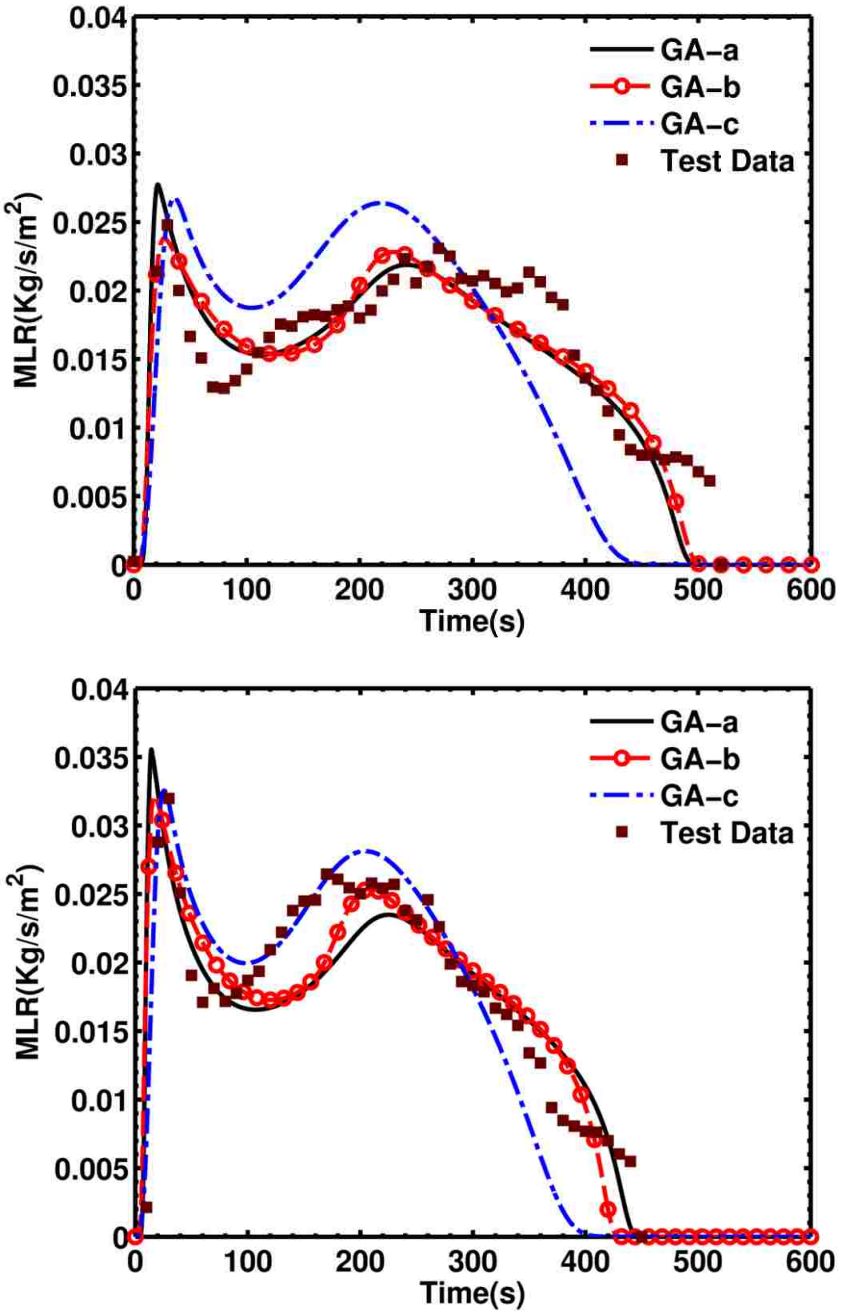

Figure 2-2. Cone calorimeter test: time variations of the fuel mass loss rate for a PVC sample subjected to 75 kW/m² (top) and 92 kW/m² (bottom). Comparison between experimental data (square symbols) and simulation results from GA-based models (lines).

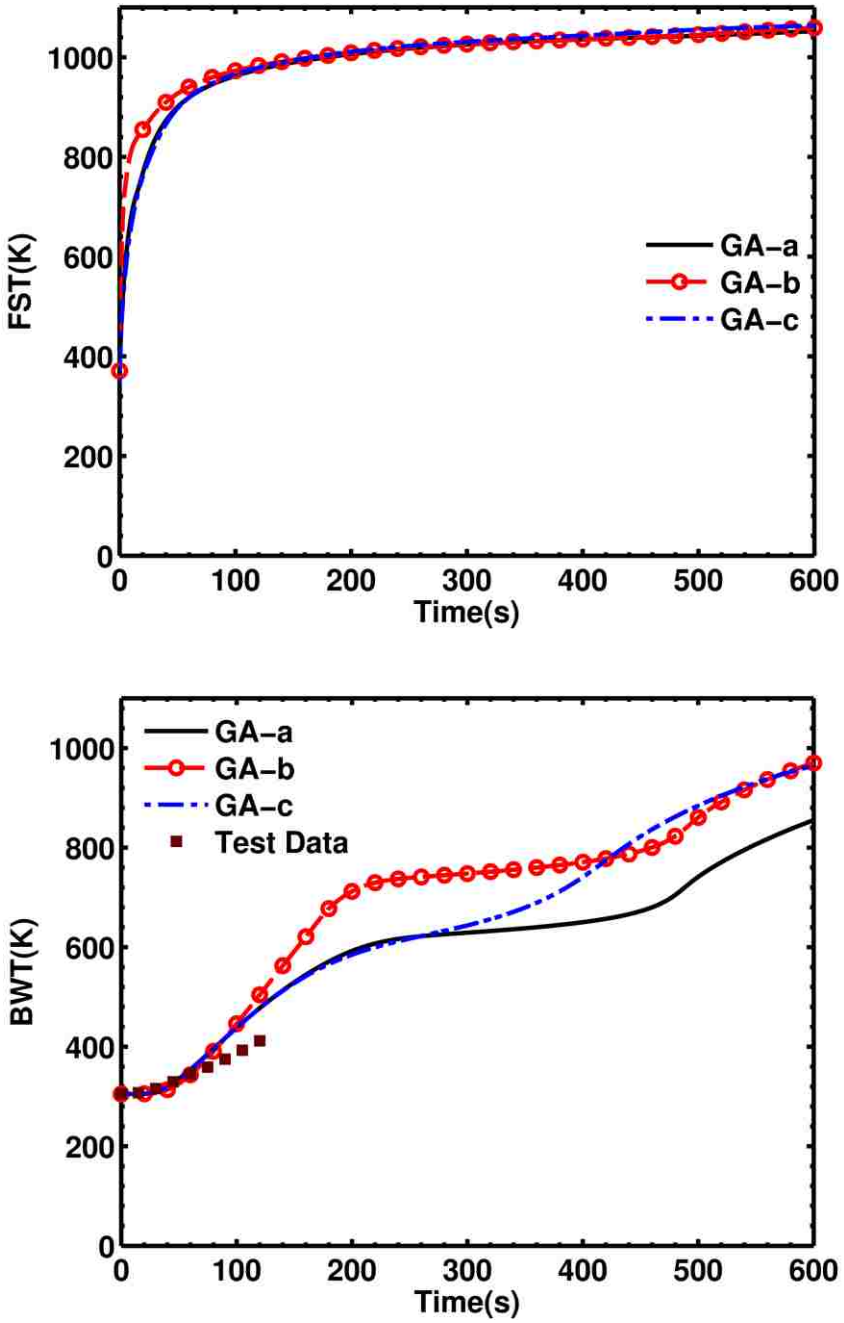

Figure 2-3. Cone calorimeter test: time variations of front (top) and back (bottom) surface temperature for a PVC sample subjected to 75 kW/m². Comparison between experimental data (square symbols) and simulation results from GA-based models (lines).

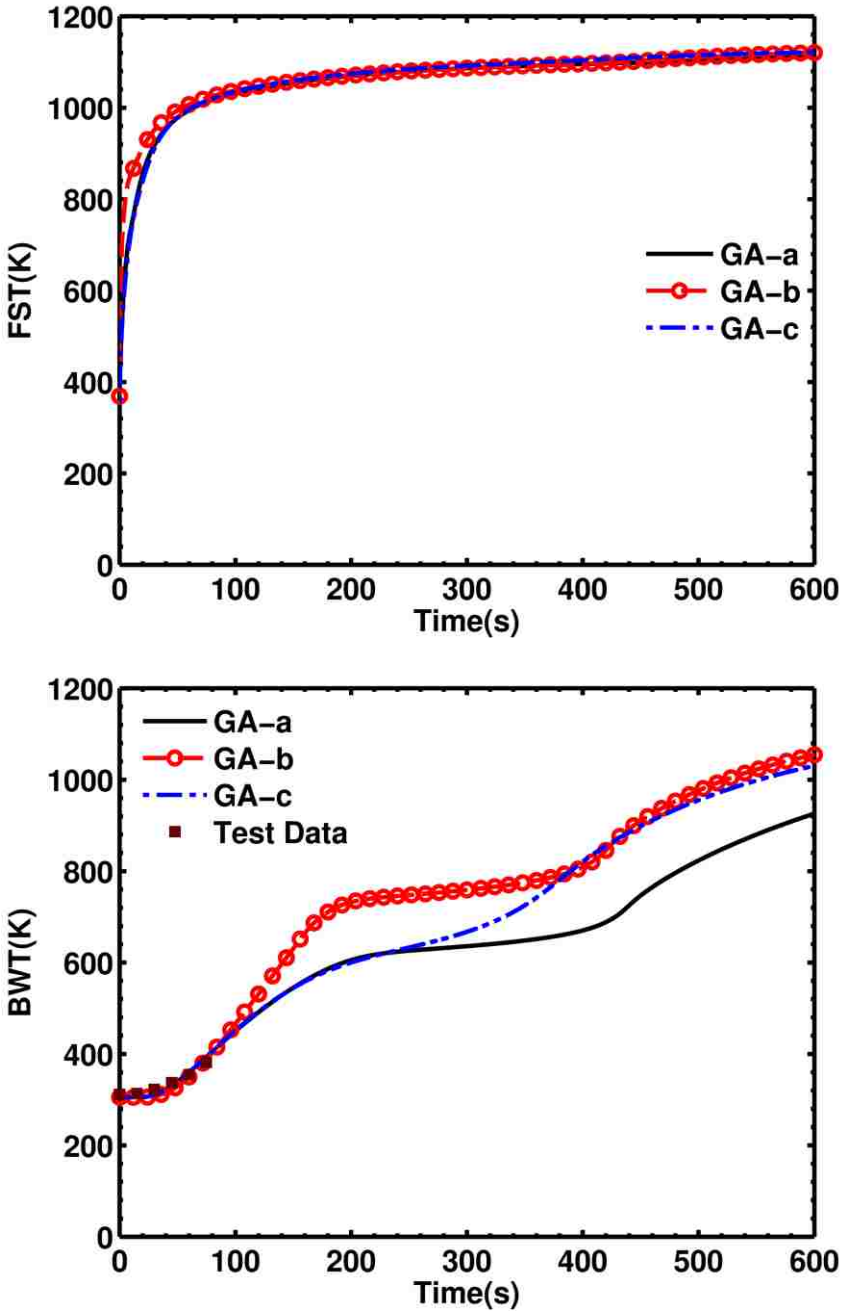

Figure 2-4. See caption of Fig. 2.3. Case G = 92 kW/m².

2.3.3.2 Stochastic hill-climber algorithm

The basic principle of stochastic hill-climber algorithms (HCA) is similar to that used in genetic algorithms, i.e., searching for successively better parameter sets

through random mutation [34]. In contrast to GA, HCA does not use crossover and mutation and has a population of two, parent and child. Stochastic hill-climbing is also different in that the parents outlive the children if they are better adapted to the environment.

The error function adopted in the HCA-based algorithm uses both mass loss rate and solid temperature data, for one level of radiation intensity, G = 75 kW/m^2. The error function is similar to that used for GA-based optimization (see Section 2.3.3.1). The present study considers three different parameter estimation methodologies corresponding to different weights given to the random mathematical search: the models are called (HCA-a), (HCA-b) and (HCA-c). In (HCA-a), the activation energy E is assumed to be equal to 0 (a convenient and somewhat arbitrary simplification that makes the reaction rate a step function, increasing from zero to the pre-exponential factor A at the threshold temperature). Also, the char yield is estimated as the ratio of char mass density divided by virgin solid mass density (constant volume is assumed); the HCA search is then applied to the remaining set of 11 model coefficients and is only constrained by user-defined limits. (HCA-b) is similar to (HCA-a) except that the virgin solid mass density, char mass density and char yield are treated as unknown (independent) parameters; the number of degrees of freedom in (HCA-b) is 12. (HCA-c) is similar to (HCA-a) except that the chemical kinetic parameters A and E are assumed to be known from TGA test data (the values of A and E are extracted from analysis of TGA data from Ref. [22]; the analysis assumes that only 47% of the initial virgin solid mass is transformed into fuel volatiles or char; see the comment made in Section 2.3.3.1). The concept of a threshold temperature is removed from the model formulation; the number of degrees of freedom in (HCA-c) is now 9. Finally, (HCA-a) and (HCA-b) assume $\dot{q}''_{flame} = 10\,\text{kW/m}^2$ and treat the back PVC surface as adiabatic, whereas (HCA-c) neglects $\dot{q}''_{flame}$ but adopts a more realistic model in which the back surface of the PVC sample is in contact with a Kaowool layer.

Table 2.3 presents the values of the model parameters after HCA-based optimization. Parameters shaded in grey have been assumed. The last column in Table 2.3 presents the experimental data reported in Ref. [22]. Note again that some of the value of the model parameters reported in Table 3 are clearly unrealistic, for instance the very low values for the char emissivity in (HCA-a) and (HCA-b).

	HCA-a	HCA-b	HCA-c
ρ_{vs} (kg/m^3)	1500	2000	2700
c_{vs} (kJ/kg/K)	2.7	1.9	0.99
k_{vs} (W/m/K)	0.5	0.47	0.2
ε_{vs}	0.98	0.86	1
ρ_c (kg/m^3)	72	370	65
c_c (kJ/kg/K)	4.1	5	1
k_c (W/m/K)	0.05	0.05	0.1
ε_c	0.41	0.37	0.95
η_v	0.952	0.7	0.976
ΔH_R (kJ/kg)	350	99	380
T_{thr} ($^\circ$C)	220	210	20.0
A (1/s)	7.10E-02	5.70E-02	5.98E+03
E (J/mol)	0	0	7.16E+04

Table 2-3. Values of the input parameters for the HCA-based pyrolysis models.

Figure 2.5 presents a comparison between cone calorimeter data and model predictions. The figure shows that all 3 models are successful at reproducing the global features of the time variations of the fuel mass loss rate (MLR) observed in the experimental study, in particular the (short) ignition delay, the timing of the first peak (within 30%), the magnitude of the first peak (within 10% for (HCA-c), and within 17% for (HCA-a) and (HCA-b)), the timing of the second peak (within 13%), the magnitude of the second peak (within less than 11%), the total burn out time (within 20%), and the total mass loss (within 10%). The L2-norm error calculated over the entire time evolution of MLR and made non-dimensional by the average value of MLR (calculated between ignition and burn-out time) is approximately 15% for (HCA-b), 19% for (HCA-a) and 30% for (HCA-c).

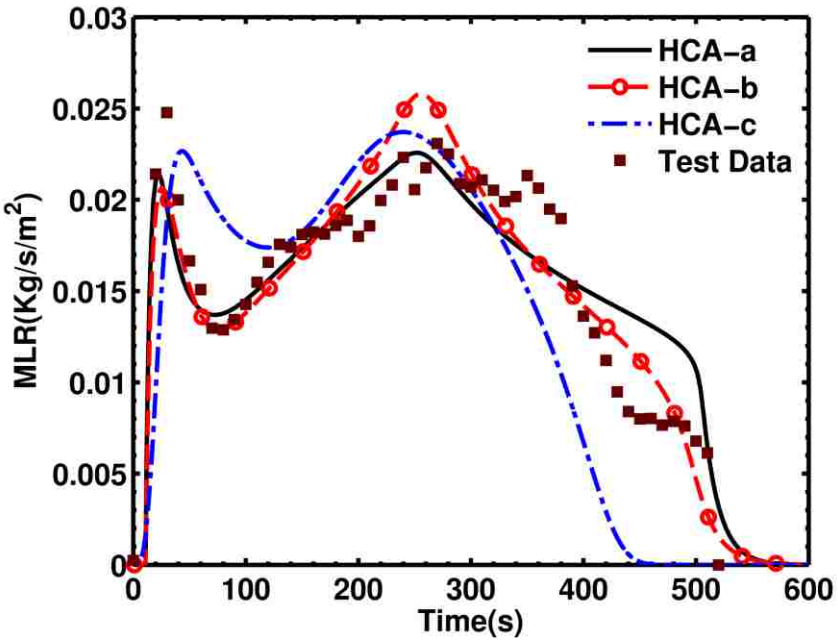

Figure 2-5. Cone calorimeter test: time variations of the fuel mass loss rate for a PVC sample subjected to 75 kW/m². Comparison between experimental data (square symbols) and simulation results from HCA-based models (lines).

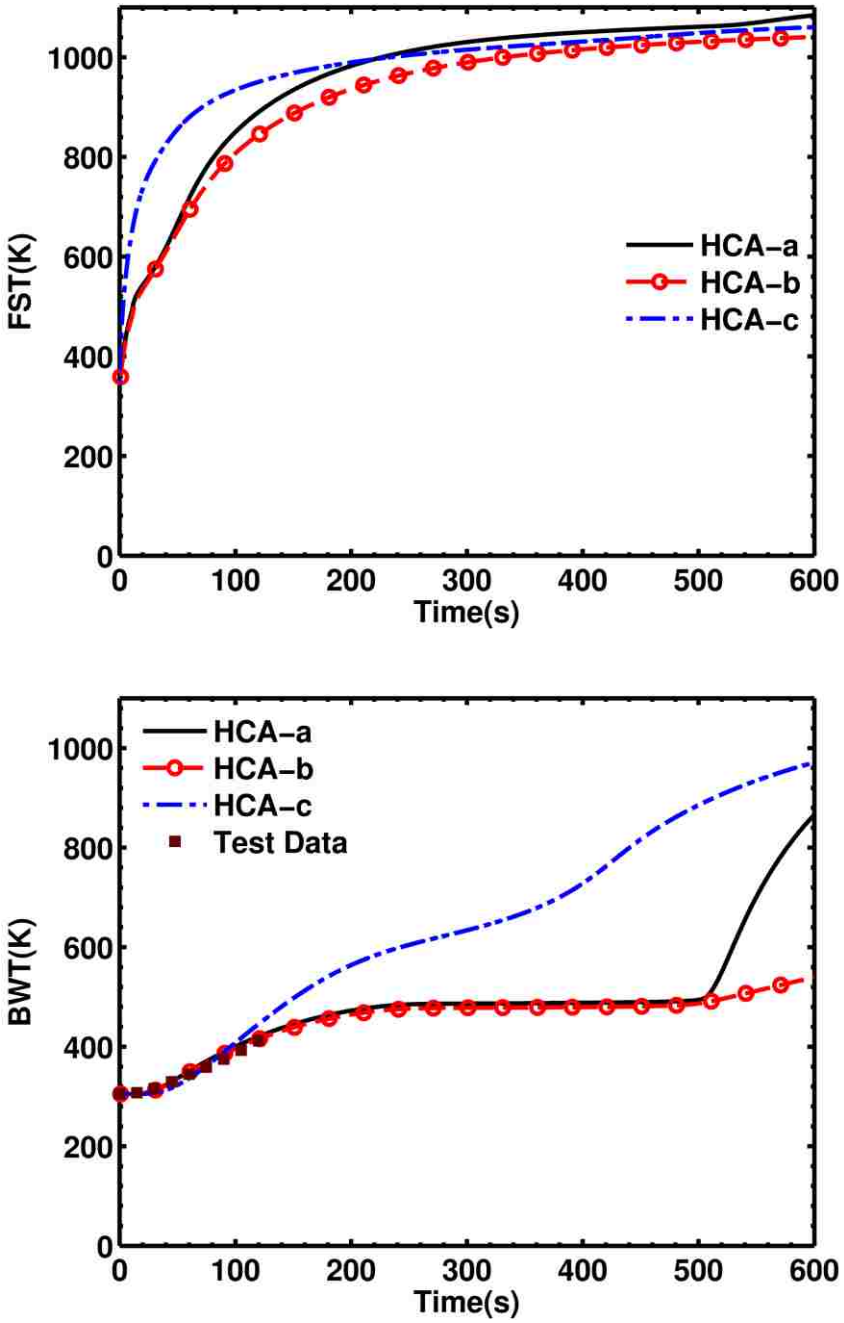

Figure 2-6. Cone calorimeter test: time variations of front (left) and back (right) surface temperature for a PVC sample subjected to 75 kW/m². Comparison between experimental data (square symbols) and simulation results from HCA-based models (lines).

Figure 2.6 presents the corresponding time variations of the front and back surface temperature. The figure shows that all 3 models are successful at reproducing

the early variation of the back surface temperature (up to 100 degrees Celsius). Again, subsequent measured variations are considered unreliable and are not used, nor plotted. It is interesting to note that the 3 pyrolysis models predict significantly different evolutions of the PVC temperatures: model (HCA-c) in particular predicts front and back surface temperatures that may be more than 200 degrees higher than those predicted by models (HCA-a) and (HCA-b).

2.4. Comparison between the PVC pyrolysis models in cone calorimeter tests

The previous section has described the development of six different models to treat PVC pyrolysis. These models are calibrated against experimental data from cone calorimeter tests using relatively high values of the radiation intensity (G = 75 kW/m^2 and G = 92 kW/m^2 for GA-based models; G = 75 kW/m^2 for HCA-based models), thin samples (L = 6 mm), and thermally insulated back surface conditions. In this section, we consider again the cone calorimeter configuration but now explore the predictions of the pyrolysis models for conditions that are significantly different from those used during calibration: the radiation intensity takes values between G = 5 and G = 200 kW/m^2; the sample thickness is changed from L = 0.6 mm to L = 6 cm; the back surface thermal boundary condition is a heat sink or a heat source. The pyrolysis models are compared in terms of the following global properties: the ignition time; the MLR peak value; the time to MLR peak; the burn out time; and the average MLR value. The intent in this comparative study is to determine whether, and by how much, predictions from the six pyrolysis models (which by construction, converge for conditions within a certain calibration range) start to diverge for conditions that are of general interest but lie outside of this calibration range.

2.4.1 Effect of changing the radiation intensity

We assume here that L = 6 mm and that the back surface of the PVC samples is adiabatic. The irradiation from the radiant panel is changed from high values that are relevant to post-flashover fire conditions ($G \geq$ 50 kW/m^2) to low values that are relevant to ignition conditions ($G \leq$ 10 kW/m^2).

Figure 2.7 presents a comparison of the simulated time variations of MLR as predicted using all six pyrolysis models, for G = 100 kW/m^2 and G = 10 kW/m^2. As expected, lower values of the thermal loading results in longer ignition delays, lower values of MLR and longer burn out times. Lower values of G also correspond to a change from a double-peak variation of MLR to a single-peak variation: the early decrease in MLR after a first peak is typical of char-forming materials (the char layer that is formed at the exposed surface of the PVC sample acts as a thermal barrier and has a negative impact on the gas-to-virgin-solid heat transfer); the final decrease in MLR is due to burn out. For G = 100 kW/m^2, the increase in MLR observed between (approximately) 1 and 3 minutes is explained by the back surface thermal boundary condition (the heating process taking place inside the PVC sample is accelerated once the heated layer reaches the adiabatic back surface); for G = 10 kW/m^2, this increase is not observed because the negative effect of the char at the front surface and the positive effect of adiabatic insulation at the back surface occur simultaneously and the two peaks are merged.

Furthermore, while the level of agreement between the six PVC models is relatively good at G = 100 kW/m^2 (these conditions are close to those adopted during calibration), it is seen that the models present significant levels of disagreement at G = 10 kW/m^2. The increasing discrepancy between the predictions of the pyrolysis models as the thermal load takes decreasing values is one of the main results of the present study. In Fig. 7, this discrepancy is quite large. For instance, for G = 10 kW/m^2, while all other models predict a successful start of pyrolysis (within a few minutes of exposure), model (GA-b) predicts no ignition of the PVC sample. This prediction may be explained by the high value of the threshold temperature adopted in (GA-b) (see Table 2); this high value results in unusually long ignition delays or simply no ignition at low values of the radiation intensity. In addition, while successful ignition is observed for G = 10 kW/m^2 in models (GA-a), (GA-c), (HCA-a), (HCA-b) and (HCA-c), the details of the pyrolysis process differ significantly: ignition times vary by a factor 2, peak values of MLR by a factor 3 and burn out times by a factor 2.

The variations of global pyrolysis properties with radiation intensity were examined systematically in order to quantify differences in the predictions of the six pyrolysis models. Figures 2.8 and 2.9 present the variations of global pyrolysis properties with radiation intensity. The global properties are the peak and average values of MLR (Fig. 2.8) and the times to ignition, to MLR first peak and the burn out time (Fig. 9). Ignition time is defined as the time to reach a critical MLR value equal to $\dot{m}''_f = 1\,\text{g/s/m}^2$, as suggested by Stoliarov *et al*. [35]. The burn out time is defined as the time (measured from ignition) when the MLR value falls below the critical value equal to $\dot{m}''_f = 1\,\text{g/s/m}^2$.

The average value of MLR is calculated from ignition to burn out. MLR and time are made non-dimensional in Figs. 8-9 with the following definitions (the + superscript indicates a non-dimensional value):

$$
\begin{aligned}
(\dot{m}''_f)^+ &= \frac{\dot{m}''_f}{(\dot{q}''_{w,ref}/\Delta H_{R,ref})} \\
(t_{ign})^+ &= \frac{t_{ign}}{(\pi(k_{ref}\rho_{ref}c_{ref})(T_{ign,ref}-T_\infty)^2/(2\dot{q}''_{w,ref})^2)} \\
(t_{peak})^+ &= \frac{t_{peak}}{(\pi(k_{ref}\rho_{ref}c_{ref})(T_{ign,ref}-T_\infty)^2/(2\dot{q}''_{w,ref})^2)} \\
(t_{bo})^+ &= \frac{t_{bo}}{(\rho_{ref}L\Delta H_{R,ref}/\dot{q}''_{w,ref})}
\end{aligned}
\qquad (9)
$$

where ρ_{ref}, c_{ref}, k_{ref}, $\Delta H_{R,ref}$, $T_{ign,ref}$ designate reference values for the PVC mass density, heat capacity, thermal conductivity, heat of pyrolysis and ignition (threshold) temperature, where T_∞ is ambient temperature, $\dot{q}''_{w,ref}$ a reference estimate of the net wall heat flux, and where t_{ign}, t_{peak} and t_{bo} designate times to ignition, to peak MLR and burn out time. In Figs. 8-9, ρ_{ref}, c_{ref}, k_{ref}, $\Delta H_{R,ref}$, $T_{ign,ref}$ are obtained from Refs. [22,35]: $\rho_{ref} = 1430\,\text{kg/m}^3$; $c_{ref} = 1550$ J/kg/K ; $k_{ref} = 0.17$ W/m/K ; $\Delta H_{R,ref} = 1420$ kJ/kg ; $T_{ign,ref} = 270\,^\circ\text{C}$; $\dot{q}''_{w,ref}$ is estimated by the irradiation, $\dot{q}''_{w,ref} = G$.

Figures 2.8 and 2.9 show that the discrepancy between model predictions increase significantly at low values of the external heat loading, for $G \leq 25$ kW/m^2. As seen in Fig. 8, the standard deviation of the simulated peak MLR value (average MLR value) is 0.056 (0.048) at G = 100 kW/m^2 and 0.38 (0.40) at G = 10 kW/m^2. Similarly (but with a less pronounced effect), as seen in Fig. 9, the standard deviation of the times to ignition (burn out time) is 0.58 (0.68) at G = 100 kW/m^2 and 1.17 (1.39) at G = 10 kW/m^2.

Figure 2.10 presents the spatial variations of the virgin solid volume fraction x_{vs}, the solid temperature T_s, and the pyrolysis mass reaction rate $\dot{\omega}_s'''$, at t = 120 s and for G = 100 kW/m². The virgin solid volume fraction is a convenient diagnostic to monitor the pyrolysis zone location: $x_{vs} = x_{vs,0}$ in the virgin solid (where $x_{vs,0}$ is the initial value of x_{vs}; $x_{vs,0} = 1$ in models (GA-a), (GA-b), (HCA-a), (HCA-b); $x_{vs,0} = 0.47$ in models (GA-c) and (HCA-c), which accounts for the production of inert volatiles); $x_{vs} = 0$ in the char layer; and the pyrolysis zone is the region where x_{vs} changes from $x_{vs,0}$ to 0. The pyrolysis zone location can also be monitored by plotting $\dot{\omega}_s'''$; note that the spatial integral of $\dot{\omega}_s'''$ is equal to the fuel mass loss rate, see Eq. (4). Figure 10(a) shows that all models describe the build-up of a char layer ($x_{vs} = 0$) near the exposed surface of the PVC sample (at x = 0). Also all models approximately agree on the thickness and location of the pyrolysis zone (see Fig. 10(c)): the thickness of the pyrolysis zone is on the order of 1 mm and at t = 120 s, the pyrolysis zone has propagated about 1-1.5 mm into the depth of the PVC sample. The models show more significant differences in their predictions of the heat distribution (see Fig. 10(b)): models (HCA-a) and (HCA-b) predict front surface temperatures that are more than 100 degrees lower than those predicted by other models; in addition, the heat is diffusing more slowly in (HCA-a) and (HCA-b) compared to other models and the back surface temperature takes values that change by more than 100 degrees when comparing (HCA-a) and (HCA-b) to (GA-b).

Figure 2.11 presents the spatial variations of x_{vs}, T_s and $\dot{\omega}_s'''$, at t = 1200 s and for G = 10 kW/m². Figure 2.11 shows that there are significant levels of disagreement between the six PVC models: model (GA-b) predicts no ignition; all other models predict a distributed pyrolysis zone that spans across the entire depth of the sample; but while models (GA-a), (GA-c) and (HCA-c) predict quasi-uniform variations of $\dot{\omega}_s'''$ (i.e. relatively flat profiles), models (HCA-a) and (HCA-b) predict strong spatial variations of $\dot{\omega}_s'''$; in addition, predictions in PVC composition vary widely (the simulated composition of the exposed surface at x = 0 varies between virgin PVC, as predicted by (GA-b), and pure char, as predicted by (HCA-a) and (HCA-b), see Fig. 2.11(a)) and predictions in solid temperatures vary by more than 100 degrees (Fig. 2.11(b)).

We now briefly consider the particular case of model (GA-b) at G = 10 kW/m². Figure 2.11(b) shows that at t = 1200 s, the PVC temperature predicted by model (GA-b) is approximately uniform and takes values above the threshold temperature, $T_s \approx 380\,^{\circ}\mathrm{C}$ compared to $T_{thr} = 317.9\,^{\circ}\mathrm{C}$: strictly speaking, model (GA-b) (like all other models) predicts a successful start of pyrolysis; however the values taken by the pyrolysis mass reaction rate $\dot{\omega}_s'''$ and the mass loss rate $\dot{m}_f''$ are very low and remain well below the critical threshold used to define ignition, $\dot{m}_f'' << 1\,\mathrm{g/s/m^2}$. Thus, at low values of the radiation intensity, model (GA-b) predicts super-critical heating of the PVC sample but sub-critical values of the mass loss rate and no flaming ignition.

A sensitivity analysis was carried out with the intent to understand the source of discrepancy between the different pyrolysis models at low values of G through a better understanding of the relative importance of the different pyrolysis model parameters on the PVC response to thermal loading. The thermal properties (k, ρ, c and ε) of the virgin solid and char, the chemical kinetic parameters (A and E), and the heat of pyrolysis (ΔH_R) were systematically varied within the range of values given in Tables 2 and 3, and for values of G between 5 and 200 kw/m^2.

It was found that for $G \leq 25$ kW/m^2, the response of PVC is strongly influenced

by the values of A and E, whereas at higher values of G, the response is approximately insensitive to the choice of chemical kinetic parameters (under high G conditions, the pyrolysis chemistry may be considered as infinitely fast). In other words, the increasing discrepancy between the predictions of the different PVC pyrolysis models as one goes to low values of G may be explained by the large variations in the values of A and E adopted by these models (see Tables 2.2 and 2.3). Note that the models are calibrated at high values of G (see Section 2.2.3), i.e. under conditions for which the PVC response is insensitive to details of the pyrolysis chemistry. This analysis suggests that a correct calibration of the chemical reaction coefficients A and E requires including experimental data at low irradiation levels and that the limited calibration discussed in Section 2.2.3 (using cone calorimeter data obtained at G = 75 kW/m^2 and/or G = 92 kW/m^2) does not allow an application of the pyrolysis models to low G conditions.

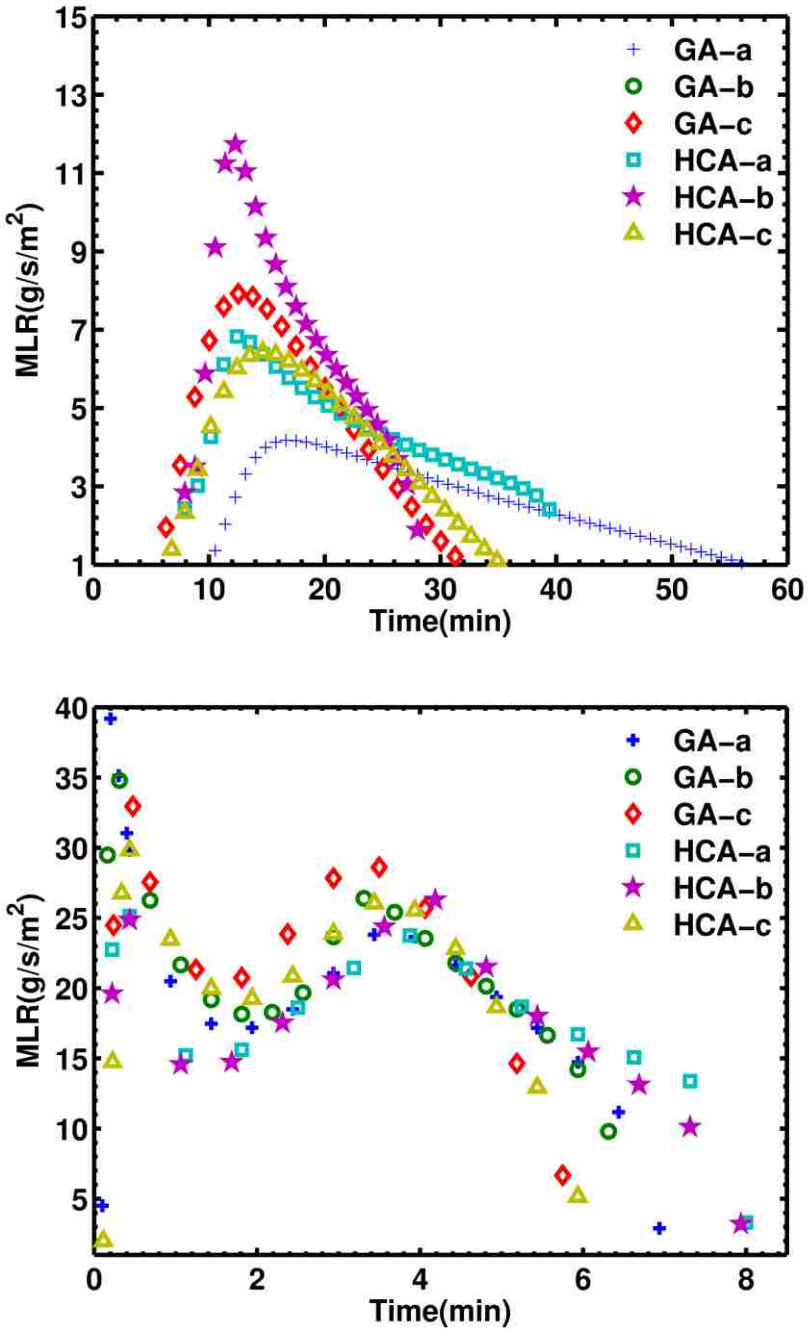

Figure 2-7. Cone calorimeter test: time variations of the fuel mass loss rate for a PVC sample subjected to 100 kW/m² (bottom) and 10 kW/m² (top), 6 mm thick PVC sample and adiabatic back surface. The (GA-b) curve for G = 10 kW/m² corresponds to no ignition (MLR □ 0) and is not plotted.

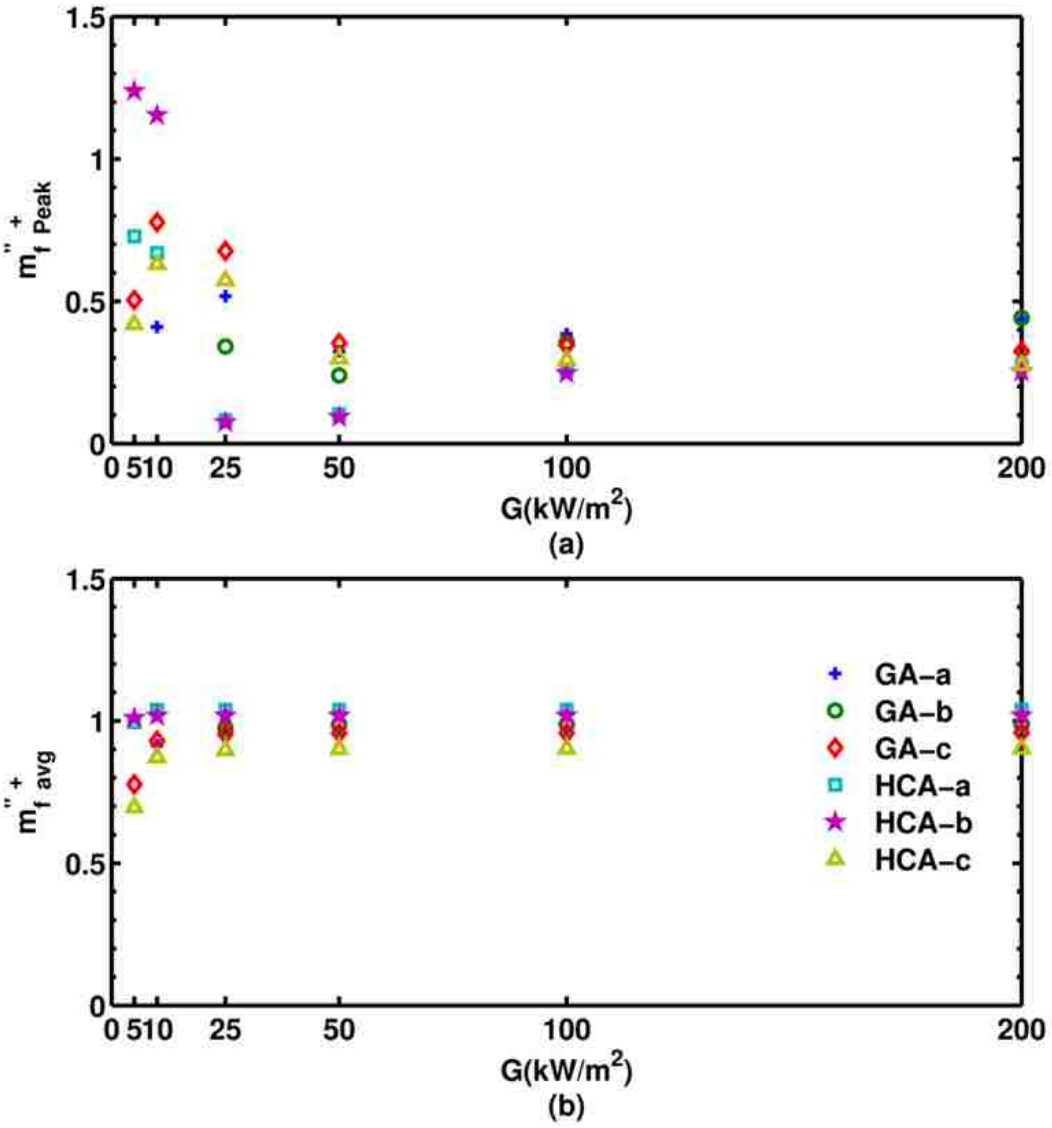

Figure 2-8. Cone calorimeter test: normalized peak (top) and average (bottom) value of the fuel mass loss rate as a function of the irradiation from the radiant panel, 6 mm thick PVC sample and adiabatic back surface. The (GA-b) data for G = 5 and 10 kW/m² corresponds to no ignition (MLR = 0) and are not plotted.

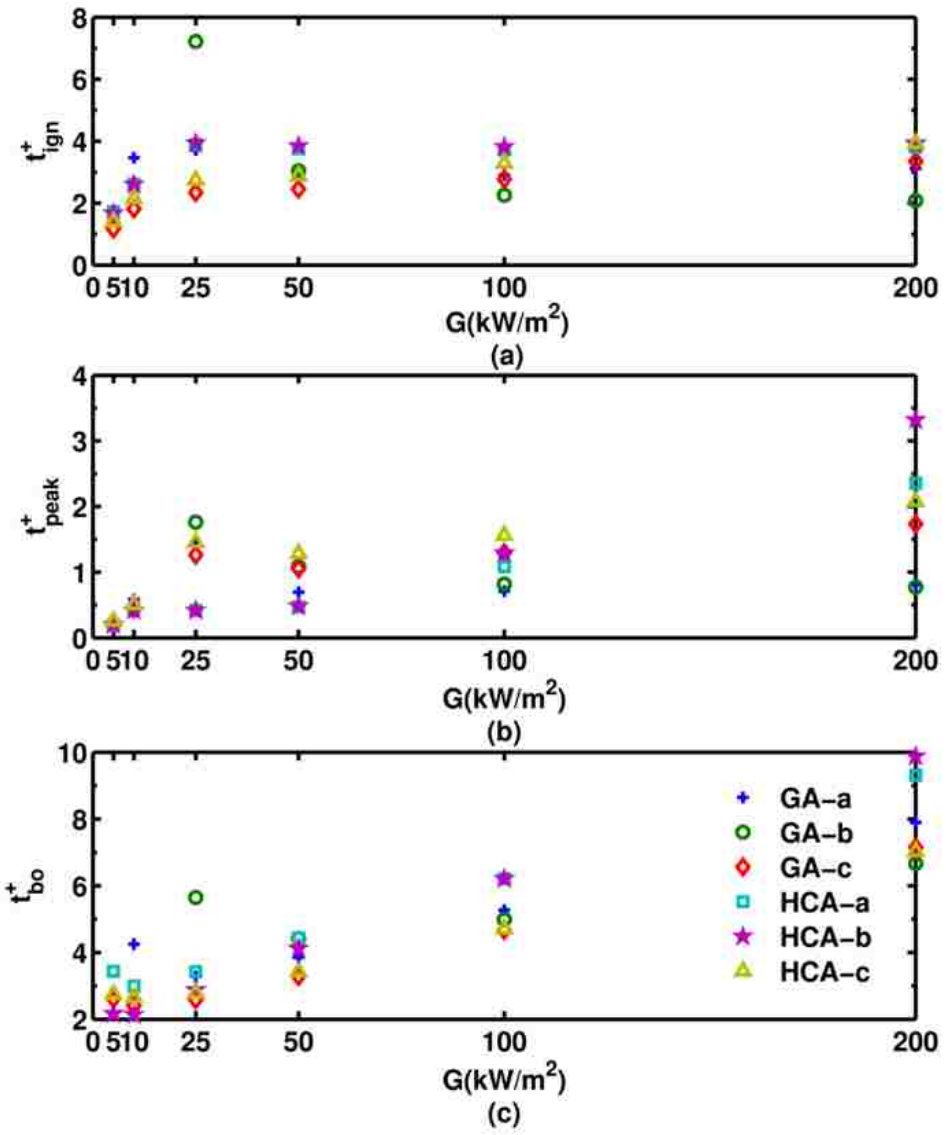

Figure 2-9. Cone calorimeter test: normalized ignition time (top), time to first peak of the fuel mass loss rate (middle) and burn-out time (bottom) as a function of the irradiation from the radiant panel, 6 mm thick PVC sample and adiabatic back surface. The (GA-b) data for G = 5 and 10 kW/m² corresponds to no ignition (ignition time, time to first peaks and burn-out times are infinite) and are not plotted.

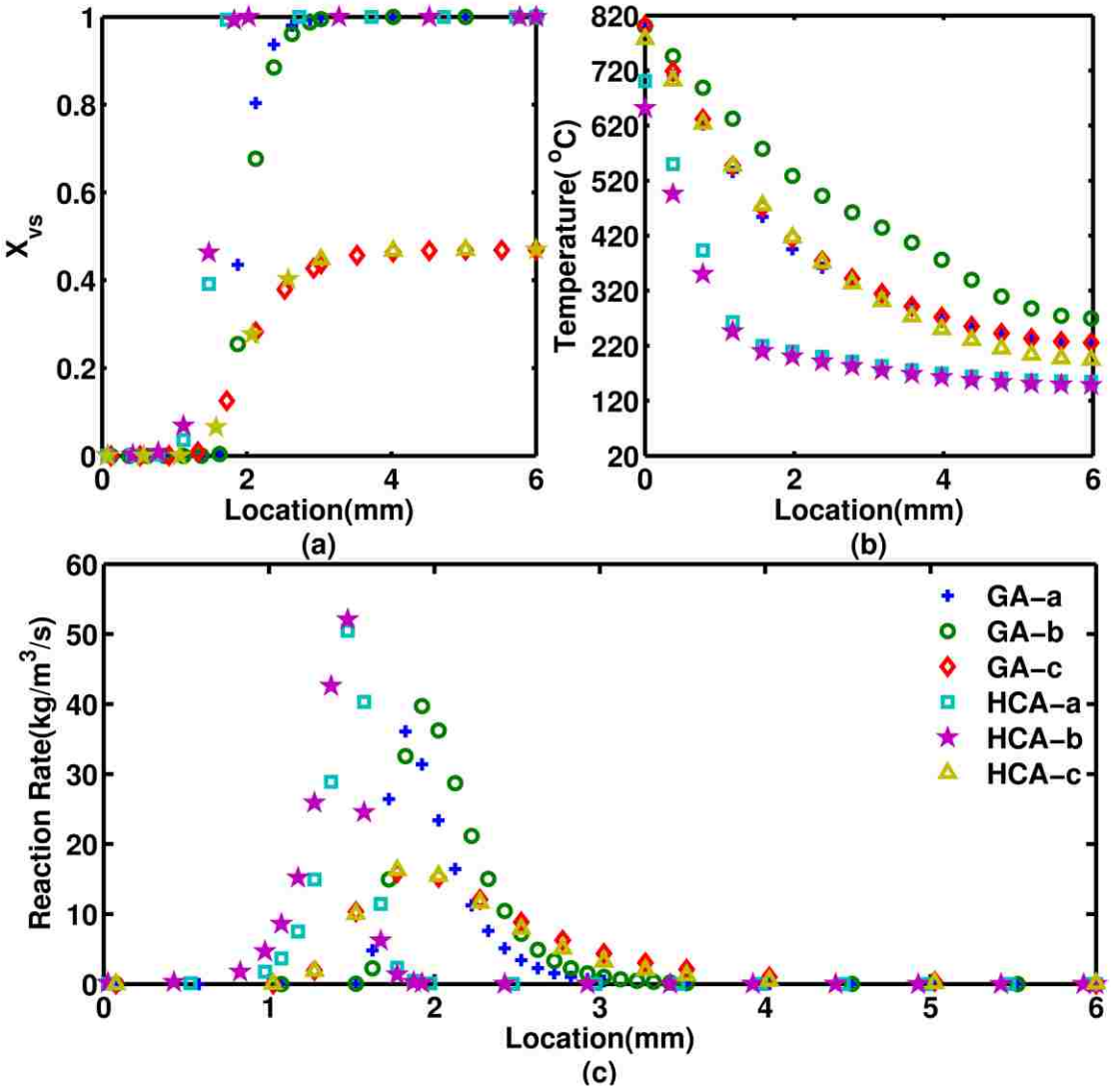

Figure 2-10. Cone calorimeter test: spatial variations of (a) the virgin solid volume fraction, (b) the solid temperature, (c) the pyrolysis mass reaction rate, at t = 2 minutes for G = 100 kW/m², 6 mm thick PVC sample and adiabatic back surface.

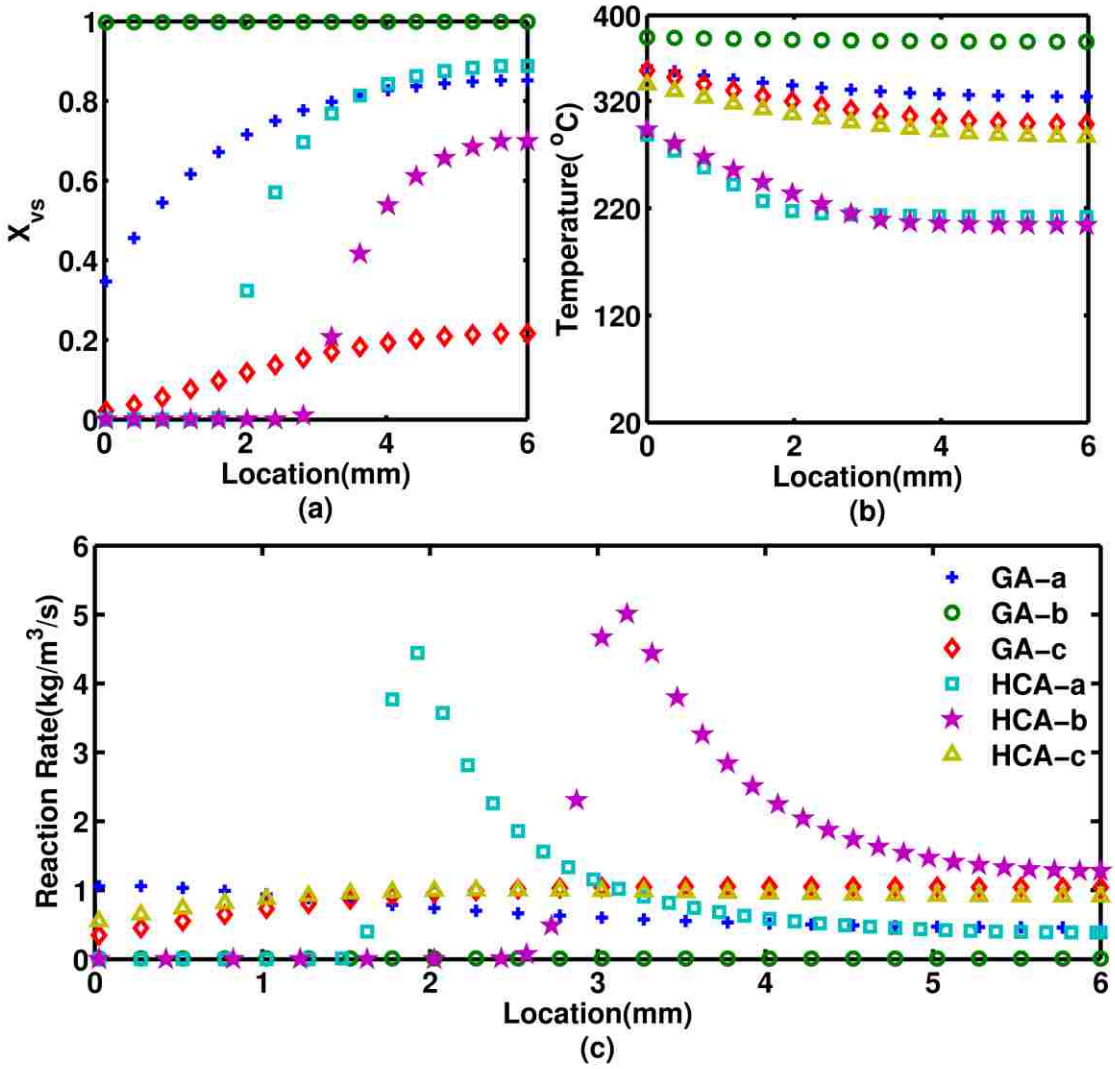

Figure 2-11. See caption of Fig. 2.10. Data taken at t = 20 minutes for G = 10 kW/m².

2.4.2 Effect of changing the sample thickness

We assume here that the irradiation from the radiant panel is G = 100 kW/m^2 and that the back surface of the PVC samples is adiabatic; the sample thickness is changed from thermally-thin (L = 0.6 mm) to thermally-thick (L = 6 cm) conditions. Note that the assumption of radiatively-opaque materials becomes questionable for ultra-thin samples.

Figure 2.12 presents a comparison of the simulated time variations of MLR as

predicted using all six pyrolysis models, for L = 0.6 mm. The variations of MLR present a single peak: similar to the case of low irradiation discussed in Section 2.3.1, two distinct peaks are not observed because the increase in MLR due to back surface insulation occurs simultaneously with the decrease in MLR due to the formation of a char layer. Note also that the magnitudes of the MLR peaks in Fig. 12 are approximately 3 to 4 times larger than those observed in Fig. 2.7 (top plot); this is due to the more rapid heating that is observed in thin and insulated materials. Furthermore, it is seen that the models present significant levels of disagreement: peak values of MLR vary by a factor 3, and burn out times by a factor of more than 5.

Figure 2.13 presents the spatial variations of x_{vs}, T_s and $\dot{\omega}_s'''$, at t = 9 s and for L = 0.6 mm. The heat distribution shown in Fig. 2.13(b) shows that as expected, the simulated PVC samples are close to thermally-thin conditions: the spatial variations of temperature across the depth of the sample are less than 100 degrees (except for model (GA-a) that shows a difference between front surface and back surface of approximately 200 degrees); these variations are much smaller than those presented in Fig. 2.10(b). Figure 2.13 also shows that there are significant levels of disagreement between the six PVC models: all models predict a distributed pyrolysis zone that spans across the entire depth of the sample; but while models (GA-c), (HCA-a), (HCA-b) and (HCA-c) predict quasi-uniform variations of $\dot{\omega}_s'''$ (i.e. relatively flat profiles), models (GA-a) and (GA-b) predict strong spatial variations of $\dot{\omega}_s'''$. In addition, predictions in PVC composition vary widely (Fig. 13(a)) and predictions in solid temperatures vary by 250 degrees (Fig. 2.13(b)).

Figure 2.14 presents a comparison of the simulated time variations of MLR as predicted using all six pyrolysis models, for L = 60 mm. The variations of MLR present a single peak: unlike the case of high irradiation discussed in Section 2.3.1, the positive effect of adiabatic insulation at the back surface is weak and does not lead to a second peak. Furthermore, it is seen that the models present moderate-to-high levels of disagreement: peak values of MLR vary by a factor 1.5, and burn out times by a factor of 2.3; these variations are larger than, but still comparable to those

observed in the calibration tests presented in Figs. 2.2 and 2.5.

Figure 2.15 presents the spatial variations of x_{vs}, T_s and $\dot{\omega}_s'''$, at t = 180 s and for L = 60 mm. Figure 15(a) shows that all models describe a similar build-up of a char layer near the exposed surface of the PVC sample (at x = 0); the thickness of the pyrolysis zone is on the order of 1 mm and at t = 180 s, the pyrolysis zone has propagated about 1.5-2 mm into the depth of the PVC sample (Fig. 15(c)). Consistent with results presented in Fig. 10(b), the models show significant differences in predictions of the heat distribution (Fig. 2.15(b)).

A sensitivity analysis (similar to that discussed in Section 2.3.1) was also carried out with the intent to understand the source of discrepancy between the different pyrolysis models at small and large values of the sample thickness L. It was found that for L = 0.6 mm, the response of PVC is strongly influenced by pyrolysis chemistry and that much of the discrepancy between the predictions of the different PVC pyrolysis models may be explained by the large variations in the values of A and E adopted by these models (Tables 2.2 and 2.3).

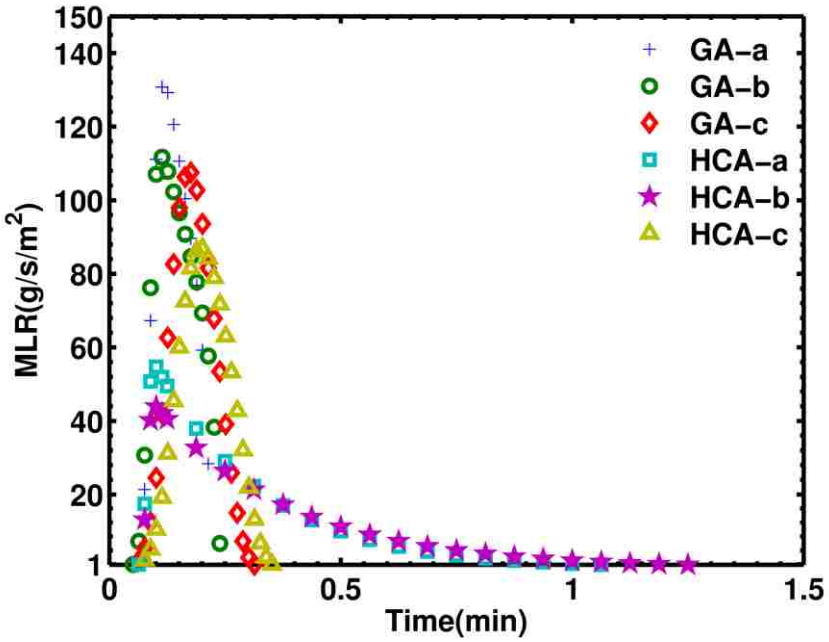

Figure 2-12. Cone calorimeter test: time variations of the fuel mass loss rate for a PVC sample subjected to 100 kW/m², 0.6 mm thick PVC sample and adiabatic back surface.

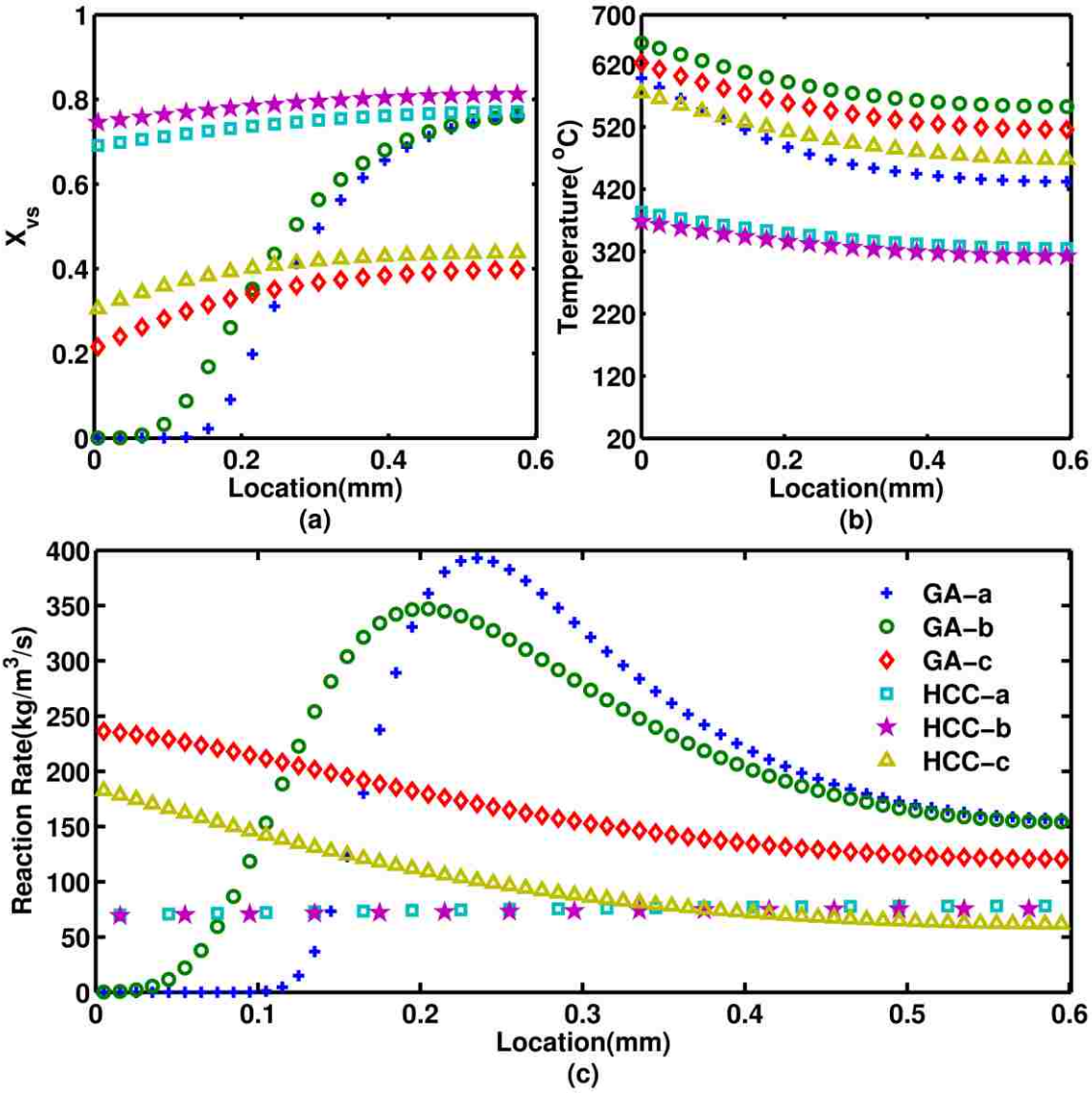

Figure 2-13. Cone calorimeter test: spatial variations of (a) the virgin solid volume fraction, (b) the solid temperature, (c) the pyrolysis mass reaction rate at t = 9 s for G = 100 kW/m², 0.6 mm thick PVC sample and adiabatic back surface.

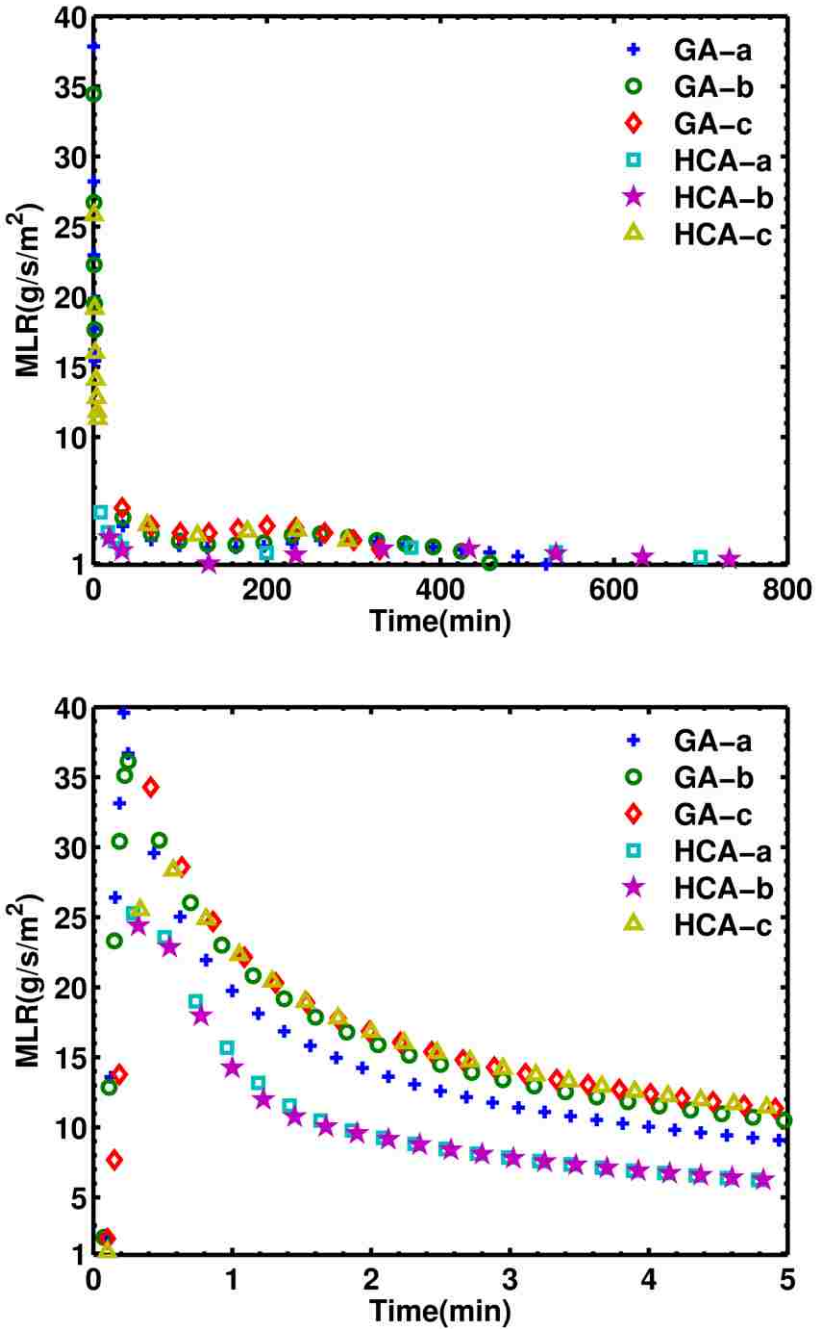

Figure 2-14. See caption of Fig. 2.12. Case L = 60 mm. Long time (top) and short time (bottom) evolution.

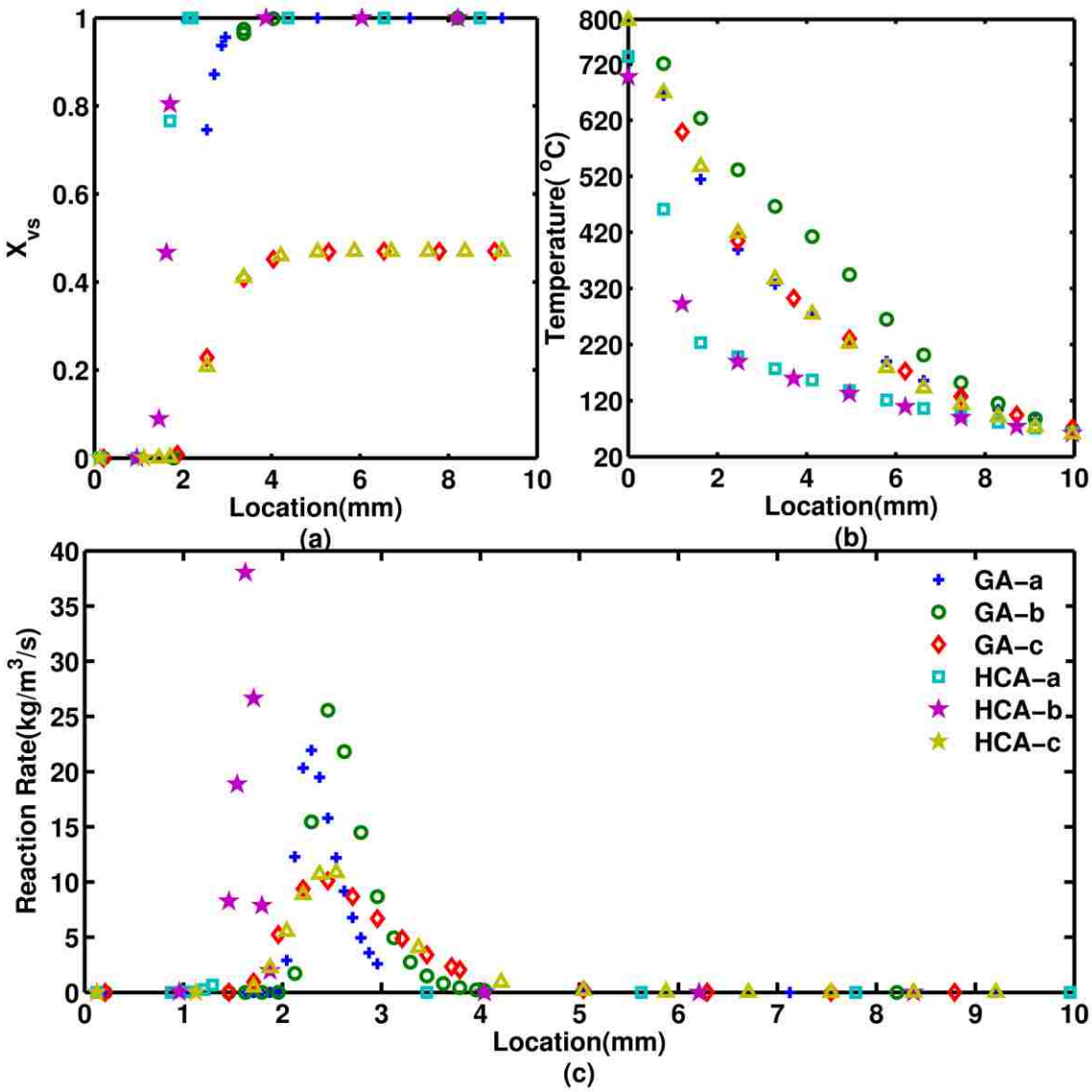

Figure 2-15. Cone calorimeter test: spatial variations of (a) the virgin solid volume fraction, (b) the solid temperature, (c) the pyrolysis mass reaction rate at t = 180 s for G = 100 kW/m², 60 mm thick PVC sample and adiabatic back surface.

2.4.3 Effect of changing the thermal boundary conditions

We assume here that L = 6 mm and that the irradiation from the radiant panel is G = 100 kW/m^2. The front and back surface thermal boundary conditions are modified in the following way: the heat flux at the exposed surface of the solid material (at x = 0) is given by Eq. (5) with a convective heat transfer coefficient h =

25 W/m^2/K; the heat flux at the back surface (at $x = L$) is given by a similar expression with $\varepsilon = 0$ (no radiation exchange), h = 25 W/m^2/K and $T_\infty = 570\,\mathrm{K}$. This case simulates a configuration in which the PVC sample, in addition to being exposed at the front surface to a strong radiant heat flux, is also exposed at the back surface (via convective heat transfer) to a hot ambient gas.

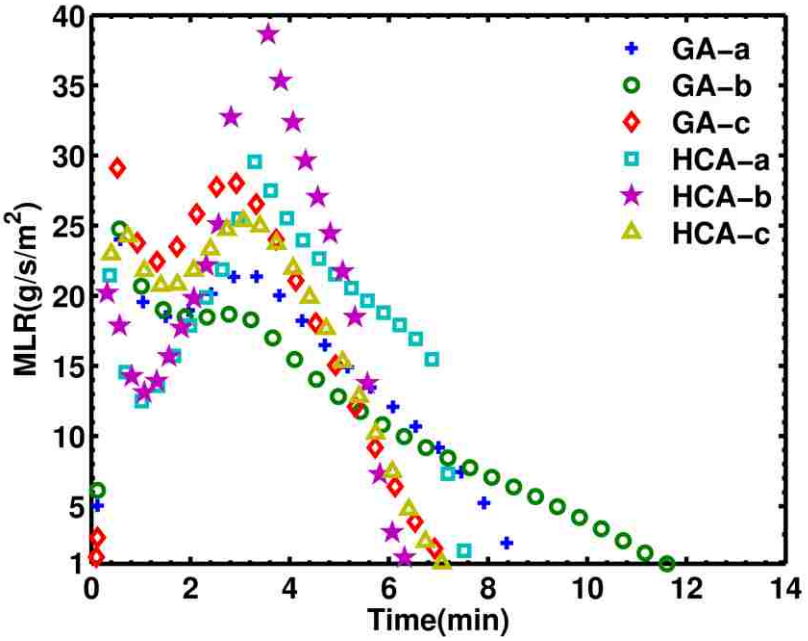

Figure 2-16. Cone calorimeter test: time variations of the fuel mass loss rate for a PVC sample subjected to 100 kW/m², 6 mm thick PVC sample and back surface exposed to 570 K ambient gas.

Figure 2.16 presents a comparison of the simulated time variations of MLR as predicted using all six pyrolysis models. It is seen that the models present significant levels of disagreement: first peak values of MLR vary by a factor 1.5, second peak values of MLR by a factor of more than 2, and burn out times by a factor 2.

Figure 2.17 presents the spatial variations of x_{vs}, T_s and $\dot{\omega}_s'''$, at t = 294 s and for G = 100 kW/m². Figure 2.17(c) shows that all models predict a relatively thick pyrolysis zone that spans across the deeper half of the PVC sample.

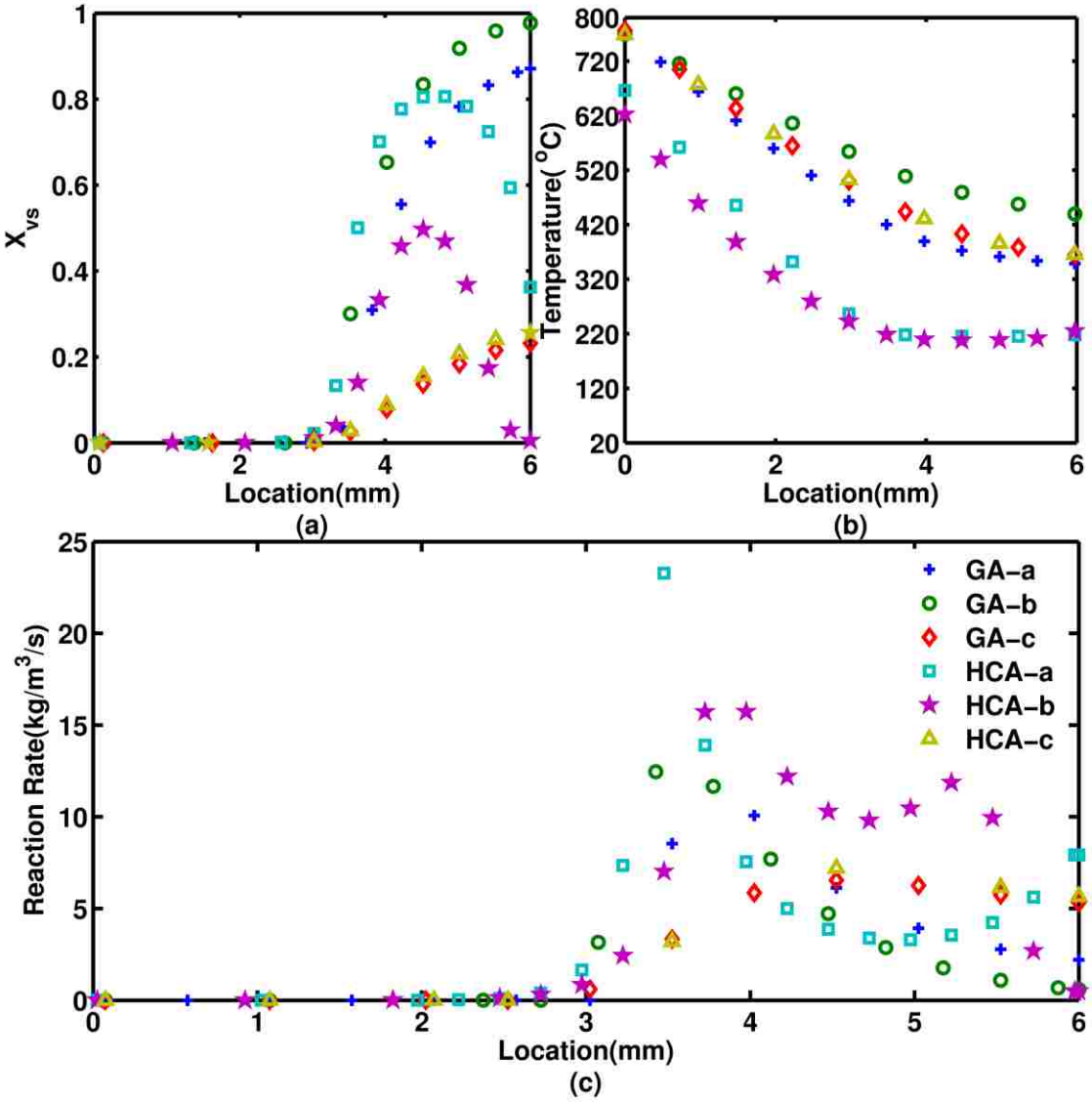

Figure 2-17. Cone calorimeter test: spatial variations of (a) the virgin solid volume fraction, (b) the solid temperature, (c) the pyrolysis mass reaction rate at t = 294 s for G = 100 kW/m², 6 mm thick PVC sample and back surface exposed to 570 K (297 °C) ambient gas.

Models (HCA-a) and (HCA-b) feature double-peak reaction rate profiles, which suggests that the decomposition of the PVC material is driven by thermal loading at both ends of the sample; for instance, at time t = 294 s, model (HCA-b) predicts the formation of a fully-charred layer at the back surface of the sample, $x_{vs} = 0$ at $x = L$. In contrast, model (GA-b) shows no sign of back surface degradation, $x_{vs} \approx 1$ at $x = L$.

Models (GA-a), (GA-c) and (HCA-c) show intermediate results with single-peak reaction rate profiles and a partially-charred layer at the back surface.

The results presented in Section 2.4 suggest that while MLR predictions from the six pyrolysis models agree within 10-30% for conditions corresponding to calibration tests (i.e. high values of the radiation intensity, thin samples, and thermally insulated back surface conditions), MLR predictions will show more pronounced discrepancies (and typically only agree within 100-300%) for conditions corresponding to low values of the radiation intensity, ultra-thin samples, and modified back surface boundary conditions. The importance of these discrepancies is now evaluated in the next section in a representative flame spread problem.

2. 5 Comparison between the PVC pyrolysis models in a vertical upward flame spread problem

We present below results from large eddy simulations (LES) of a representative flame spread configuration. The LES simulations are performed using the Fire Dynamics Simulator (FDS); FDS is a fire modeling software developed by the U.S. National Institute of Standards and Technology [36-37]. The numerical database consists in a series of six simulations; the numerical configuration corresponds to a turbulent flame spreading upward along a vertically-oriented PVC sheet; the numerical and modeling choices made in each simulation are identical except for the treatment of pyrolysis; pyrolysis is treated using the semi-empirical models presented in Section 2.3.

FDS is a Fortran 90, second-order accurate, finite difference solver with explicit time integration. The solver features multi-block, rectangular Cartesian grid, meshing capabilities; it also features a parallel computing capability using Message Passing Interface (MPI) protocols. FDS physical modeling capabilities include [36-37]: a low Mach number flow formulation; the classical Smagorinsky model for turbulence; the Eddy Dissipation Concept model for combustion; a simple yield model for soot formation; and a finite volume, radiative transfer equation (RTE) solver for thermal

radiation (with a choice between a gray medium model and a spectrally-resolved wide band model). In the present study, we use FDS version 5.5.1.

2.5.1 Numerical configuration

The numerical configuration is presented in Fig. 2.18. The configuration is inspired from the experimental set-up used in Ref. [37]. The vertical PVC sheet is 55 cm high (z-direction), 30 cm wide (x-direction) and 6 mm thick (y-direction); the PVC sheet is extended with two lateral Marinite panels (Marinite is a chemically inert, insulating material) and one top piece of sheet metal; the PVC/Marinite/sheet-metal assembly (referred to as the PVC panel hereafter) is 60 cm high and 40 cm wide. The PVC sheet is ignited using a high temperature solid device: the ignition device is rectangular-shaped (and is 5 cm high, 30 cm wide and 5 cm deep, see Fig. 18), is located at a y-distance of 5 cm from the bottom of the PVC sheet, and features one hot surface (facing the PVC sheet) with a constant uniform temperature equal to 1,073 K (800 degrees Celsius). The irradiation produced by the ignition device is approximately 30 kW/m^2 at the bottom of the plate. The PVC panel is also equipped with vertical side panels made of metal sheet; the side panels are located at $x = 0$ and $x = 40$ cm and act as flow barriers (Fig. 2.18).

The computational domain is 60 cm high, 40 cm wide and 50 cm deep. The y-size (50 cm) of the domain is chosen large enough so that air entrainment is not affected by inaccuracies associated with open flow boundary conditions. The PVC panel is located at $y = 0$; the floor (at $z = 0$) is a solid boundary (and is treated as isothermal at ambient temperature); the $y = 50$ cm and $z = 60$ cm boundaries are open boundaries and play the role of inflow and outflow boundaries, respectively (Fig. 2.18).

The computational grid corresponds to a near-wall block ($0 \leq y \leq 15$ cm) with the highest resolution and an outer layer block ($15 \leq y \leq 50$ cm) with a coarser resolution. The near-wall resolution corresponds to $\Delta y = 0.5$ cm and $\Delta x = \Delta z = 1$ cm; the outer layer resolution is twice coarser, $\Delta y = 1$ cm and $\Delta x = \Delta z = 2$ cm; the total number of grid cells is 93,000. The choice of a relatively small near-wall grid spacing ($\Delta y = 0.5$

cm) comes from the intent to perform wall-resolved LES simulations, *i.e*. simulations in which the near-wall region of the boundary layer flame is grid-resolved and wall gradients are described with suitable accuracy. Note that the boundary layer flame has a thickness on the order of 1 cm and wall-resolved simulations are expected to require near-wall grid spacing on the order of 1 mm. The value of Δy adopted in the present study came from a separate grid convergence study in which the grid was systematically refined and the solution was carefully monitored for changes.

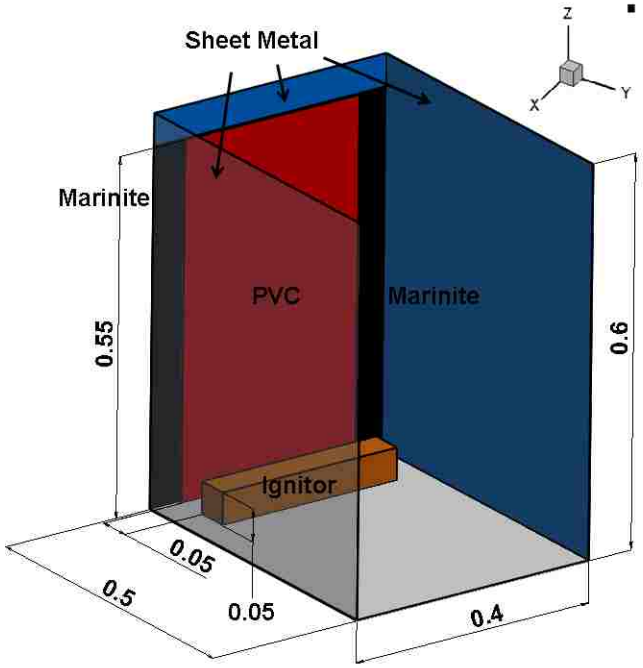

Figure 2-18. Numerical configuration corresponding to bottom ignition of a vertical PVC sheet. Dimensions are given in meters.

Figure 2.19 presents a typical result from this study in the form of the time variations of the local fuel mass loss rate at a particular PVC sheet location (located on the vertical centerline of the PVC sheet and at an elevation z = 5 cm). Figure 2.19 shows that while the results from coarse grid simulations (Δy = 5 cm and Δy = 2.5 cm) are grid-sensitive, predictions become approximately grid-independent provided that the near-wall grid resolution is 1 cm or smaller. These results suggest that Δy = 0.5 cm is an acceptable choice for near-wall resolution in the present wall-resolved simulations.

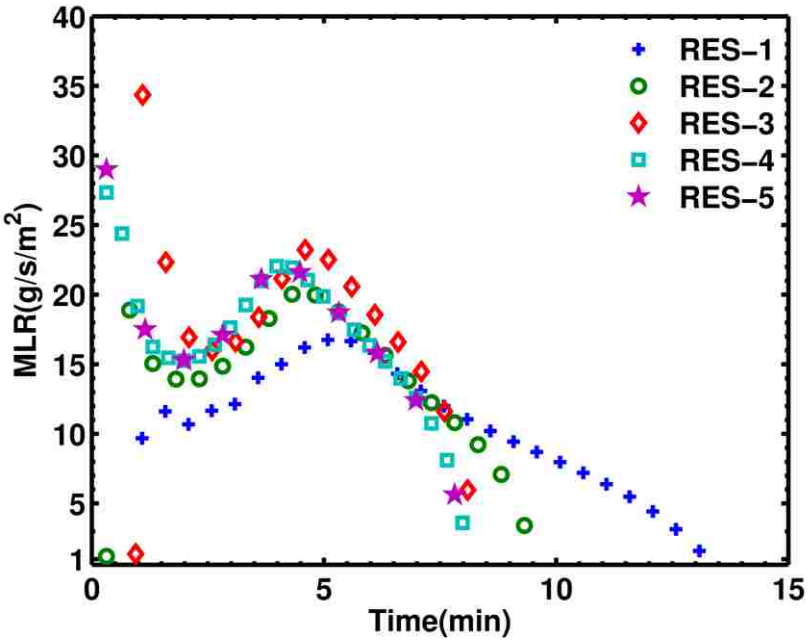

Figure 2-19. Flame spread test: time variations of the fuel mass loss rate evaluated on the centerline of the PVC sheet and at an elevation z = 5 cm. Comparison between difference levels of grid resolution: $(\Delta x, \Delta y, \Delta z) = (5,5,5)$ cm (RES-1); $(\Delta x, \Delta y, \Delta z) = (2.5,2.5,2.5)$ cm (RES-2); $(\Delta x, \Delta y, \Delta z) = (1,1,1)$ cm (RES-3); $(\Delta x, \Delta y, \Delta z) = (0.5,0.5,0.5)$ cm (RES-4); $(\Delta x, \Delta y, \Delta z) = (1,0.5,1)$ cm (RES-5).

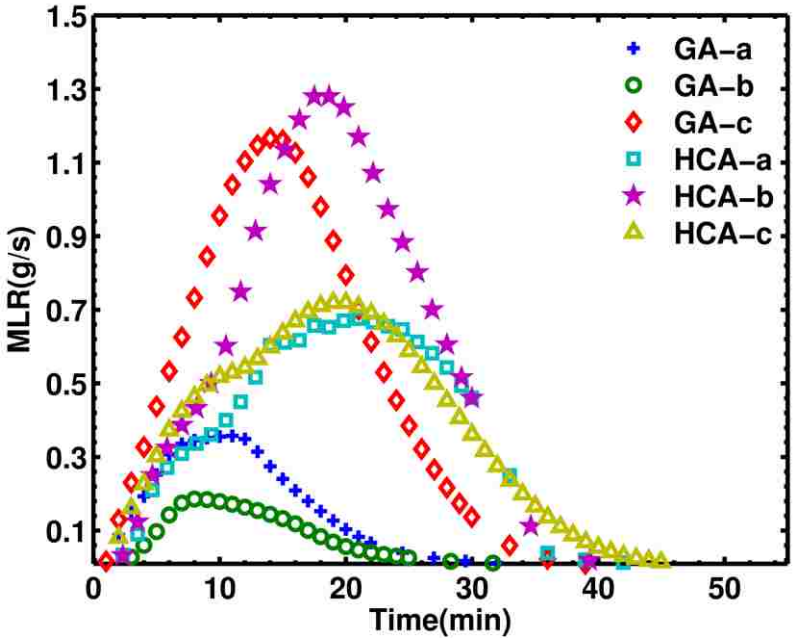

Figure 2-20. Flame spread test: time variations of the total fuel mass loss rate.

The simulations are performed using the Eddy Dissipation Concept combustion model and assuming single-step global combustion chemistry. The PVC fuel vapors are described as C_2H_3Cl with chlorine treated as an inert chemical species; the soot yield is 17.2%, the *CO* yield is 7.2% and the heat of combustion is 14.4 MJ/kg [22, 30, 39]. Thermal radiation is treated assuming a grey medium. Furthermore, the simulations are performed using the pyrolysis models discussed in Sections 2 and 3; the thickness of the PVC sheet is L = 6 mm; the back surface is treated as adiabatic.

2.5.2 Result

Figure 2.20 presents a comparison of the simulated time variations of MLR as predicted using all six pyrolysis models. It is seen that the models present high levels of disagreement: peak values of MLR vary by a factor of more than 8 (model (HCA-b) predicts a peak value of approximately 1.3 g/s while model (GA-b) predicts 0.15 g/s); the times to peak MLR value vary by a factor of more than 2; and burn out times vary by a factor 1.5. Assuming that all the fuel released from the PVC sheet burns in the wall flame, it is seen that models (HCA-b) and (GA-c) correspond to maximum burning intensities (peak values of HRR are approximately 17-19 kW); models (HCA-c) and (HCA-a) correspond to moderate burning intensities (peak values of HRR are approximately 8.5-10 kW); and models (GA-a) and (GA-b) correspond to low burning intensities (peak values of HRR are below 5 kW). Note that the simulated combustion intensities are relatively low and that fire conditions remain close to critical conditions required for sustained burning and flame spread.

A different perspective is adopted in Fig. 2.21: the figure presents the spatial variations of the local burning efficiency measured on the vertical centerline of the PVC sheet and as a function of elevation *z*. The local burning efficiency is defined as:

$$\zeta(x_{PVC}, z_{PVC}) = \frac{\int_{t_{ign}}^{t_{bo}} \dot{m}''_f(t)dt}{\rho_{s,0}\eta_v L} \tag{10}$$

where x_{PVC} and z_{PVC} designate spatial coordinates on the exposed surface of the PVC sheet. The burning efficiency ζ compares the total release of flammable PVC vapors (measured from ignition to burn out) to the value that is obtained when pyrolysis processes go to completion (as was the case in the cone calorimeter tests of Section 2.4): ζ takes values between 0 and 1 ($\zeta = 0$ when pyrolysis is not active; and $\zeta = 1$ when pyrolysis is active and sustained up to total fuel depletion); ζ provides a convenient measure of deviations from complete pyrolysis.

Table 2.4 also presents results obtained in each simulation for the global burning efficiency:

$$\zeta_g = \frac{\iint \zeta(x_{PVC}, z_{PVC}) dx_{PVC} dz_{PVC}}{A_{PVC}} \tag{11}$$

where integration on the RHS of Eq. (11) takes place over the entire surface of the PVC sheet and where A_{PVC} designates the surface area of the sheet.

Mass loss	GA-a	GA-b	GA-c	HCA-a	HCA-b	HCA-c
m_f (kg)	0.310	0.157	1.171	0.923	1.383	1.010
$m_{f,max}$ (kg)	1.319	1.342	1.302	1.414	1.386	1.226
ζ_g	0.235	0.117	0.900	0.653	0.998	0.824

Table 2-4. Flame spread test: comparison between the different predictions for the total mass loss. m_f is the simulated total mass loss; $m_{f,max}$ is the value of m_f that is obtained when pyrolysis processes go to completion, $m_{f,\max} = (\rho_{s,0} \eta_v L A_{PVC})$; ζ_g is the global burning efficiency, $\zeta_g = (m_f / m_{f,\max})$ (see Eq. 11).

Figure 2.21 and Table 2.4 show that the different pyrolysis models present high levels of disagreement: while model (HCA-b) predicts a successful flame spread fueled by a nearly complete pyrolysis process (Table 2.4 indicates that 99.8% of the initial virgin solid PVC mass is transformed into pyrolysis products, *i.e*. flammable volatiles and char), model (GA-b) predicts no flame spread and a pyrolysis process limited to the vicinity of the ignition device (only 11.7% of the initial virgin solid PVC mass is transformed into flammable volatiles and char). Table 2.4 also shows

that models (GA-a), (GA-c), (HCA-a) and (HCA-c) correspond to intermediate regimes in which fuel depletion is partial and values of ζ_g range between 23.5% and 90%.

Yet another perspective is adopted in Figs. 2.22 and 2.23. Figure 2.22 presents the time variations of the pyrolysis front height x_p, defined as the highest location along the vertical centerline of the PVC sheet at which the local fuel mass loss rate reaches the critical value of 1 g/m^2/s. The upward rate of spread of the vertical flame may be defined as the time derivative of x_p.

Figure 2.22 suggests that flame spread may be characterized by the following sequence of events: an initial induction phase ($x_p \approx 5$ cm) during which the ignition device thermally loads the bottom of the PVC sheet and establishes a small base flame; a flame spread phase (x_p increases from 5 to 55 cm) during which the pyrolysis region extends (both vertically and horizontally) and the wall flame intensifies; a burn out phase ($x_p = 55$ cm) during which pyrolysis and combustion are sustained for a certain time. In all cases except (GA-b), the induction phase lasts for approximately 3 minutes; in (GA-b), PVC temperatures remain sub-critical and transition to a flame spread phase is not observed. Figure 2.22 shows that the fastest vertical spread is obtained with model (GA-c), followed by models (HCA-c), (HCA-b) and (HCA-a); this ranking is consistent with that observed in Fig. 20 when considering the early variations of the fuel mass loss rate (at time $0 \le t \le 10$ minutes).

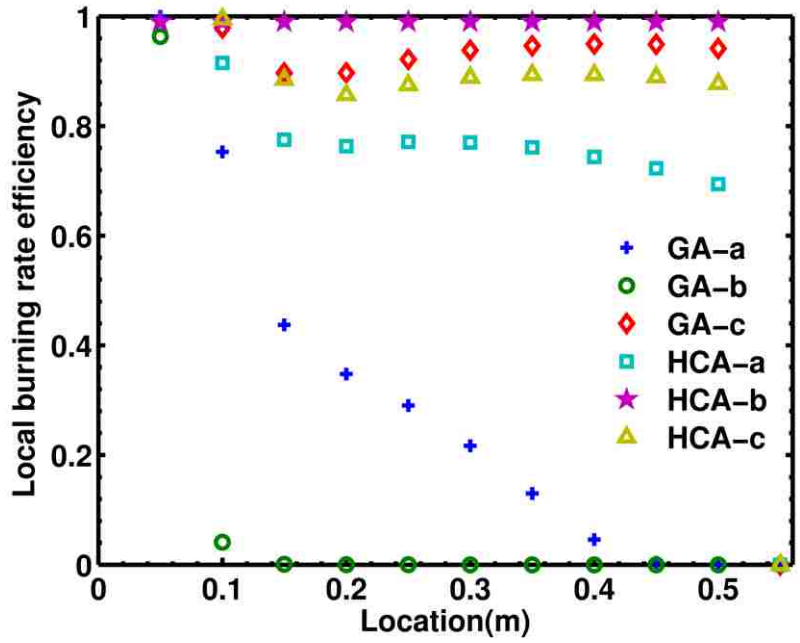

Figure 2-21. Flame spread test: centerline variations of the local burning efficiency ζ (a non-dimensional measure of the local mass loss, see Eq. 10) with respect to elevation z.

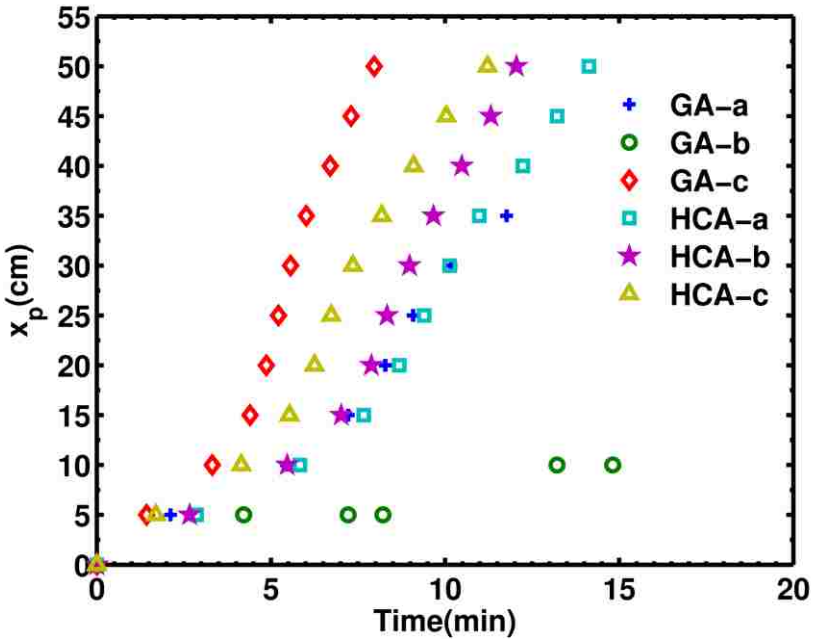

Figure 2-22. Flame spread test: time variations of the pyrolysis front height.

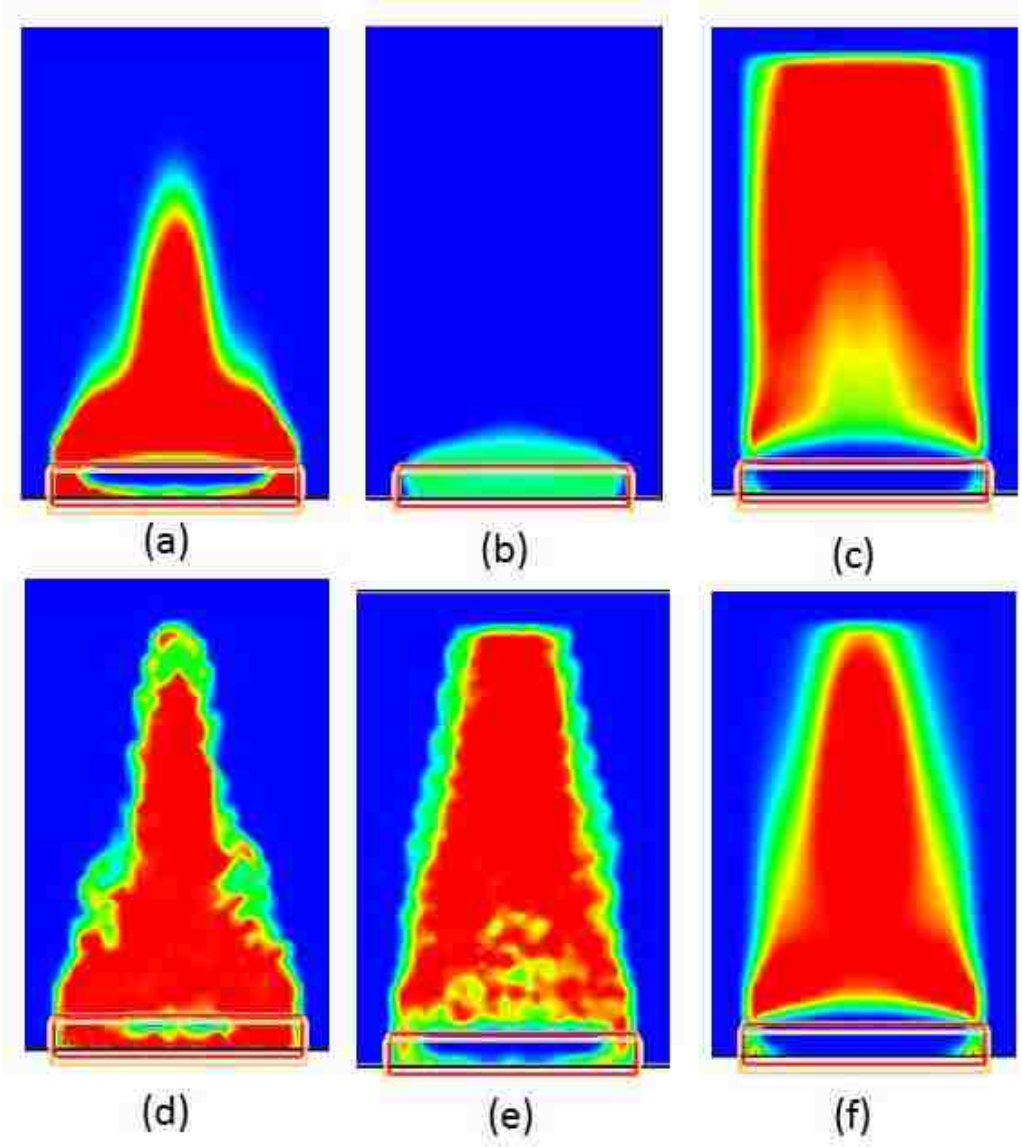

Figure 2-23. Flame spread test: instantaneous snapshot showing the spatial distribution of the fuel mass loss rate on the PVC sheet surface. Time t = 15 min; (a) (GA-a); (b) (GA-b); (c) (GA-c); (d) (HCA-a); (e) (HCA-b); and (f) (HCA-c).

Figure 2.23 provides a graphical representation of the extent and speed of flame spread, in the form of an instantaneous distribution of $\dot{m}''_f$ along the PVC sheet. Consistent with results of Fig. 2.22, at t = 15 min (900 s), cases (GA-c), (HCA-c) and (HCA-b) have reached the burn out phase, whereas cases (HCA-a) and (GA-a) are still in the flame spread phase, and case (GA-b) is in the induction phase. Note that

models (HCA-a) and (HCA-b) lead to a noisy distribution of $\dot{m}''_f$: these numerical oscillations are due to the assumption of zero activation energy combined with the adoption of a threshold temperature.

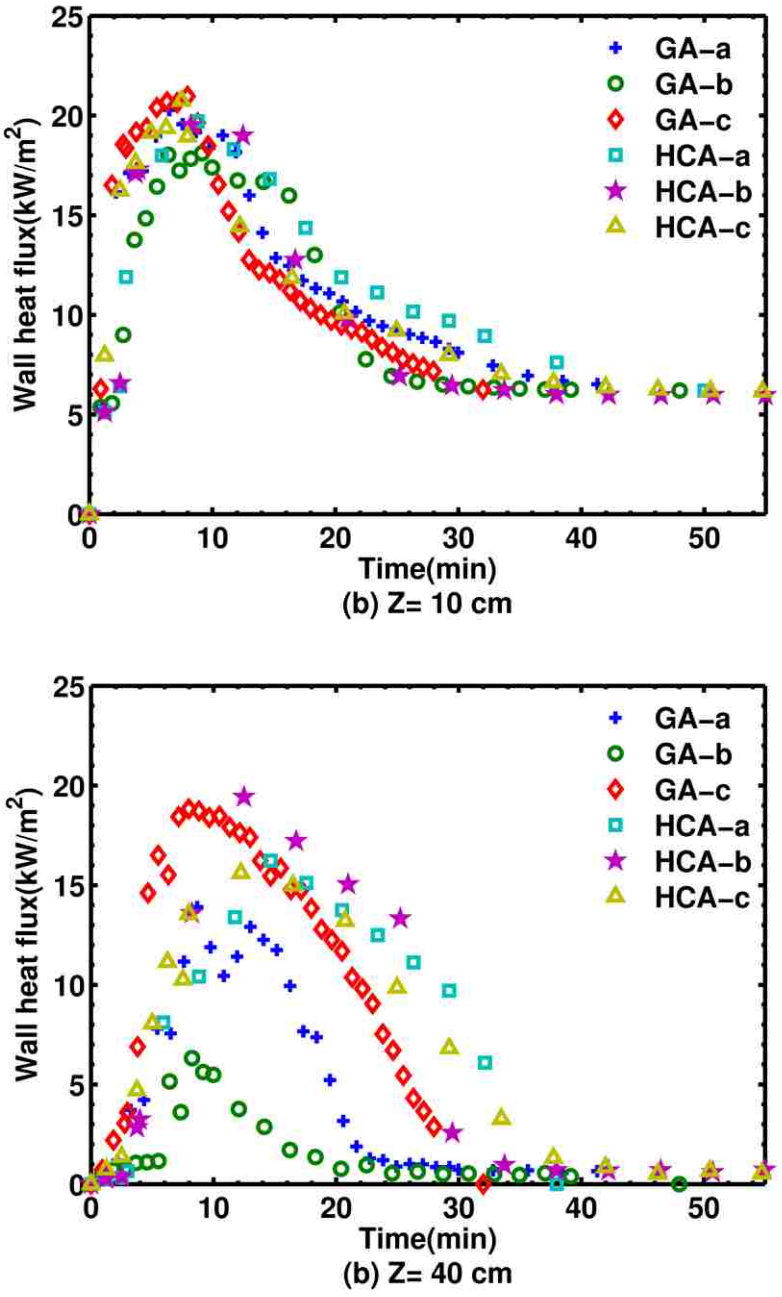

Figure 2-24. Flame spread test: time variations of the gauge heat flux measured on the centerline of the PVC sheet and at two different elevations: (a) z = 10 cm; (b) z = 40 cm.

Figure 2.24 presents the time variations of the gauge heat flux measured on the vertical centerline of the PVC sheet and at two different elevations. The gauge heat flux is defined as the irradiation from the wall flame plus the convective heat flux, and provides a measure of the thermal loading experienced by the PVC sheet. Simulated values of the convective heat flux range between 4.5 and 7.5 kW/m². Figure 24 shows that the values of the intensity of the thermal loading in the present flame spread problem are relatively low (peak values of the gauge heat flux range between 10 and 20 kW/m^2) and are significantly lower than those used in the cone calorimeter tests of Section 2 (where G = 75 kW/m^2 and 92 kW/m^2).

This now leads to a possible explanation of the large variations in predicted PVC burning behavior that were observed in Fig. 2.20: as discussed in Sections 2.3 and 2.4, the pyrolysis models have been calibrated using relatively high values of the radiation intensity; the flame spread problem, however, is characterized by moderate-to-low values of the thermal feedback (Fig. 2.24) and these conditions lie outside of the domain of calibration of the models; this ,in turn, leads to a significant loss of model accuracy (in Section 2.4, the pyrolysis models have been shown to lead to inconsistent predictions for conditions corresponding to low values of the radiation intensity, see Fig. 2.7).

In order to further examine this proposed explanation, we perform two new cone calorimeter simulations, for G = 12.5 kW/m^2 and 17.5 kW/m^2. These levels of G correspond to representative average values of the gauge heat flux at z = 10 and 40 cm (see Fig. 2.24). Figure 2.25 shows that at these low levels of the thermal loading, models (HCA-b) and (GA-c) predict relatively high values of MLR (i.e., peak MLR values on the order of 10 g/s/m^2); models (HCA-c), (HCA-a) and (GA-a) predict moderate values (i.e., peak MLR values between 5 and 10 g/s/m^2); and model (GA-b) predicts critically low values (i.e., peak MLR values below 5 g/s/m^2) that are unlikely to be large enough for sustained burning and flame spread. In addition, Figure 2.7 shows that models (GA-a) and (GA-b) are quite sensitive to the value of G: for G = 10 kW/m^2, model (GA-a) predicts critically low values of MLR, while model (GA-b) predicts no ignition.

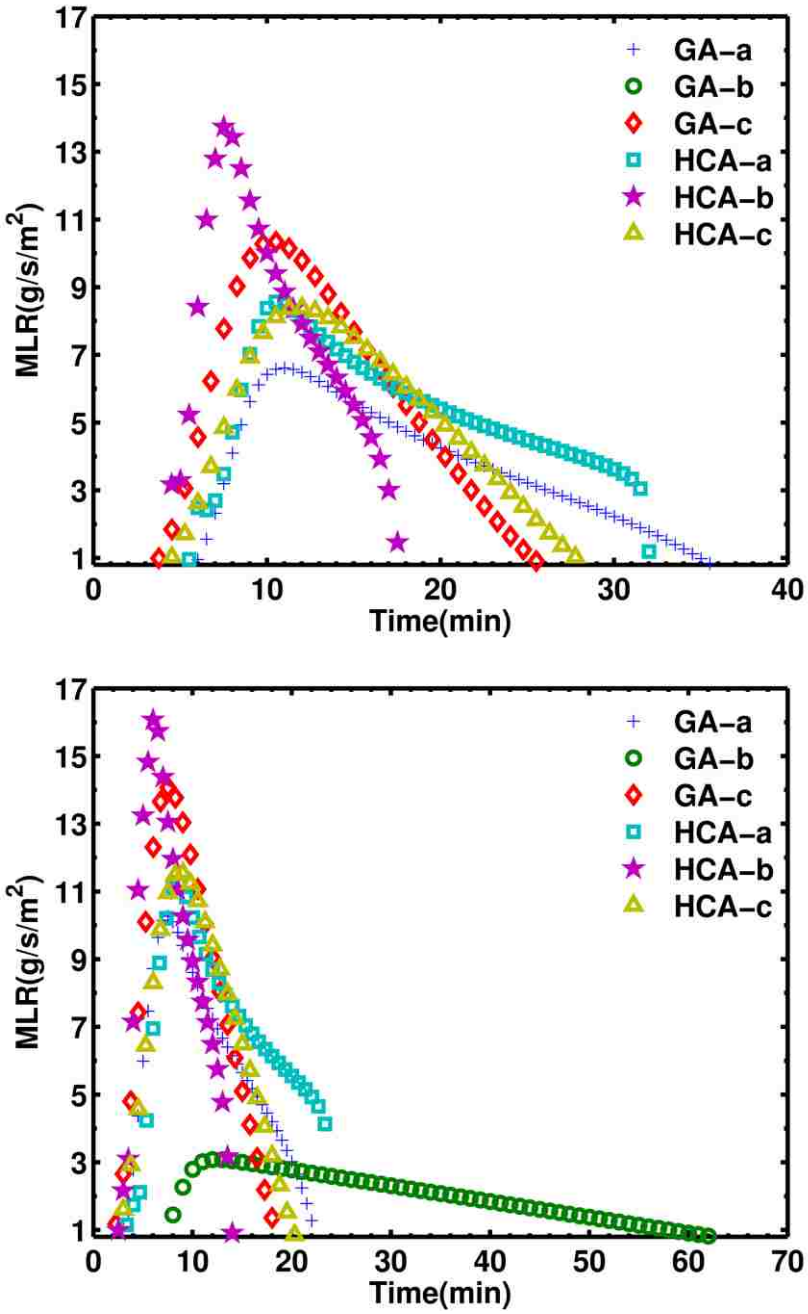

Figure 2-25. Cone calorimeter test: time variations of the fuel mass loss rate for a PVC sample subjected to 12.5 kW/m² (top) and 17.5 kW/m² (bottom); L = 6 mm; adiabatic back surface.

Combined together, these results are consistent with the conflicting flame spread predictions observed in Fig. 2.20. If one uses peak MLR values obtained in the cone calorimeter tests of Figs. 7 and 25 in order to establish a ranking between all the

models, one finds that: models (HCA-b) and (GA-c) produce the largest flames; models (HCA-c) and (HCA-a) produce smaller flames; and models (GA-a) and (GA-b) produce even smaller flames that may not spread. This ranking is consistent with the flame spread results presented in Fig. 2.20. Note also that these results support the usual assumption made in fire research that bench scale data can be extrapolated to full scale fire problems (provided that the intensity of the thermal feedback is similar in both configurations).

2.6 Conclusion

The general objective of the present study is to evaluate the predictive capability of pyrolysis models based on a calibrated semi-empirical approach. We consider the case of polyvinyl chloride (PVC) and first develop six different models to simulate PVC pyrolysis. The development is based on: a standard one-dimensional model formulation used to describe heat and mass dynamics inside the PVC material combined with global one-step pyrolysis chemistry; cone calorimeter test data used for model calibration; and two parameter estimation techniques used to optimize the model calibration process. The six models that are produced are different but provide similar mass loss rate predictions for conditions corresponding to calibration test data (i.e. high values of the radiation intensity, $G > 50$ kW/m^2, relatively thin samples, $L =$ 6 mm, and thermally insulated back surface conditions).

We then present a comparison of predictions made by the six PVC pyrolysis models in a series of cone calorimeter tests and for conditions that are significantly different from those used during model calibration, in particular at low values of the radiation intensity and for different thicknesses of the PVC samples, Predictions from the six PVC pyrolysis models show pronounced discrepancies, most notably for conditions corresponding to low values of the radiation intensity and ultra-thin samples. These results suggest that the predictive capability of the pyrolysis models is limited. One important factor in this limitation is the fact that in the present study, the models are calibrated at high values of the thermal loading, i.e. under conditions for

which the PVC response is limited by transport processes and is relatively insensitive to details of the pyrolysis chemistry, while the domain of application of the models is likely to include conditions of moderate-to-low values of the thermal loading, i.e. conditions for which decomposition chemistry play a dominant role.

This point is further illustrated through a comparison of predictions made by the PVC pyrolysis models in a vertical upward flame spread problem. The flame spread problem is characterized by low values of the thermal feedback (values of the gauge heat flux vary between 10 and 20 kW/m^2), i.e. conditions that lie outside of the domain of calibration of the pyrolysis models. The six PVC pyrolysis models are found to produce conflicting predictions: two models predict successful flame spread with quasi complete pyrolysis (i.e., total PVC burn out); three models predict successful flame spread with partial pyrolysis (i.e., leaving a significant amount of unburnt PVC); and one model predicts no flame spread (i.e., no flame propagation beyond the ignition region). The large variations in the predicted burning behavior suggest that the models have limited value when applied to flame spread problems because of uncertainties in their level of accuracy.

Thus, the domain of validity of semi-empirical pyrolysis models is limited to the set of conditions that are used during model calibration. This may be an unacceptable restriction for models intended for general-purpose use, especially given the fact that the exact domain of validity of the proposed pyrolysis models remains typically unspecified. This restriction may be overcome in several ways. One way is to adopt a more comprehensive strategy for model calibration, for instance by using thermo-gravimetric analysis (TGA) data, differential scanning calorimetry (DSC) data, and/or simultaneous thermal analysis (STA) data in addition to bench-scale data (cone calorimeter or fire propagation apparatus). A more comprehensive strategy for model calibration may also require better instrumented bench-scale tests, for instance tests that produce in-sample solid temperature data (e.g., front and back surface temperature data) in addition to mass loss rate data. The present study also suggests that it is important to include data from cone calorimeter tests performed with low values of the radiation intensity, preferably below 20 kW/m^2.

Finally, it is worth emphasizing that while semi-empirical models provide a cost-effective approach to pyrolysis modeling and are an attractive option for engineering-level fire modeling applications, the present study also suggests that there is a strong need to develop more fundamental approaches that rely on detailed descriptions and accurate estimates of "true" physical and chemical properties. Detailed comprehensive pyrolysis models are the preferred approach for a general-purpose treatment of pyrolysis.

Chapter 3 : A Numerical Study of Solid Fuel Pyrolysis under Time Dependent Radiant Heat Flux Conditions

3.1 Summary

The present study examines the effect of time dependent irradiation on pyrolysis processes. The pyrolysis process generally takes place in a strongly unsteady environment and consequently the gas-to-solid rate of heat transfer features strong unsteady variations. In some cases, the variations of the gas-to-solid heat flux may result in significant variations of the fuel mass loss rate. This aspect is usually overlooked in experimental, theoretical, or numerical analysis in which a quasi-steady point of view is often adopted.

We examine in the present study the effects of fluctuating incident radiant heat exposure on the pyrolysis processes taking place inside solid flammable materials. The study uses a simple one-dimensional numerical model. The pyrolysis model formulation is based on standard conservation statements for heat and mass, coupled with a global one-step finite-rate decomposition chemistry model that can be applied to both non-charring and charring materials. The model allows for constant or time-varying radiant exposures. We consider in the present study harmonic periodic variations in irradiation characterized by a mean value, an amplitude and a frequency. The responses of polymethyl methacrylate (PMMA) and polyvinyl chloride (PVC) samples are analyzed in terms of the amplitude of the fluctuations in both solid temperature and fuel mass loss rate. Results indicate that the response of charring and non-charring materials is quite different. In the case of PMMA, the effects of time-varying radiant exposure are pronounced during the entire pyrolysis process, from ignition to burn-out. In contrast, in the case of PVC, the effects of time-varying radiant exposure are only pronounced during a limited time. This limited time corresponds to a regime in which the pyrolysis front is within a certain spatial

distance of the exposed surface of the material. The analysis leads to an evaluation of the importance of unsteady heat flux effects on pyrolysis processes.

3.2 Introduction

Computer simulation as an engineering tool provides the potential for predicting flame spread and fire growth in real-world geometries. There is a significant interest in the modern fire research community to use Computational Fluid Dynamics-based fire simulation as it provides a cost-effective alternative to expensive full-scale fire tests. It can also provide a fundamental understanding of material flammability and fire growth as opposed to conducting full-scale tests for every possible combination of test parameters and geometries [28].

Broadly speaking, flame spread is a transient phenomenon consisting of interactions between the gas phase and the solid phase. During this process, the solid is subjected to an external heat flux, i.e. in the form of radiation coming from flames or another source at ignition. As a result, the surface temperature of the solid begins to rise and heat is transported inside the slab by thermal conduction. When the temperature reaches the pyrolysis temperature, the solid begins to decompose and undergoes thermal degradation (pyrolysis). Solid pyrolysis corresponds to the transformation of carbon and hydrogen matter from the solid phase into flammable vapors that fuel the combustion process. These flammable gases flow out of the solid, due to the pressure gradient generated at the pyrolysis zone, mix with air and undergoes combustion in the gas phase. More precisely, this process features a closed-loop heat feedback mechanism, where a large amount of heat is released by gaseous combustion and is then transferred to the surrounding unburnt solid by radiation and convection ahead of the flame. This, in return, produces more flammable gas during the pyrolysis of the solid, to burn and leads to a larger turbulent flame.

Flame spread and fire growth are determined by interactions between pyrolysis, gas phase combustion, radiation, and turbulent flow. Therefore, accurate prediction of these phenomena using Computational Fluid Dynamics-based fire models requires

several sub-models for simulation of the gaseous phase and the condensed phase. In many fire scenarios, solid materials make up a substantial amount of the fuel loads. Understanding the processes involved in the pyrolysis of condensed phase fuels is important to characterize ignition, growth, and the production rate of flammable vapor. Thus, a condensed phase pyrolysis sub-model that accurately predicts the temperature and volatile release rate is essential for CFD-based fire modeling. The fuel release rate is the amount of gaseous fuel generated by thermal degradation of the solid material and it determines the intensity of the combustion process. Radiative and convective heat fluxes from the flame can be calculated and the effect of the flame on the materials in the surrounding environment can be determined.

A significant amount of experimental and theoretical studies have been conducted over the past few decades for the analysis and prediction of pyrolysis processes of both charring and non-charring materials [15–21]. Materials are classified into two categories: (1) solids which leave a considerable amount of char after the pyrolysis process as residue, e.g. wood, referred to as charring materials; and (2) solids that do not leave residue behind after the pyrolysis process, e.g. polymethyl methacrylate (PMMA), referred to as non-charring materials.

Pyrolysis models feature a variety of approaches and may be categorized as: 1) fully empirical models in which the evolution of the fuel mass loss rate is prescribed based on data obtained in reference bench-scale or furniture calorimeter experiments; or 2) semi-empirical or comprehensive models that are based on detailed descriptions of the many physical and chemical processes that occur inside solid fuel sources in response to the gas-to-solid thermal loading [14–19]. Comprehensive models can be further categorized based on the reaction scheme used to describe the conversion of solid material to production of gaseous fuel during the pyrolysis process: (a) one-step global reaction; (b) one-step multiple reaction under which the solid fuel decomposes through multiple consecutive first order reactions; (3) multi-step semi-global reaction through which multiple elementary reactions occurs simultaneously. Typically, an Arrhenius type expression is used to model the reaction of chemical kinetics. Semi-empirical models correspond to an intermediate approach based on simplified

descriptions of in-solid heat transfer and chemical processes [17–19]. These cost-effective models rely on a number of simplifications, e.g. infinitely fast or global single-step pyrolysis chemistry, the assumption of a single-phase homogeneous medium, etc.

Semi-empirical or comprehensive models have several advantages and eliminate many restrictions placed on the other models in terms of simplifying assumptions. However the increased complexity has an inevitable drawback: these models requires a set of material properties to properly calculate the amount of released pyrolysis gases under an incident heat flux. These inputs include the kinetic parameters (reaction order, pre-exponential factor and activation energy), thermal properties (specific heat capacity, thermal conductivity and density) of pyrolysis products, and radiative characteristics (surface emissivity, in-depth radiation absorption coefficient). Optimization techniques, developed over the past decade due the lack of measured material properties, generate material properties in an iterative process under a prescribed calibration phase. The reader is referred to [16] for a more detailed discussion of thermal and comprehensive pyrolysis models.

As discussed earlier, the thermal feedback from the flame is the driving mechanism of the pyrolysis process. Recent experimental and numerical studies on the pyrolysis process have focused only on a constant incoming heat flux. However, in most fire scenarios, the flame grows in size and becomes turbulent. The turbulent gaseous flow is characterized by random, fluctuating movements and consists of eddies with differing time and length scales. The influence of these turbulent fluctuations is pronounced on radiative heat flux and consequently the gas-to-solid rate of heat transfer features strong unsteady variations. As a result, the pyrolysis process takes place in a strongly unsteady environment. This aspect is usually overlooked in experimental, theoretical, or numerical analysis in which a quasi-steady point of view is often adopted.

In the present study, the effect of fluctuations in incident radiant heat exposure on the pyrolysis processes was examined. The paper is organized as follows: Section 3.3 contains a description the pyrolysis model employed in this study. The pyrolysis

model formulation is based on standard conservation statements for heat and mass, coupled with a global one-step finite-rate decomposition chemistry model that can be applied to both non-charring and charring materials. The pyrolysis model allows for constant or time-varying radiant exposures. The material properties and chemical reaction parameters used in the pyrolysis model have been previously calibrated based on an optimization technique to represent thermal degradation of polymethyl methacrylate (PMMA) and polyvinyl chloride (PVC). A mathematical solution to a reference analog problem corresponding to heat conduction in a semi-infinite solid thermally loaded by an unsteady heat flux is used as the basis for data analysis. The analytical model was further modified to predict the amplitude of temperature and mass loss rate fluctuations for time dependent radiant exposure. Section 3.4 contains the study of the pyrolysis behavior of PMMA and PVC where the radiation intensity is excited. The response of the PMMA and PVC samples under harmonic periodic variations in irradiation was analyzed in terms of the amplitude of the fluctuations in both solid temperature and fuel mass loss rate. In addition, a sensitivity analysis was carried out in an attempt to understand the relative importance of the unsteady radiant heat flux parameters on the overall trend of mass loss rate time history, namely amplitude of front surface temperature and regression rate fluctuations. In Section 3.5, the findings of this study and plans for future work are summarized.

3.3 Methodology

3.3.1 Pyrolysis model

The present study considers a classical pyrolysis model that is similar to the experimental configuration studied in cone calorimeter tests. The pyrolysis model treats the thermal degradation across a solid as a local one-dimensional problem in the direction normal to the exposed solid surface. The model formulation is based on the classical conservation statements for heat and mass and is adopted from Ref [20]. The model employs a control volume approach and allows for sample shrinkage or swelling. An Arrhenius-like thermal degradation chemistry is assumed based on a global one-step pyrolysis reaction with virgin solids transformed into volatiles and

char. The main equations of the model formulation based on finite volume formulation are:

$$\frac{\partial(\rho_s \Delta y)}{\partial t} = -\dot{\omega}_{sg}''' \Delta y \tag{1}$$

$$\frac{\partial(\rho_s Y_{vs} sy)}{\partial t} = -\dot{\omega}_{d}''' \Delta y \tag{2}$$

$$\frac{\partial(\rho_s c_s T_s \Delta y)}{\partial t} = \Delta y \left(k_s \frac{\partial T_s}{\partial y} \right) - \dot{\omega}_{d}''' \Delta y \Delta H_R \tag{3}$$

where ρ_s, c_s, k_s and T_s designate the mass density, heat capacity, thermal conductivity and temperature of the solid material, *y* is the spatial coordinate normal to the exposed surface, Δy is the cell size, $\dot{\omega}_{sg}'''$ is the volumetric formation rate of volatiles from the condensed phase (i.e. the amount of virgin solid mass transformed into gas by pyrolysis processes per unit time per unit volume), $\dot{\omega}_{d}'''$ is the volumetric destruction rate of condensed species), and ΔH_R is the heat of pyrolysis. The thermal properties which include density, heat capacity, thermal conductivity, and emissivity are weighted by the condensed phase mass fraction.

Equation (1) and equation (2) describe the solid phase mass conservation equation and solid phase mass species conservation equation. Equation (1) together with equation (2) describes solid mass loss due to phase change and the associated production of flammable vapors. Equation (3) represents the conservation of energy for the condensed phase.

The total destruction rate of solid material was formulated using an Arrhenius-like expression, shown in equation (4a). In equation (4a), Y_{vs} is the mass fraction of virgin solid material, A is a pre-exponential factor and E is the activation energy. The formation rate of char and the formation rate of volatiles from the condensed phase are:

$$\dot{\omega}_{d}''' = \rho_s Y_{vs} A \exp(-E / RT_s) \tag{4-a}$$

$$\dot{\omega}_{sc}''' = SF\,\dot{\omega}_{d}''' \tag{4-b}$$

$$\dot{\omega}_{sg}''' = (1 - SF)\,\dot{\omega}_{d}''' \tag{4-c}$$

$$SF = 1 - (1 - \rho_c \rho_{vs}^{-1})\,\chi \tag{4-d}$$

Note ρ_{vs}, ρ_c designate the mass density of the virgin solid material and char, and χ is a user defined parameter that controls shrinkage and swelling.

The fuel mass loss rate (per unit exposed surface area) is by definition the mass flux of volatiles from the exposed surface of the solid material and may be expressed as:

$$\dot{m}_f''(t) = \int_0^L \dot{\omega}_{sg}'''(y,t)\,dy \tag{5}$$

where L is the sample thickness. Note that Eq. (5) neglects any possible gas transport effect from the depth of the solid sample to the exposed surface.

The solid material is treated as optically opaque. The heat flux at the exposed surface of the solid material (at y= 0) is:

$$\dot{q}_w''(t) = \underbrace{\varepsilon G - \varepsilon\sigma({T_{s,w}}^4 - {T_\infty}^4)}_{\text{radiation}} - \underbrace{h(T_{s,w} - T_\infty)}_{\text{convection}} \tag{6}$$

Note ε is the surface emissivity, G is the irradiation from the radiant panel, σ is the Stefan-Boltzmann constant, $T_{s,w}$ is the solid surface temperature (at $y = 0$), T_∞ is the ambient gas temperature, and h is the convective heat transfer coefficient. The model allows for constant or fluctuating radiant exposures. The back surface (at $y = L$) was assumed to be adiabatic.

Equations (1)–(3) are coupled partial differential equations. These equations were numerically solved using a fully implicit algorithm (second-order technique for spatial discretization time integration). The model calculation was validated by comparison with an analytical solution for a semi-infinite solid exposed to a constant

heat flux and provides an exact match. The performance of the model was further validated with Thermakin [21–22] in predictions of fuel mass loss rate for PMMA, high-impact polystyrene (HIPS), and PVC.

3.3.2 Determination of pyrolysis model parameters

The flammable materials examined in the present study are polymethyl methacrylate (PMMA) and polyvinyl chloride (PVC). The pyrolysis model necessitated a large number of unknown coefficients (material properties and parameters of the chemical reactions), which are needed to be determined for each material. To achieve this, the pyrolysis model was coupled to an automated optimization scheme which uses a genetic algorithm (GA). This optimization scheme adjusts the material properties in an iterative process based on evolutionary principles to obtain optimal agreement between the model and experimental data, typically coming from thermo-gravimetric and/or cone calorimeter experiments. Test data needed for non-charring and charring polymers were obtained from Ref. [21-22]. Table 3.1 presents value of material properties and reaction parameters for non-charring and charring material. The value of parameter $\chi = 1$ was considered for both PMMA and PVC.

Virgin Material Properties		
	PMMA	PVC
$\rho(kg/m^3)$	1109.80	1729.75
c(J/kg/K)	1311.30	1111.30
k(W/m/K)	0.27	0.17
ε	0.92	0.90
χ	1	1

Residue Material Properties		
	PMMA	PVC
$\rho(kg/m^3)$	-	397.84
c(J/kg/K)	-	3894.30
k(W/m/K)	-	0.10
ε	-	0.90
η		0.23

Reaction Parameters		
	PMMA	PVC
$\Delta H_p(kJ/kg)$	910	291.8
$A(s^{-1})$	1.29E+11	2.98E+13
E(kJ/mol)	153	193
$T_{thr}(^oC)$	-	230.09

Table 3-1. Synthetic data for non-charring and charring materials.

3.3.3 Mathematical theory

3.3.3.1 Amplitude of temperature fluctuation

The case of a one dimensional semi-infinite solid slab made of a homogenous material with constant properties was considered. The slab was assumed to be at a constant initial temperature, T_∞, and the surface was subjected to an oscillatory heat flux. In this section, the mathematical models used to predict the thermal behavior of the slab will be developed. A heat balance over the body leads to the following well-known transient heat equation:

$$\frac{\partial T}{\partial t} = \alpha \frac{\partial^2 T}{\partial y^2} \tag{7}$$

where α is the thermal diffusivity. The boundary condition at the surface is $q(0,t) = q_A \sin(\omega t)$. The classical solution found in the literature [41] may be expressed in the form of:

$$T(y,t) = T_\infty + A\sin(\omega t - y\phi) - \frac{2q_A}{k\sqrt{\pi}} \int_0^{y/2\sqrt{\alpha t}} \cos(\omega(t - \frac{y^2}{4\alpha\xi^2} - \frac{\pi}{4})) \exp(-\xi^2) d\xi \tag{8-a}$$

$$A = \frac{q_A}{k}\sqrt{\frac{\alpha}{w}} e^{-y\sqrt{\frac{\omega}{2\alpha}}} \tag{8-b}$$

$$\phi = (-\sqrt{\frac{\omega}{2\alpha}} - \frac{\pi}{4}) \tag{8-c}$$

It can be seen in the steady state solution that A represents the amplitude of oscillation at point *y* inside the material, and ϕ in the sinusoidal function represents the phase lag of oscillation at the point *y* relative to the oscillation of the surface temperature. The oscillation at *y* (deeper inside the slab) is not as strong as at the surface and there is a delay from the time that the surface temperature changes to the time that the temperature at *y* responds to such change. The amplitude of temperate oscillation at the front surface may be written as:

$$A_{\Delta T} = \frac{q_A}{k}\sqrt{\frac{\alpha}{\omega}} \tag{9}$$

The sudden surface temperature change gradually propagates into the semi-infinite slab. The heat is conducted inside the material, developing two different sections: the heated region where the temperature is affected by the surface-imposed heat, and the virgin region, where the material has not felt the presence of the surface heating and remains at the initial temperature. The distance between the surface of the material and the start of the virgin region is called the heat penetration depth, $\delta_t = 4\sqrt{\alpha t}$. The wavelength of the heat equation analytical solution**,** the distance over which the waves shape repeats, is given by $\lambda = \frac{2\pi}{k'} = 2\pi\sqrt{\frac{2\alpha}{\omega}}$. Equation 8(b) provides the temperature profile inside a slab with a finite volume.

3.3.3.2 Amplitude of mass loss rate fluctuation.

In this section, a simplified method to account for the effect of fluctuation in radiant heat panel on mass loss rate was applied. The reaction rate, Eq. 4(a), is decomposed to an averaged and a fluctuation component, $\omega = \overline{\omega} + \widetilde{\omega}$. Note that the reaction rate is depend of the temperature, thus the temperature field is decomposed in the same manner. The reaction form may be expressed as

$$\omega = \rho_s Y_{vs} A \exp(-E / RT_s) = \rho_s Y_{vs} A \exp(-\frac{E}{R(\overline{T} + \widetilde{T})}) \qquad \text{(10-a)}$$

The reaction rate can be further be represented by a Taylor series:

$$\omega = \omega(\overline{T}) + \widetilde{T}\frac{\partial \omega}{\partial T}\bigg|_{\overline{T}} + \frac{\widetilde{T}}{2}\widetilde{T}\frac{\partial^2 \omega}{\partial T^2}\bigg|_{\overline{T}} + O(3) \qquad \text{(10-b)}$$

The mean value of the reaction rate and the oscillatory component were obtained using Eq. 10(b) and expansion of an exponential function. Thus the ratio of the oscillatory component to the averaged reaction rate becomes:

$$\frac{\widetilde{\omega}}{\overline{\omega}} = 2\sinh(\frac{E}{R\overline{T}}\widetilde{T}) \qquad \text{(10-c)}$$

The oscillation in mass loss rate is the integration of the change in reaction rate, Eq.10 (c) over the pyrolysis zone. The reaction zone for non-charring material, in this study, remains close to the surface, i.e. within the characteristic length scale, provided

above. In addition, the average temperature can be estimated for PMMA based on the net value of heat flux on the sample surface.

3.4 Results and discussion

The previous section has described the development of a pyrolysis model to simulate the degradation of PMMA and PVC. The pyrolysis model allows for constant or time-varying radiant exposures. Using a Fourier transform, the turbulent functions may be decomposed into a summation of sinusoidal and cosinesoidal functions of different frequencies. Thus, sinusoidal variations in irradiation were used in the form $G = G_{mean} + G_A \sin(2\pi f t)$ where G_{mean}, G_A, f are the mean irradiation from panel, the forcing irradiation amplitude, and the forcing frequency, respectively.

These variations in gas-to-solid heat loading induce oscillations in the solid temperatures. The following parameters were varied to provide a qualitative analysis of the effect of harmonic thermal load on the pyrolysis of charring and non-charring sample: Mean intensity varied between G = 25 kW/m^{2}and G = 100 kW/m^2; amplitude of forcing irradiation varied between G = 5 kW/m^2 and G = 20 kW/m^2; and forcing frequency varied from 0.1 Hz to 10 Hz. We assume here that the sample thickness is L = 5 mm and the convective heat loss at the surface of the samples is negligible. The initial temperature is 300 K and the temporal and special resolutions are 100 μm and 100 ms (a smaller time increment was used for the case of harmonic thermal load with high frequency). The numerical results are compared in terms of the following features: transient burning rate and front surface temperature behavior; the burn out time; and the average MLR values. The temperature field, heat flux and MLR are decomposed in the form of $\varphi(y,t) = \overline{\varphi}(y,t) + \tilde{\varphi}(y,t)$ where φ is the field variable, $\overline{\varphi}$ is the mean and $\tilde{\varphi}(y,t)$ is special and temporal oscillation. This will allow finding the averaged value of temperature, radiant heat flux and MLR, their oscillatory trend and other characteristic. The amplitude of fuel mass loss rate and front surface temperature are further analyzed. The intent of this study is to determine

whether, and by how much, the burning rate of solid fuel predictions under harmonic thermal load departs from the regression rate measured in quasi-steady conditions.

3.4.1 Non-charring polymer (PMMA)

Figure 3.1 shows the time histories of fuel mass loss rate and the surface temperature for a PMMA sample obtained with a steady radiant heat flux varying between G = 25 kW/m^2 and G = 100 kW/m^2 . As indicated in figure 3.1(a), the magnitude of incident heat flux has a large effect on the burning behavior of PMMA sample. A simple analytical approximation of regression rate and burnout time may be written as:

$$\dot{m}'' = \frac{\dot{q}''_{wall}}{\Delta H_p}, \qquad t_{burn} = \frac{\rho L \Delta H_p}{\dot{q}''_{wall}} \tag{11}$$

where $\dot{q}''_{wall}$ is the net thermal load , ΔH_p the heat of pyrolysis, ρ the density, and L the sample thickness. The MLR is proportional to the magnitude of net thermal load, and therefore the level of incident radiation, whereas the burning time is inversely proportional to incident heat flux. The higher the incident heat flux, the higher the peak value of mass loss rate and a shorter burning time, as illustrated in figure 3.1. Assuming the appropriate surface temperature, the steady burning rate using Eq. 11 is (23, 48, 72, and 96) g/s^{-1}m^2 for radiant heat flux of (25, 50, 75, 100) kW/m^2 which gives about 20% error compared to steady regression rate observed in figure 3.1(a). In addition, at the lower heat flux, the sample shows the thermally thin behavior whereas at higher level of radiant heat flux it exhibits a thermally thick behavior. The higher value of the incoming heat flux results in a higher front surface temperature, as shown in figure 3.1(b). After the growth phase, the surface temperature of the PMMA sample shows a benign increase. The peak in surface temperature at the end of burning is due to the reduction of conductive heat flux in the shrinking sample as the pyrolysis wave front reaches the back wall.

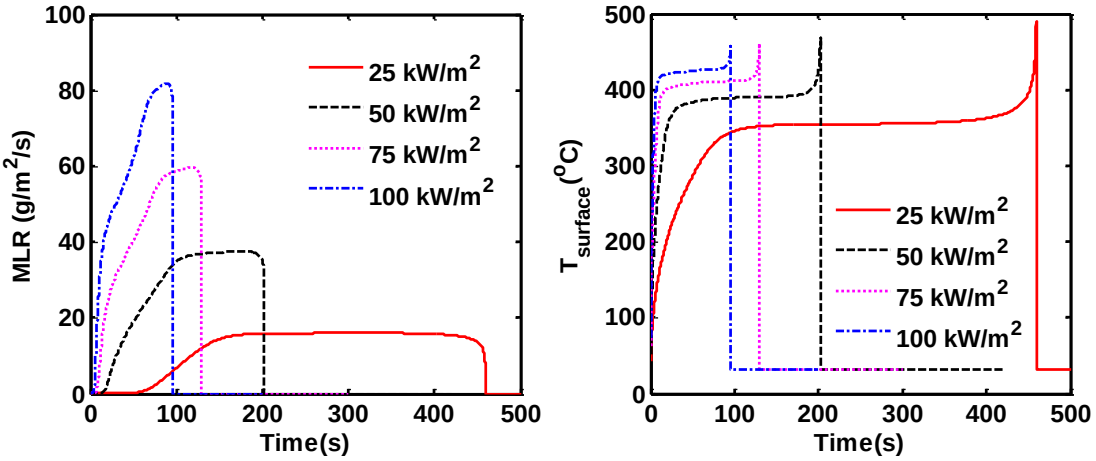

Figure 3-1. Time variation of the fuel mass loss rate (left) and front surface temperature (right): Case of a 5mm PMMA sample subjected to a constant radiant heat flux.

Figure 3.2 shows a comparison between the simulated MLR obtained with a steady and harmonic radiant heat flux for a PMMA sample. The PMMA sample was subjected to incident radiation values of $G_{mean} = 50\,\mathrm{kW/m^2}, G_A = 10\,\mathrm{kW/m^2}\ f = 0.1Hz$. The figure shows the burning rate of the fuel is sensitive to the excitation of the radiant heat flux. The harmonic behavior in the MLR curve is observed and remains until the burn out time. This means the regression rate has a strong dependence on the incoming heat flux in a timely manner and departs from the semi-steady condition observed in cone calorimeter tests. However, the averaged mass loss rate and the burnout time are not affected with the radiant heat flux fluctuation. Furthermore, the variation in MLR is consistent with figure 3.1(a) and that of predicted with Eq.10(c), which will be discussed in more detail. The sensitivity of the overall MLR trend may result in extinction or faster flame spread in a real fire scenario where the released volatiles mix with oxygen. It is worth noting that time scale for solid phase combustion is about two orders of magnitude greater than for gas phase combustion—meaning it takes more time for the solid fuel to get adjusted to changes in the incoming heat flux.

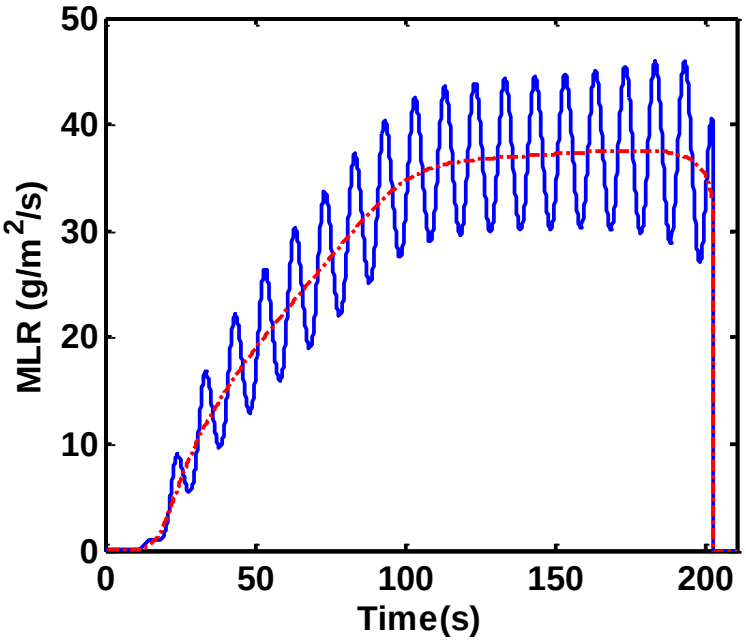

Figure 3-2. Time variation of the fuel mass loss rate:Case of 5mm PMMA sample subjected to a constant (red dots) and time-varying (blue line) radiant heat flux.

Figure 3.3 shows the time histories of front surface and back wall temperatures of the PMMA sample under steady and unsteady radiant exposure. Under constant radiative heat flux, the surface temperature reaches a nearly steady value after the growth phase. The net heat flux is nearly constant, see Fig. 3.4, and a significant amount of energy is available for the pyrolysis reaction to take place. In the case of sinusoidal radiant heat flux, the excitation in the thermal load results in the harmonic behavior observed in front surface temperature, shown in Fig 3.3. The back wall temperature, was affected by the exited thermal load after 3.2 minutes when the pyrolysis zone approaches the back as a result of sample shrinkage.

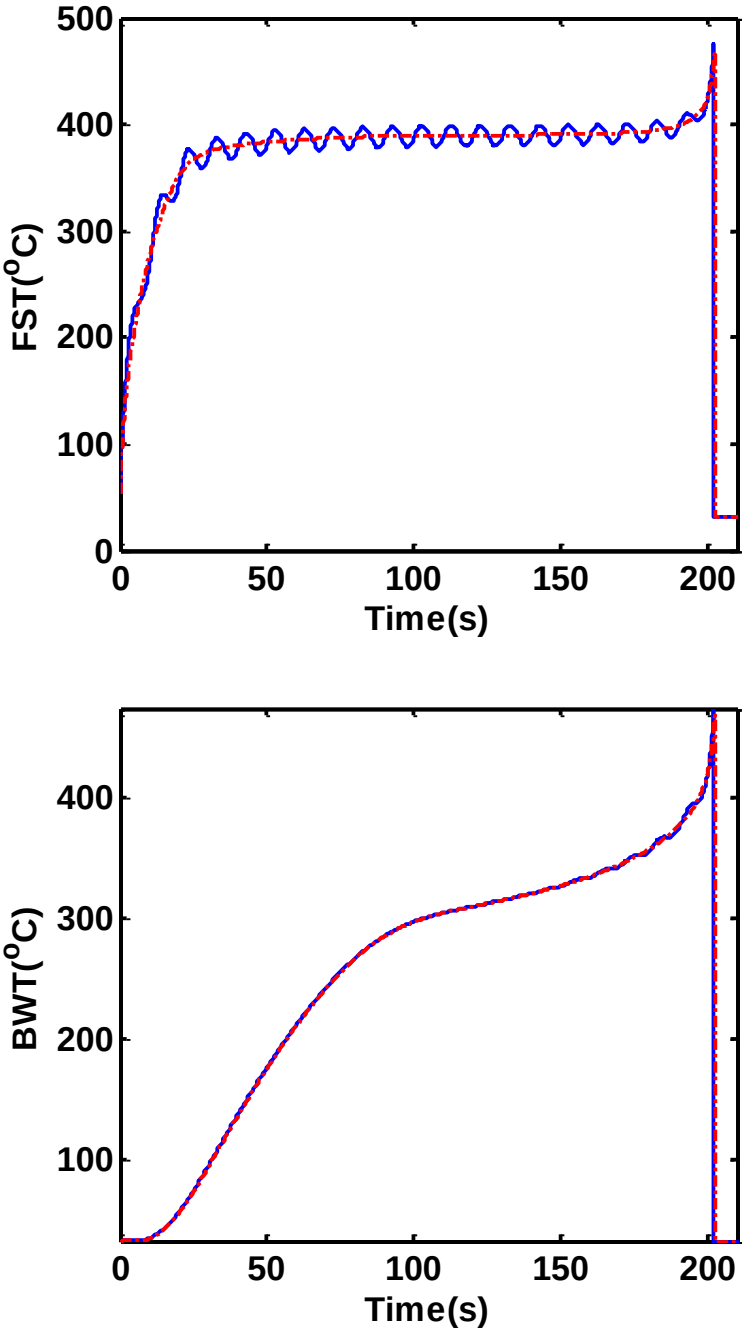

Figure 3-3. Time variation of the front surface temperature (top) and back surface temperature (bottom): case of 5mm PMMA sample subjected to a constant (red dots) and time-varying (blue line) radiant heat flux.

The temperature and reaction rate profile at 81 seconds for one cycle inside the PMMA solid sample exposed to harmonic heat flux are shown in Fig. 3.5. As it is

illustrated in the figure, fluctuations appeared in the traces of temperature profile and reaction rate. The characteristic length scale, $l = \sqrt{2\alpha/\omega}$, has the value of 0.768 mm. The pyrolysis front is within the characteristic distance of the exposed surface in which the incoming heat flux is excited, and therefore the effects of time-varying irradiation are pronounced. The reaction zone remains close to the surface of PMMA sample as opposed to charring material which will be discussed later.

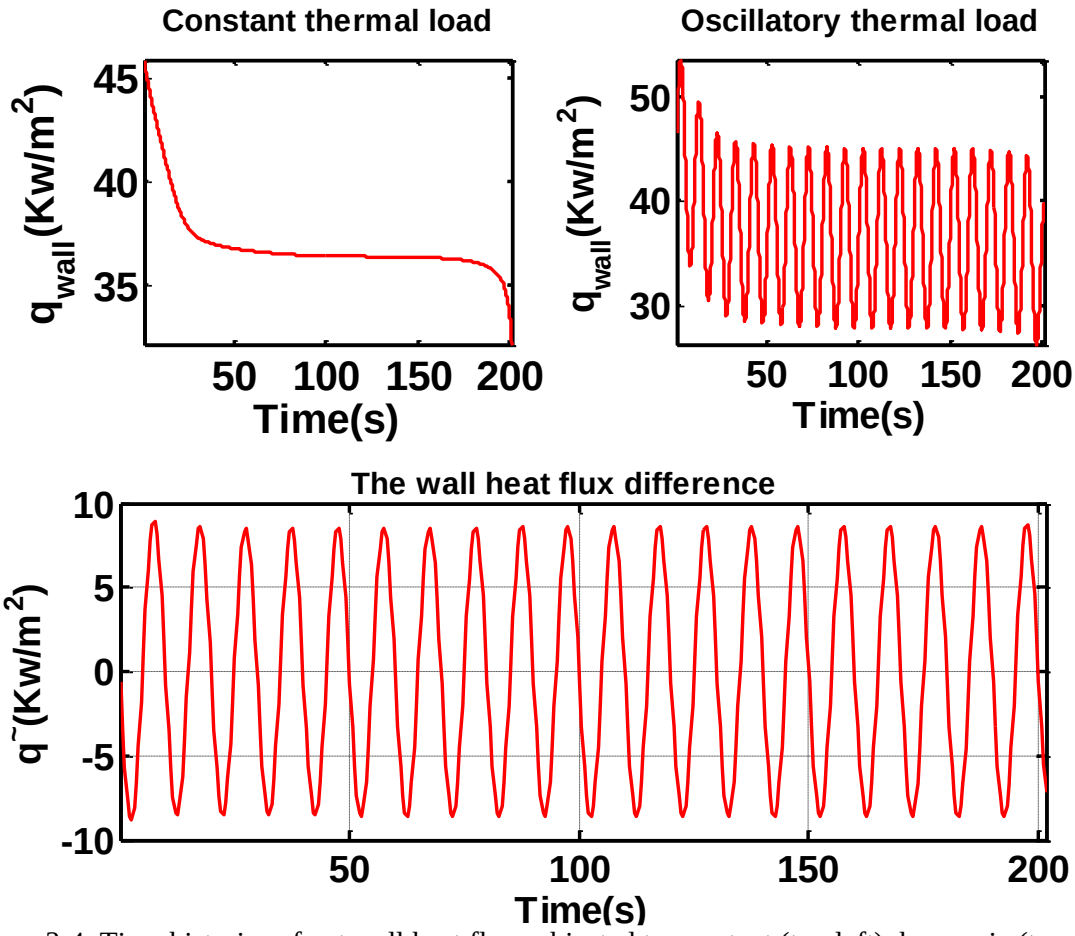

Figure 3-4. Time histories of net wall heat flux subjected to constant (top left), harmonic (top right), and their difference (bottom): case of 5 mm PMMA sample with $G_{mean} = 50\text{Kw/m}^2$, $G_A = 10\text{Kw/m}^2$, $f = 0.1\,\text{HZ}$.

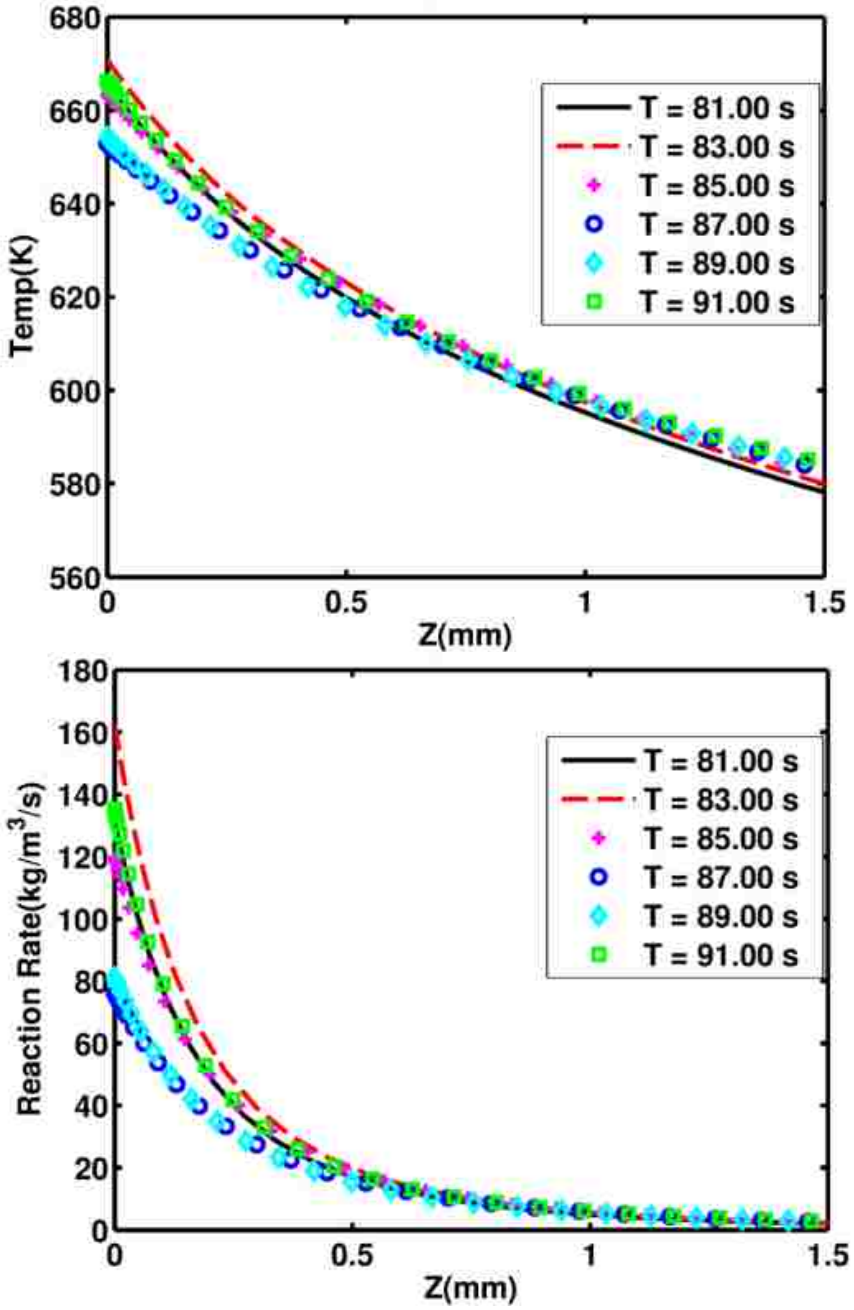

Figure 3-5. Temperature and reaction rate distribution inside solid sample subjected to harmonic radiation $G_{mean} = 50\,\mathrm{kW/m^2}, G_A = 10\,\mathrm{kW/m^2}\ f = 0.1Hz$: Case of 5 mm PMMA sample.

The temporal temperature oscillation is obtained from $\tilde{T} = T - \bar{T}$ where the average temperature field, $\bar{T}$, is obtained under a constant radiant heat flux G_{mean} and

T is the temperature field under an oscillatory radiant heat flux in the form of $G = G_{mean} + G_A \sin(2\pi f t)$. The main drawback of this linearized formulation is that it is implicitly assumed that the temperature fluctuation comes from the oscillatory part of radiant heat flux which is not fully correct at higher values of heat flux.

The amplitude of the surface temperature as a function of time at four levels of mean radiation heat flux while keeping the oscillation amplitude and frequency fixed at 10 kW/m^2 and 0.1 Hz, respectively, is shown in figure 3.6. The attenuation of the magnitude of temperature oscillation, i.e. the reduction in the amplitude, is observed in figure 3.6 during the growth phase. The amplitude of oscillation shows a steady behavior after the growth phase at low and intermediate level of mean radiant heat flux ($G \leq 50\ kW/m^2$). At higher level of heat flux, i.e., $G \geq 75\ kW/m^2$, a quasi-steady behavior for surface fluctuating magnitude is observed. In addition, the amplitude of fluctuation of surface temperature is higher at lower values of mean irradiation.

Figure 3.7 presents the amplitude of surface temperature for the mean radiative heat flux of $G_{mean} = 50 \text{kW/m}^2$ and an oscillation amplitude of $G_A = 10 \text{kW/m}^2$ as a function of time. The amplitude of surface oscillation is calculated after the growth phase. The overall surface temperature magnitude trend is similar with the corresponding value calculated from Eq. 9; more precisely, an increase in frequency results in a decrease in the amplitude of surface temperature while an increase in oscillation amplitude has the opposite effect. Notice that the high frequency excitation would give rise to a small penetration depth of the oscillations.

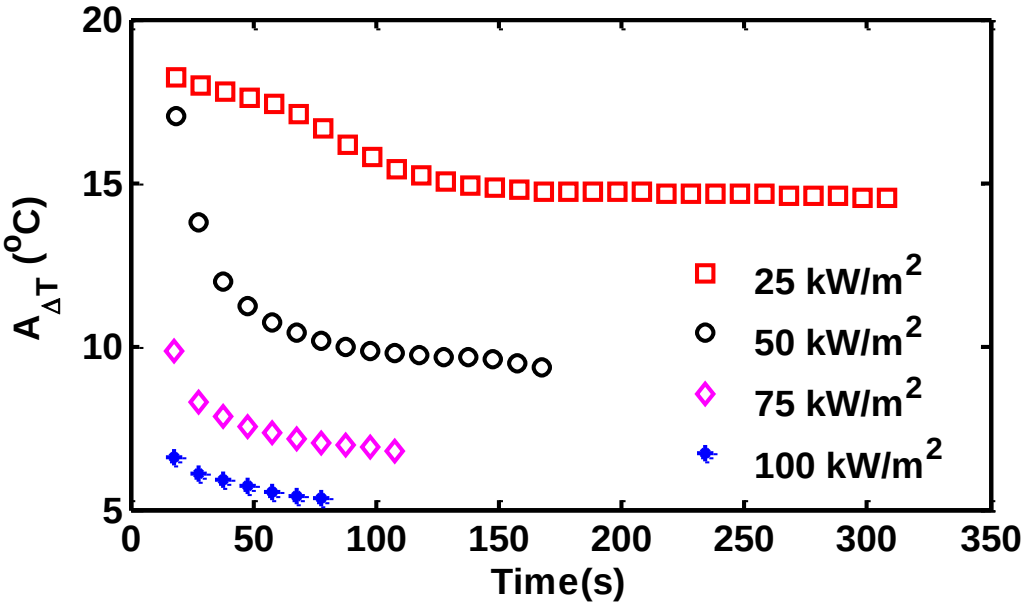

Figure 3-6. Time histories of the amplitude of surface temperature subjected to $G_A = 10\text{kW/m}^2$, $f = 0.1\,\text{Hz}$: Case of 5 mm PMMA sample.

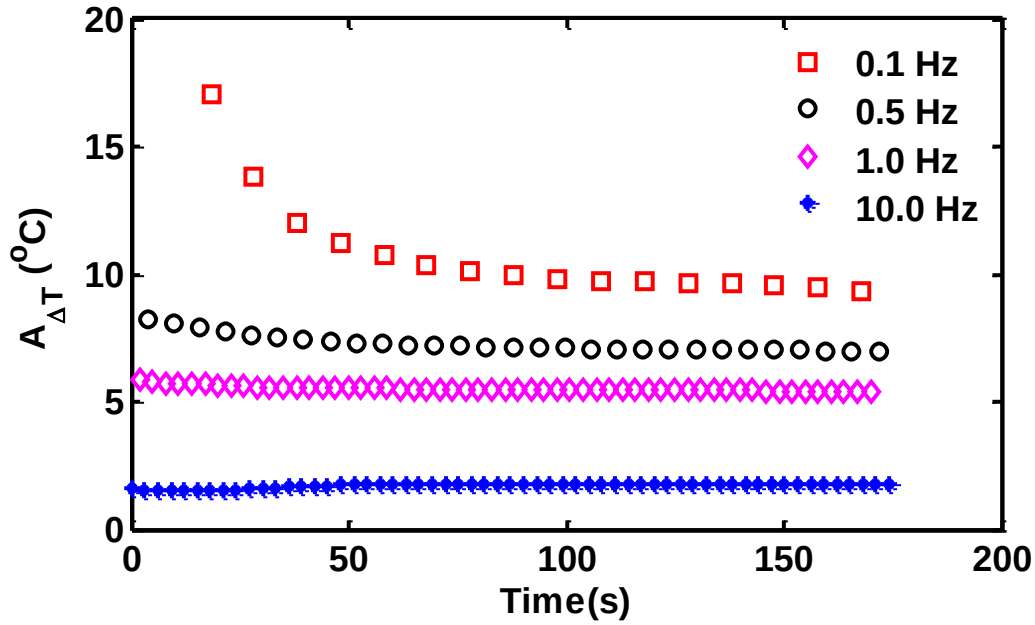

Figure 3-7. Time histories of the amplitude of surface temperature subjected to $G_{mean} = 50\text{kW/m}^2, G_A = 10\text{kw/m}^2$: Case of 5 mm PMMA sample.

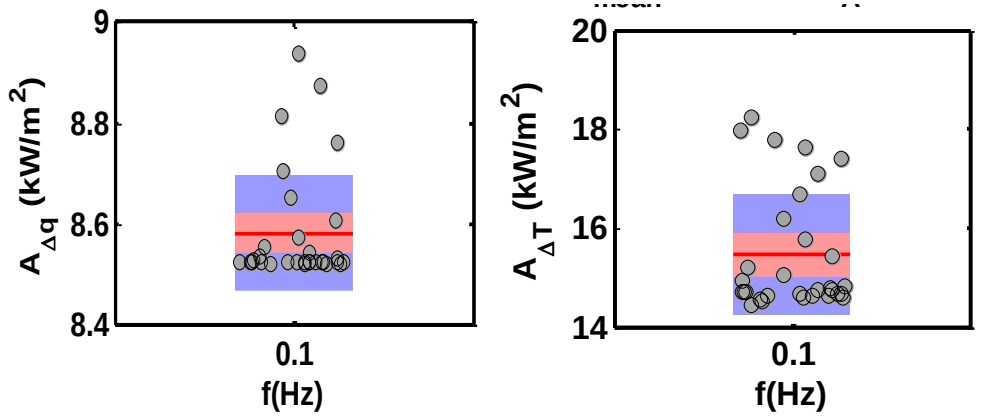

Figure 3-8. Schematic for calculating mean value of temporal heat flux amplitude (left) and surface temperature amplitude (right) for $G_{mean} = 25\text{kW/m}^2, G_A = 10\text{kW/m}^2$: Raw data: gray points, average value: red line, 95% confidence: blue box.

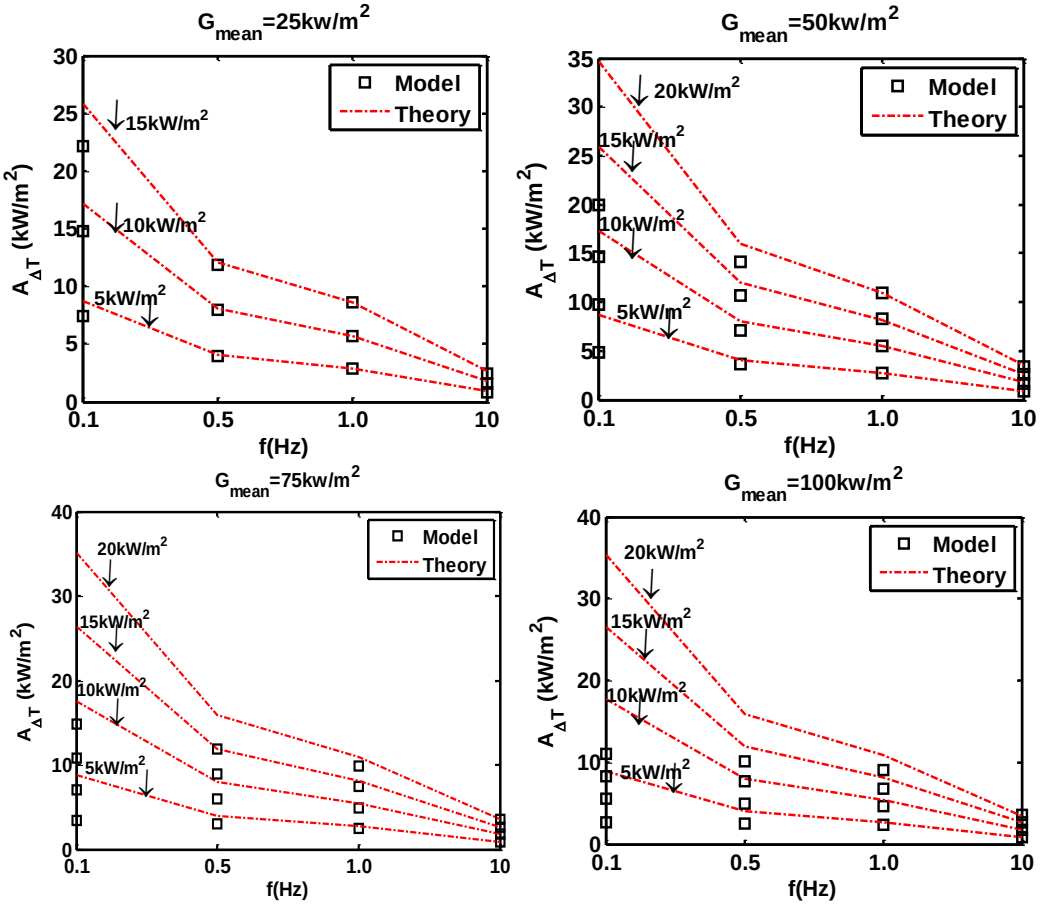

Figure 3-9. The amplitude of surface temperature: Case of 5 mm PMMA sample, theoretical (dashed line), model (square).

In order to compare the model prediction with theoretical value obtained from Eq. (9), the averaged value of surface and temporal heat flux for each value of mean irradiation, forcing irradiation amplitude, and forcing frequency is obtained using the methodology shown in figure 3.8. The outliers, i.e. the points during the growth phase are first identified and removed, and then the average value of surface and temporal heat flux amplitude is calculated.

The representative results in the form of a comparison between the simulated amplitude of surface temperature and theoretical prediction are shown in figure 3.9 and table A1-A4. The mean intensity takes values between G = 25 kW/m^2 and G = 100 kW/m^2, the amplitude of forcing irradiation takes value between G = 5 kW/m^2 and G = 20 kW/m^2, and the forcing frequency is changed from 0.1 Hz to 10 Hz. As it is illustrated in the tables, there is a significant discrepancy at: (1) low value of forcing frequency f $\leq$ 0.5 Hz where the normalized error between model prediction and theory varies between 18% (low value of mean heat flux) to 200% (high level of mean heat flux); and (2) high values of heat flux $G_{mean} \geq 100$ Kw/m^2 where the error between model and theory is about 24%.

The theoretical value of amplitude of temperature oscillation at the front surface is obtained from the steady state analytical solution of the heat-diffusion equation for a semi-infinite solid slab exposed to oscillatory heat flux at the front surface. It is worth noting that:

1. The surface heat flux during the pyrolysis process decays in time due to re-radiation. However, the analytical solution of semi-infinite slab is obtained where the surface is exposed to a fixed harmonic heat flux, meaning the value of heat flux at the surface does not decay in time. In order to correct the effect of surface re-radiation, the temporal heat flux, $\tilde{q}$, needed to calculate the theoretical value of surface oscillation is obtained from the pyrolysis model. More precisely, the net heat flux is decomposed in the form of $\tilde{q} = q - \bar{q}$ where the average net thermal load, $\bar{q}$, is the net mean radiative heat flux and q is the net oscillatory radiant heat. Note that the main drawback of this

linearized formation is that it is implicitly assumed that the field variable fluctuation comes from the oscillatory part of radiant heat flux which is not fully valid at higher values of heat flux.

2. The analytical solution is valid for a thermally thick sample. At higher values of radiant heat flux and thus faster heating, the thermally thick assumption is not valid for a shrinking PMMA sample.
3. The analytical solution does not account for a reaction mechanism.
4. To obtain the magnitude of surface oscillation, the transient part of the analytical solution is neglected. At faster time periods, the transient part becomes important and may not be ignored.

A sensitivity analysis was carried out in an attempt to understand the relative importance of the heat of pyrolysis and sample thickness on the overall trend amplitude of front surface temperature under an oscillatory radiant heat flux.

Case 1: Low value of forcing frequency and mean radiant heat flux: effect of heat of pyrolysis

As illustrated in figure 3.9, the theory over-predicts the simulated amplitude of surface temperature; the error between the model prediction and theory at low radiative heat fluxes of $G_{mean} = 25\text{kW/m}^2$ and $G_{mean} = 50\text{kW/m}^2$ is 18% and 80%, respectively, while keeping the forcing frequency at 0.1 Hz (see table A1-2). At higher values of mean radiative heat flux, the error is larger while the effect of amplitude of forcing heat flux is negligible. The reaction mechanism is neglected in the theoretical expression, meaning that the heat of pyrolysis can be the under-lying cause of the discrepancy between model and theory. To further illustrate the effect of heat of pyrolysis on the amplitude of surface temperature, the heat of pyrolysis was varied between h_p = 0 kJ/kg and h_p = 9 MJ/kg. It was observed that increasing the heat of pyrolysis to 9 MJ/kg led to an even larger discrepancy, shown in table A.5 in the appendix.

Figure 3.10 shows time histories of amplitude of temporal net heat flux and surface temperature at four level of mean radiation panel while the forcing irradiation

amplitude, frequency and heat of pyrolysis is $G_A = 5\text{kW/m}^2$, $f = 0.1\text{Hz}$ and h_p = 0 kJ/kg, respectively. As it is illustrated in the figure, there is a good agreement between the model and theory at low value of forcing frequency. For a series of forcing amplitudes varying between G_A = 10 kW/m^2 and G_A = 25 kW/m^2 similar trend were observed; the error becomes negligible at low values of heat of pyrolysis.

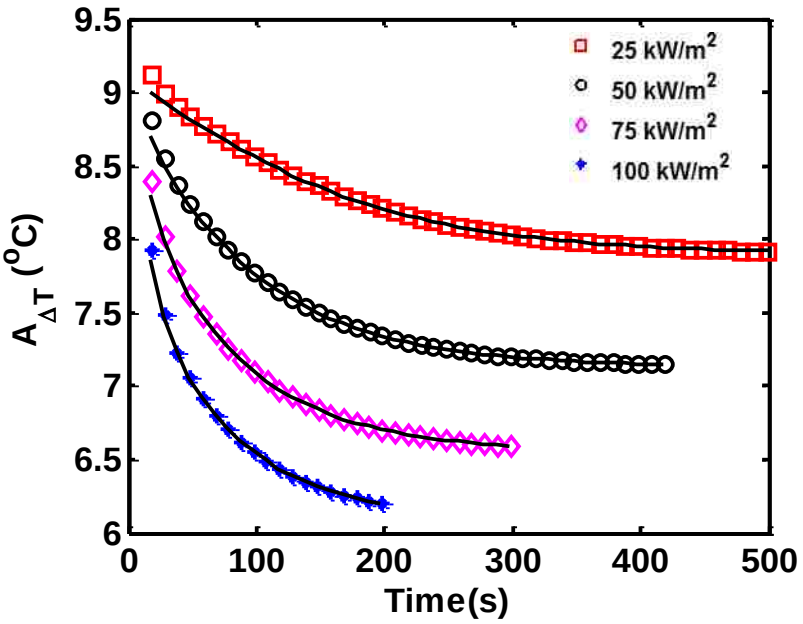

Figure 3-10. Time histories of the amplitude of fluctuating front surface subjected to $G_A = 5\text{kW/m}^2$, $f = 0.1\text{HZ}$ at four level of mean radiation: Case of 5 mm PMMA sample with h_p = 0 kJ/kg. The solid black line represents the amplitude predicted by theory.

Case 2: High value of mean heat flux: effect of heat of pyrolysis and sample thickness

An increase in the mean radiative heat flux, i.e., $G \geq 75\ kW/m^2$ results in a larger discrepancy between the model and the theoretical expression, as shown in figure 3.9. In order to identify the source of discrepancy, the heat of pyrolysis was changed to 0.9 kJ/kg and the sample thickness is set to L=50 mm. The representative results in the form of comparison between the amplitude of surface temperature predicted by model and the theoretical value for $G_{mean} = 75$ and $100 kW/\text{m}^2$ are shown in figure 3.11. The error between model and theory is significantly reduced for both level of heat

flux. The error is reduced from 160% to 32% at mean radiative heat flux of $G_{mean} = 75\ \text{kW/m}^2$ and at $G_{mean} = 100\text{kW/m}^2$, it decreases from 215% to 37%.

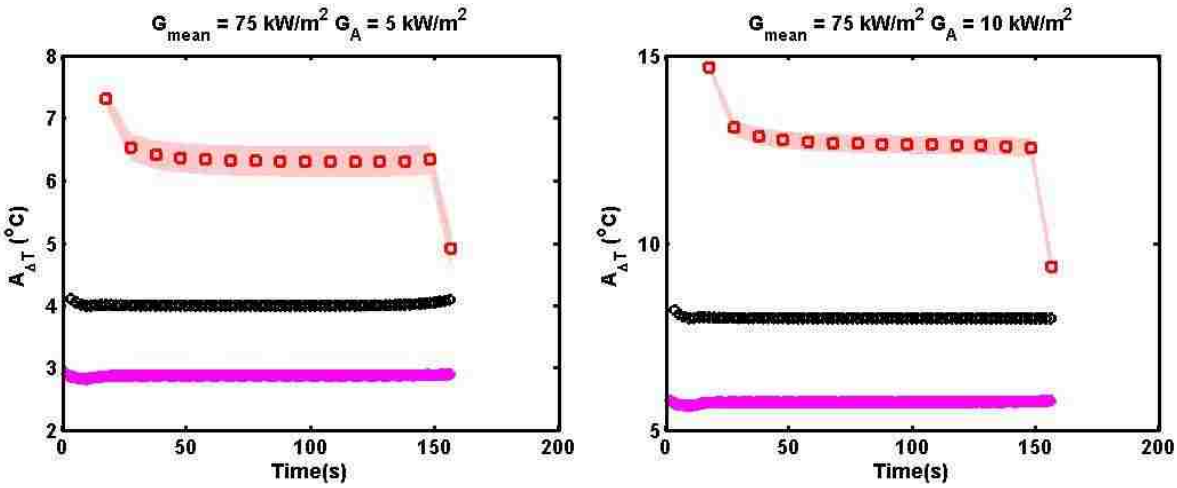

Figure 3-11. Time histories of the amplitude of surface temperature subjected to $G_{mean} = 75\text{kW/m}^2$: Case of 50 mm PMMA sample with h_p = 0.9 kJ/kg. The shaded area in $A_{\Delta T}$ shows the error between theory and model predictions.

Figure 3.12 shows the amplitude of MLR for an oscillation amplitude of $G_A = 10\ \text{kW/m}^2$, frequency of 0.1 and the mean external radiation varying between 25 *kW/m²* and 100 *kW/m²* as a function of time. The higher value of mean irradiation corresponds to a faster initial heating of the PMMA sample, thus providing a significant amount of heat for the pyrolysis process. Consequently, the higher reaction rate leads to more release of gaseous flammable vapor. The magnitude of oscillatory MLR shows a quasi-steady trend after the growth phase. The effects of time-varying radiant exposure are pronounced during the entire pyrolysis process, from ignition to burn-out. In addition, the burning time is longer at lower values of heat flux. Note that the burning time is inversely proportional to radiative heat flux.

Figure 3.13 shows the time histories of amplitude of reaction rate at the surface of PMMA slab subjected to four levels of forcing frequencies while keeping the mean radiative heat flux and forcing irradiation amplitude fixed at $G_{mean} = 50\text{kW/m}^2$, $G_A = 10\text{kW/m}^2$. The shaded areas in the figure show the error between the model and the theoretical value obtained from Eq. 10(c). There is good

agreement between the model and theory at high values of forcing frequency. The significant error at low values of forcing frequency, i.e. f = 0.1 Hz, arise from the overestimation of surface temperature in the analysis of the surface temperature fluctuation, as discussed earlier.

Figure 3.14 presents the amplitude of MLR for the mean radiative heat flux of $G_{mean} = 50\text{kW/m}^2$ and an oscillation amplitude of $G_A = 10\text{kW/m}^2$ as a function of time with for value of forcing frequencies. An increase in frequency decreases the magnitude of the amplitude, which is consistent with the results observed in figure 3.7. The higher value of temperature fluctuations as a result of increased frequency results in a lower reaction rate time scale. More precisely, the time scale associated with oscillatory radiant incoming flux is within the same order of magnitude of the reaction time scale, leading to a smaller release of volatiles. In addition, at similar values of frequency, the amplitude of MLR increases with higher oscillation amplitude of forcing radiant heat flux. Within a cycle, higher forcing irradiation amplitude provides a higher maximum and a lower minimum value of thermal load. That is, at the time during which the radiant heat flux attains the maxima, the extra heat result in a rapid release of flammable vapor. On the other hand, at the time when it reaches the minima, the value of fuel release is lower, leading to a higher amplitude of mass loss rate.

The theoretical oscillation in mass loss rate is calculated by integration of the amplitude of reaction rate, over the pyrolysis zone. The reaction zone for PMMA sample is confined within a small region, shown in figure 3.5. At higher values of forcing frequency, the normalized error between the amplitude of MLR oscillation predicted by model and theoretical values varies between 4–8%. However, the error becomes significant at lower value of forcing frequency; the error is within 20% at forcing frequency of $f = 0.5\,\text{Hz}$ and 90% at $f = 0.1\,\text{Hz}$.

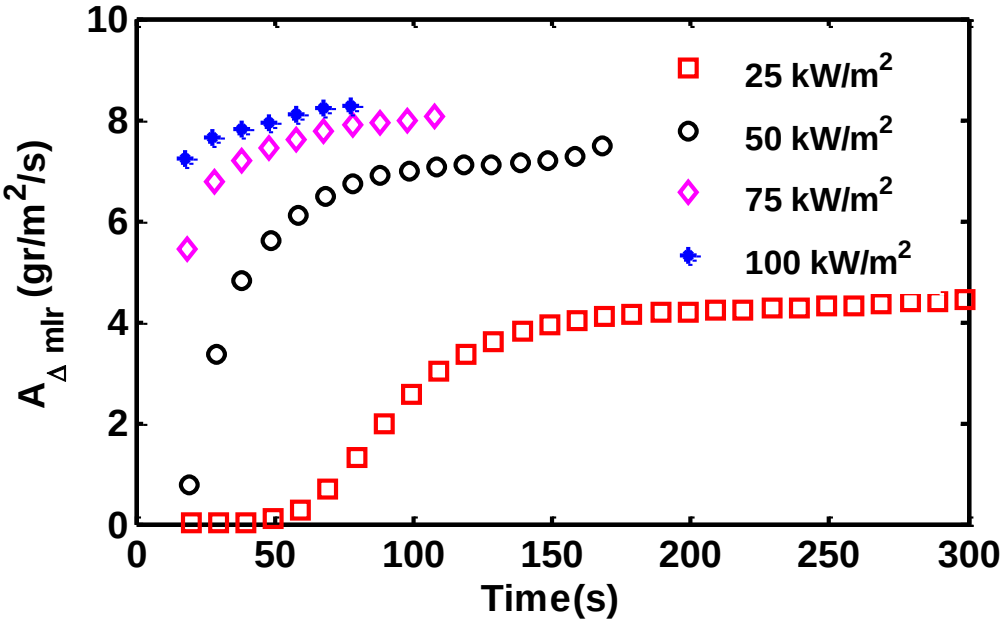

Figure 3-12. Time histories of amplitude of mass loss rate subjected to $G_A = 10\text{kW/m}^2$, $f = 0.1\,\text{Hz}$: Case of 5 mm PMMA.

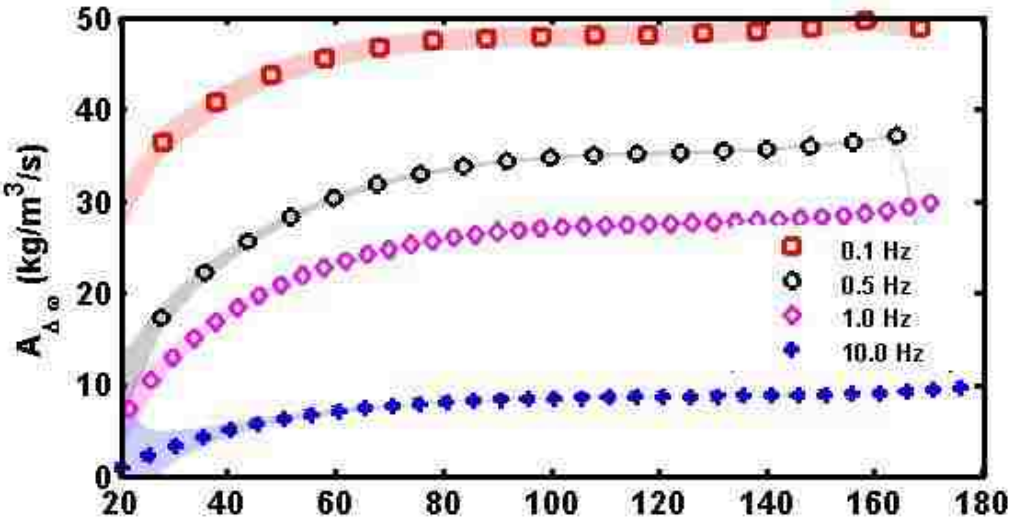

Figure 3-13. Time histories of the amplitude of reaction rate at the surface subjected to $G_{mean} = 50\text{kW/m}^2$, $G_A = 10\text{kW/m}^2$: Case of 5 mm PMMA.

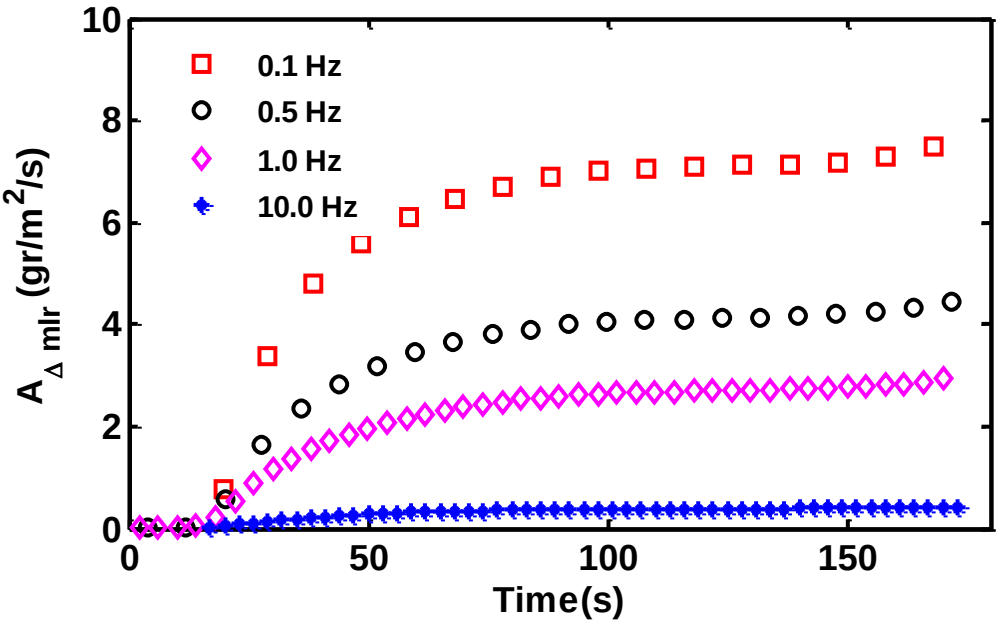

Figure 3-14. Time histories of the amplitude of oscillatory mass loss rate subjected to $G_{mean} = 50\text{kW/m}^2$, $G_A = 10\text{kW/m}^2$: Case of 5 mm PMMA.

The effect of activation energy on both mass loss rate and temperature field is significant. An increase in activation energy results in a lower reaction rate and thus a lower release of flammable vapor. The amplitude of surface temperature. Since the pyrolysis process is endothermic, increasing activation has an opposite effect, i.e. a lower temperature fluctuation and a higher fuel mass loss. There was a critical condition (increased activation energy by a factor of 2) at which the pyrolysis process takes heat from the back wall surface as a consequence of faster reaction processes. This results in a cooling effect on the back surface.

The higher the thermal inertial, the longer it takes for pyrolysis to begin. In addition, the amplitude of surface temperature becomes lower as the solid sample is more resistant to the radiant heat flux. On the other hand, lower thermal inertia (more thermally responsive) facilitates the onset of the pyrolysis process, resulting in a higher value of temperature fluctuation.

3.4.2 Charring polymer (PVC)

Figure 3.15 displays the time histories of fuel mass loss and the surface temperature for PVC sample obtained with a steady radiant heat flux varying between G = 25 kW/m^2 and G = 100 kW/m^2 . The MLR is proportional to the magnitude of radiant heat flux, whereas the burning time is inversely proportional to incident heat flux. The higher the incident heat flux, the higher the peak value of mass loss rate and a shorter burning time, as illustrated in figure 3.15 After achieving the first mass loss rate peak, the char layer forms an increasing thermal resistance, by heat absorption and enhanced surface irradiation, between the exposed surface and pyrolysis front. This results in a continuous decrease in mass loss rate. At low values of heat flux $G \leq 25kW/m^2$ less energy is fed to the pyrolysis front. As a result, the propagation of the pyrolysis wave is slower and the peak in the mass flux of pyrolysis gases is lower and postponed in time.

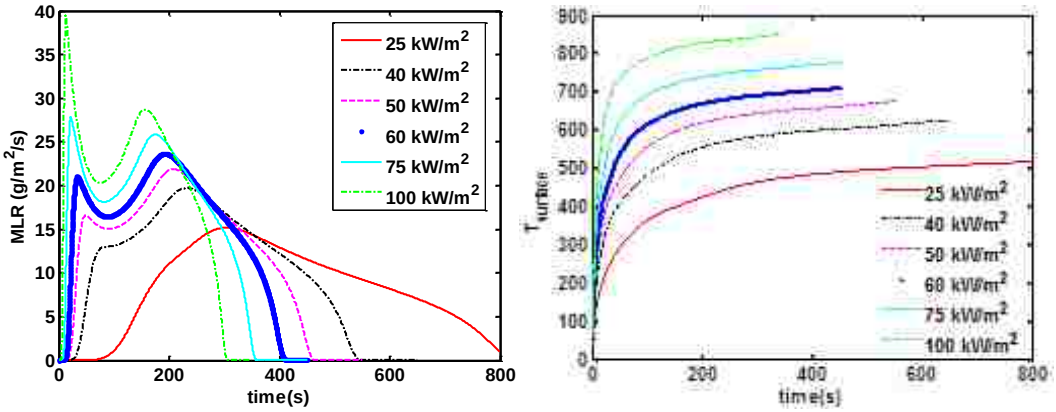

Figure 3-15. Time variation of the fuel mass loss rate (left) and front surface temperature (right): Case of 5 mm PVC sample subjected to a constant radiant heat flux.

Figure 3.16 presents representative results in the form of a comparison between the simulated fuel mass loss rate obtained with a steady and unsteady radiant heat flux The PVC sample was subjected to incident radiation values of $G_{mean} = 50 kW/m^2, G_A = 10 kW/m^2 f = 0.1Hz$. The harmonic variation in thermal load, shown in figure 3.16, induces oscillations in buring rate and front surface temperature. The oscillatory behavior in the burning rate of PVC is damped out

before MLR attains the second peak. This indicates the strong dependency of fuel mass loss rate on the incoming heat flux before the growth of the char layer. The growing char layer formed a high thermal resistant layer between the front surface and the pyrolysis front wave, acting like a damper and diminishing the thermal oscillatory wave propagating from the front surface toward the solid slab. However, the averaged mass loss rate and the burnout time are not affected with the radiant heat flux fluctuation. In addition, the trace of MLR minimums (maximums) as a function of time has a similar trend to that of constant radiant heat flux of $G_{mean} = 40\,\mathrm{kW/m^2}$ ($G_{mean} = 60\,\mathrm{kW/m^2}$), shown in Fig. 3.15. Note that the amplitude of regression rate varied with time before it reaches the second MLR peak, which will be discussed later.

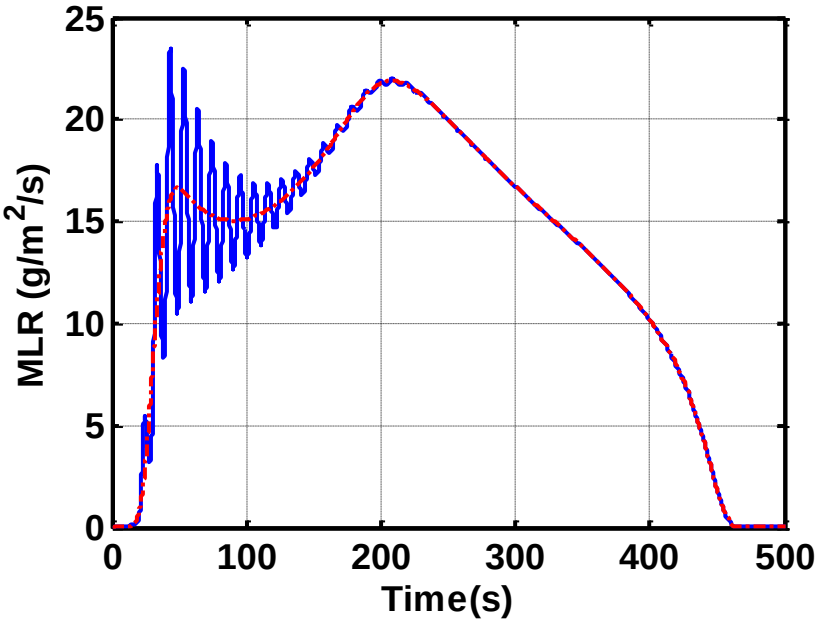

Figure 3-16. Time variation of the fuel mass loss rate:Case of a 5mm PVC sample subjected to a constant (blue line) and time-varying (red dots) radiant heat flux.

The time histories of surface temperature and back wall temperature of the PVC slab under steady and unsteady radiant heat flux with $G_{mean} = 50\mathrm{Kw/m^2}$, $G_A = 10\mathrm{Kw/m^2}$, $f = 0.1\,\mathrm{HZ}$ are shown in figure 3.17. The harmonic behavior in the surface temperature is sustained until burnout time. The

back wall surface temperature was not affected by the excited radiant heat exposure. It is expected that for a thermally thin sample, an oscillatory behavior would be observed at the back wall surface.

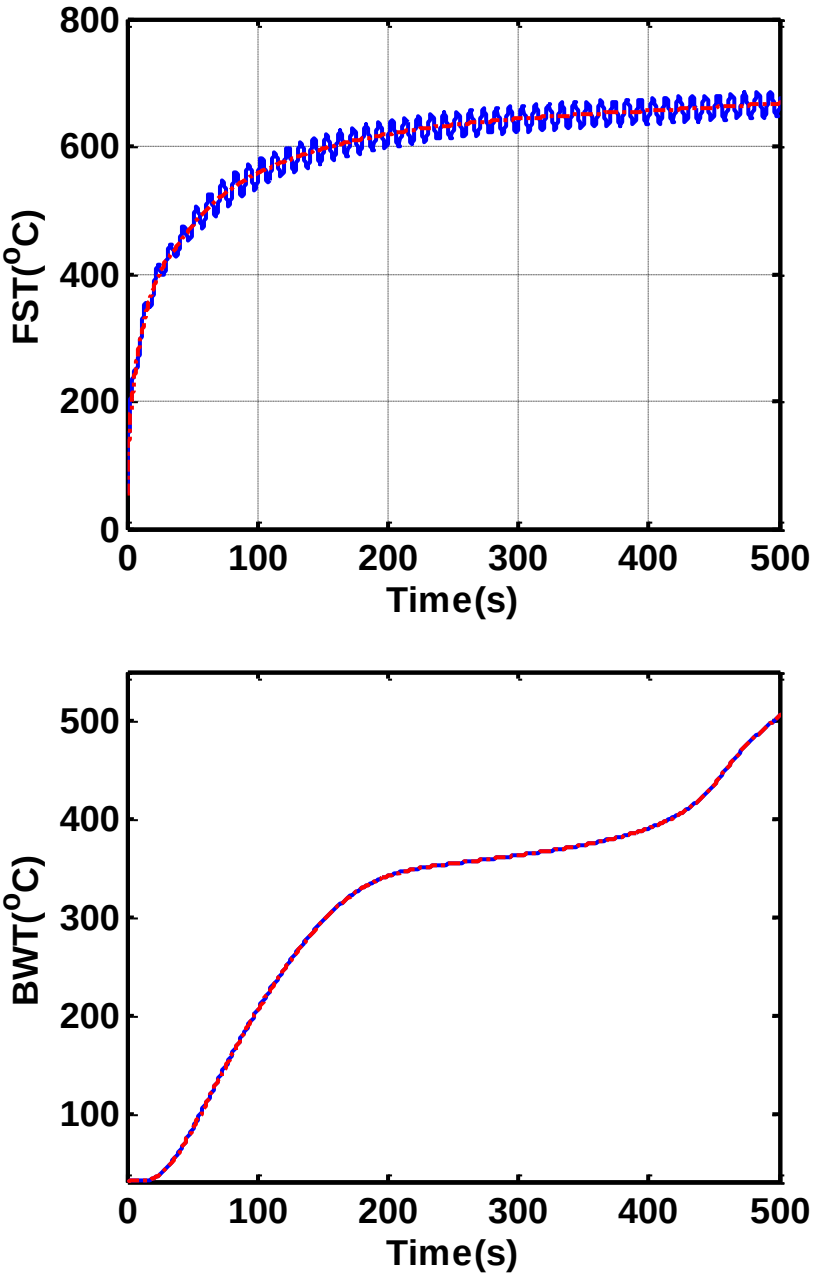

Figure 3-17. Time variation of the front surface temperature(top) and back surface temperature :Case of a 5mm PVC sample subjected to a constant (blue line) and time-varying (red dots) radiant heat flux.

Figure 3.18 shows the time histories of net heat flux for constant radiant heat flux, $G_{mean} = 50\text{kW/m}^2$, and harmonic radiant heat flux with an oscillatory amplitude of $G_A = 10\text{kW/m}^2$, and the difference of constant and oscillatory net heat flux, $q' = q - \bar{q}$. Notice, the peaks in the net heat flux contribute to a faster propagating pyrolysis wave penetrating through the sample and consequently leads in higher release of volatile (see Fig 3.16) in contrast with local minima of net heat flux where the value of MLR is lower.

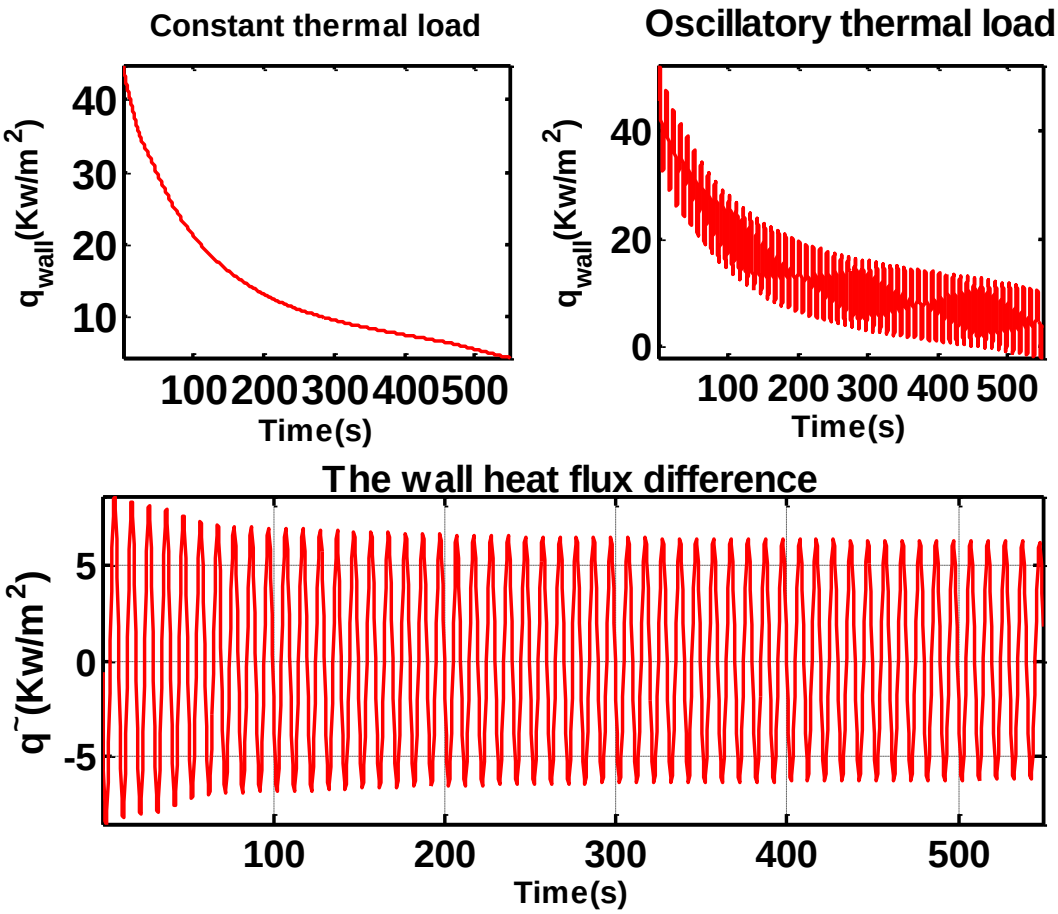

Figure 3-18. Time histories of net wall heat flux subjected to constant (top left), harmonic (top right), and their difference (bottom): Case of 5 mm PVC sample $G_{mean} = 50\text{kW/m}^2$, $G_A = 10\text{kW/m}^2$, $f = 0.1\,\text{Hz}$.

Figure 3.19 shows the reaction rate and temperature profile inside the PVC slab at 91 seconds for one cycle. The heat transferred from the radiation panel to the

surface of the PVC layer causes pyrolysis of PVC and hence forming a pyrolysis front moving inside the virgin material with time. As illustrated in the figure, the pyrolysis front propagating through the solid separates char from the virgin material. The oscillatory trend is observed in the traces of temperature profile and reaction rate. The temperature oscillation inside the solid is confined within a small region and does not penetrate throughout the PVC sample. The characteristic length scale, $l = \sqrt{2\alpha/\omega}$, for PVC sample is 0.53 mm and gives the distance at which oscillatory external heat flux takes place and consequently influences the behavior of both mass loss rate and temperature profiles. More precisely, as long as the pyrolysis front wave is inside of the reaction zone, the effect of oscillations in incident heat flux will be pronounced in the pyrolysis model calculation. In addition, profiles shown in figure 3.19 indicate that the position of the pyrolysis front, as an interface between char zone and virgin zone, and pyrolysis front thickness (pyrolysis zone) varies in time.

The temperature characteristics versus time and depth, and thus the burning characteristics during the pyrolysis process, depend on both the material characteristics and the external parameters. In the absence of char for the PMMA sample, the reaction zone remains close to the surface whereas the growing char layer formed a high thermal resistant layer between the front surface and the pyrolysis front wave, damping the thermal oscillatory wave propagating from the front surface toward virgin solid.

Figure 3.20 presents the time histories of the amplitude of surface fluctuation for an oscillation amplitude of 10 kW/m^2, frequency of 0.1 Hz, and four levels of mean radiative heat flux. The attenuation of the temperature oscillation is observed in the figure. The amplitude of oscillation shows a steady behavior at low levels of mean radiant heat flux ($G \leq 25\ kW/m^2$). At higher levels of heat flux, i.e., $G \geq 75\ kW/m^2$, the amplitude of surface temperature has the same decay rate. In addition, the amplitude of surface temperature is sensitive to oscillation amplitude. The reaction time scale is inversely proportional to the incoming heat flux; higher value of radiant heat flux

results in a faster reaction and thus the amplitude of surface temperature decreases whereas the MLR increases.

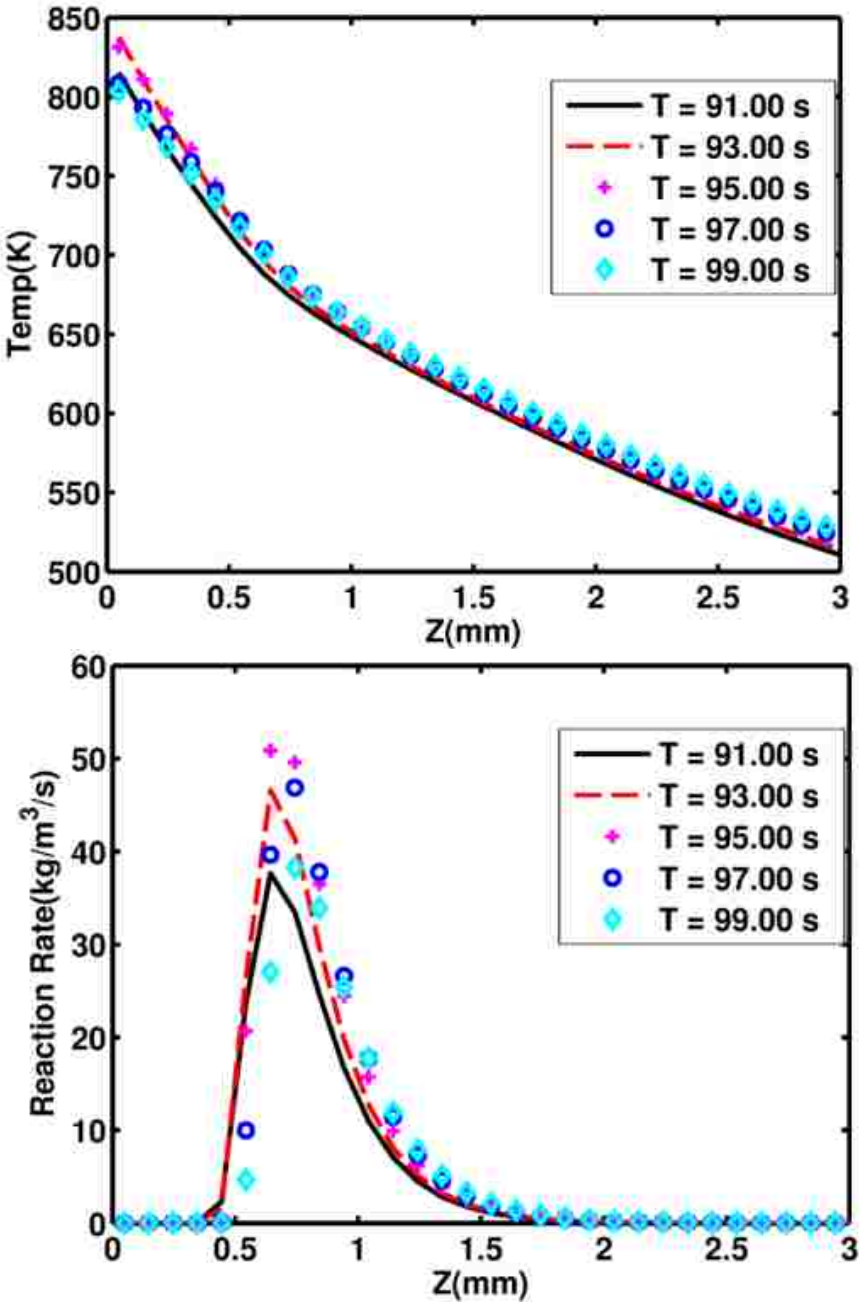

Figure 3-19. Temperature and reaction rate distribution inside solid sample subjected to harmonic radiation $G_{mean} = 50\text{kW/m}^2$, $G_A = 10\text{kW/m}^2$, $f = 0.1\,\text{Hz}$: Case of 5 mm PVC sample.

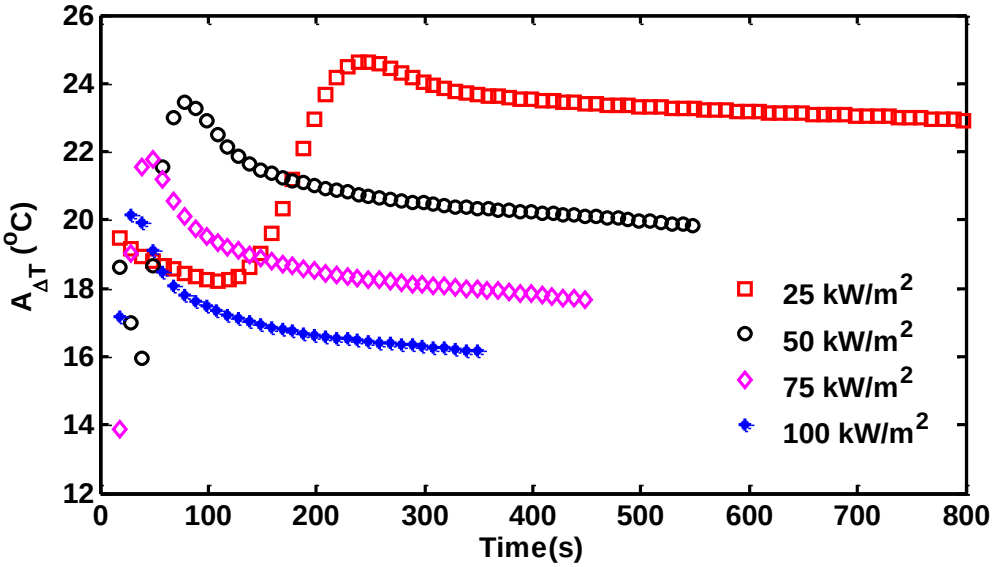

Figure 3-20. Time histories of the amplitude of surface temperature subjected to $G_A = 10\text{kW/m}^2$, $f = 0.1\,\text{Hz}$: Case of 5 mm PVC sample.

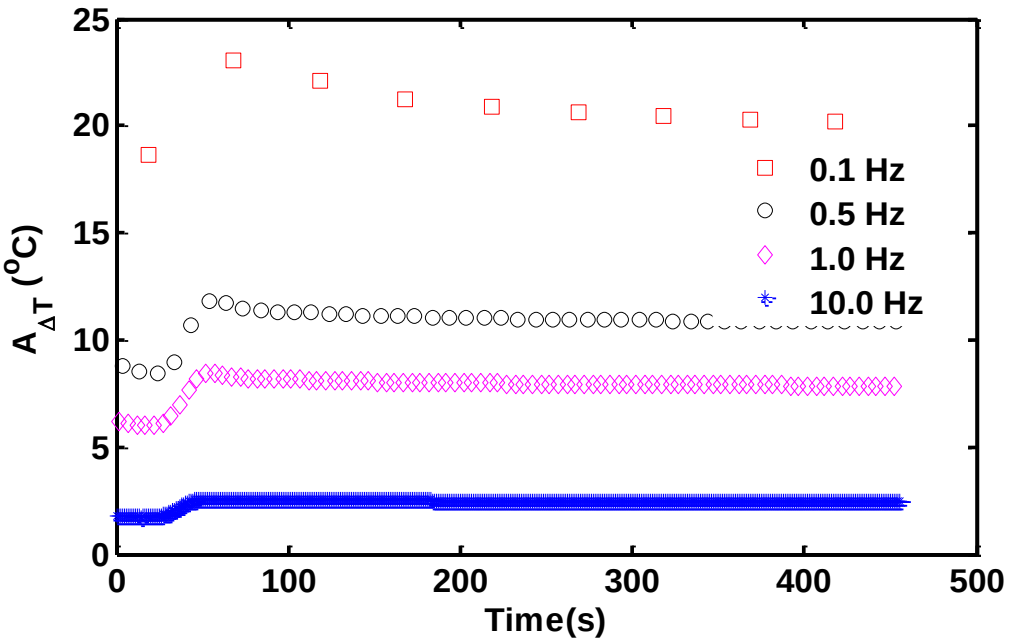

Figure 3-21. Time histories of the amplitude of surface temperature subjected to $G_{mean} = 50\text{kW/m}^2, G_A = 10\text{kW/m}^2$: Case of 5 mm PVC sample.

Figure 3.21 displays the effect of forcing frequency on the amplitude of surface temperature. The mean radiative heat flux and forcing irradiation amplitude are set to 50 kW/m^2 and $G_A = 10\text{kW/m}^2$ respectively. The magnitude of temperature oscillation shows a steady trend at an intermediate value of forcing frequency whereas it slightly changes with time at a low forcing frequency, i.e. $f = 0.1\text{Hz}$. As it was discussed before, the higher value of forcing radiant heat flux results in a higher amplitude of surface temperature while higher forcing frequency has an opposite effect. In addition, the variation in amplitude of surface temperature is consistent with that predicted by Eq. 9. The normalized error of amplitude predicted by the model and that of obtained by Eq. 9 is approximately 5% for the range of forcing frequency shown in figure 3.21.

Figure 3.22 shows the time histories of amplitude of MLR oscillation when the mean irradiation from panel is varied, while keeping the forcing irradiation amplitude and forcing frequency fixed. The attenuation of the MLR amplitude, i.e., the reduction in the magnitude of MLR fluctuation is observed before it reached the steady state. Note that the formation of the char acts like a thermal barrier and as a result the oscillation in the radiant panel will not propagate toward the solid sample. This effect of excitation in the radiant heat flux becomes negligible after MLR attain the second peak (or first peak for lower value of thermal load). Obviously, the effect of the lower net incoming heat is that surface temperature rises less rapidly. Consequently, the onset of pyrolysis occurs later. In addition, the pyrolysis gas mass flow rate in general decreases, as the front moves slower. The decay rate of amplitude of MLR fluctuation is higher at high value of mean radiant heat flux which is consistent with the results shown in figure 3.20.

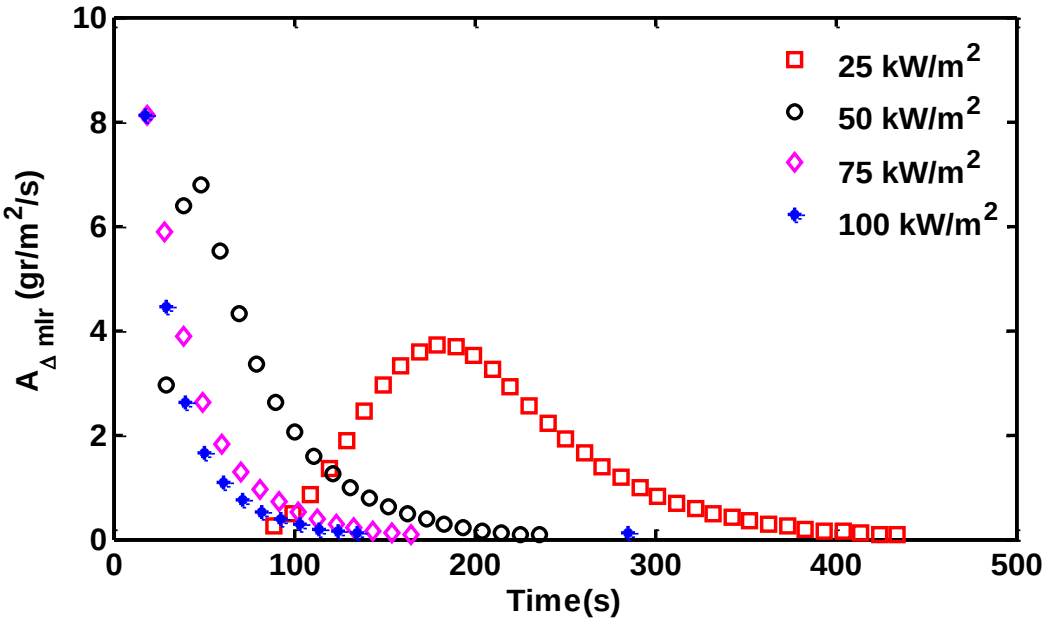

Figure 3-22. Time histories of amplitude of mass loss rate subjected to $G_A = 10\text{kW/m}^2$, $f = 0.1\,\text{Hz}$: Case of 5 mm PVC sample.

Figure 3.23 presents representative results in the form of a comparison between the amplitude of MLR fluctuation as a function of time at four levels of forcing frequency obtained with mean radiative heat flux of $G_{mean} = 50\text{kW/m}^2$ and forcing oscillatory heat flux of $G_A = 10\text{kW/m}^2$ .The figure reveals that the effect of oscillatory thermal load is less pronounced at the higher value of frequency. The periodic time scale, $t_p = \text{f}^{-1}$, is within the range of the chemical time scale, leading to less variation in the MLR fluctuation. In addition, the amplitude of MLR increases with higher oscillation amplitude of forcing radiant heat flux while keeping the forcing frequency constant. Within a cycle, higher forcing irradiation amplitude provides a higher value of thermal load at the maximum point and lower value of thermal load at the minimum point. That is, at the time during which the radiant heat flux attains the maxima, the extra heat result in rapid release of flammable vapor; on the other hand, at the time when it reaches the minima, the value of fuel release is lower, leading to a

higher value of amplitude of mass loss rate. Note that the magnitude of MLR oscillation decays with time before it reaches steady state.

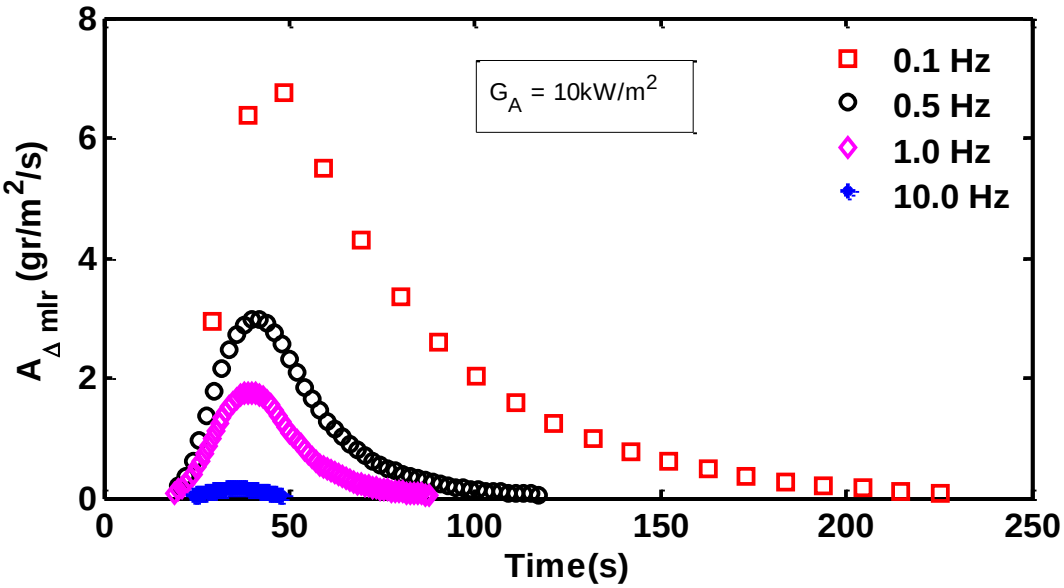

Figure 3-23. Time histories of the amplitude of oscillatory mass loss rate subjected to $G_{mean} = 50\text{kW/m}^2, G_A = 10\text{kW/m}^2$: Case of 5 mm PVC sample.

3.5 Conclusion

The general objective of the present study was to evaluate the pyrolysis process of both charring and non-charring material under a time-varying thermal load. The flammable solids considered for the present study were PMMA and PVC. A general pyrolysis model was developed based on conservation of mass, species and energy. The model allows for material shrinkage and transient thermal load. The pyrolysis parameters needed for pyrolysis modeling were estimated based on a genetic algorithm technique. A mathematical expression was developed based on a simple one dimensional heat equation to predict the fluctuation magnitude of the front surface temperature. A comparison of predictions made by the pyrolysis models under harmonic radiant exposure for PMMA and PVC was presented. The response in fuel mass loss rate and back wall temperature was different for each flammable material. In the case of PMMA, the effects of time-varying radiant exposure were pronounced during the entire pyrolysis process, from ignition to burn-out. In contrast,

in the case of PVC, the effects of time-varying radiant exposure were only pronounced during a limited time; this limited time corresponds to a regime in which the pyrolysis front is within a certain spatial distance of the exposed surface of the material. The analysis led to an evaluation of the importance of unsteady heat flux effects on pyrolysis processes.

Chapter 4 : Conclusion

Aircraft fire safety is the main concern of aircraft manufacturers and one of the major research topics that have been addressed to improve passenger safety. The growing use of composite material in the aviation industry has the potential to increase the fire hazard due to the flammable nature of these materials. Tremendous improvements in aircraft fire safety have been introduced during the last few decades. These efforts have contributed to a significant reduction in the number of accidents according to FAA data. However, further efforts in fire safety research are required in order to continue reducing the risk of fire related accidents. Aircraft manufacturers, together with the FAA, aim at improving fire safety requirements and have committed to long-term fire safety research, and to develop an efficient composite polymer matrix while keeping a balance between aircraft safety, economics and performance.

Advances in modern computing provide an excellent tool to assess the flammability of the composite polymers and the behavior of these materials in real fire scenarios. Computational Fluid Dynamics-based fire simulation presents a cost-effective alternative to expensive full-scale fire tests. It can also provide a fundamental understanding of material flammability and fire growth as opposed to conducting full-scale tests for every possible combination of test parameters and geometry. Moreover, CFD-based fire modeling may be used for forensic fire investigation. This allows the evaluation of the fire growth, and analysis of the impact of both the spread of fire hazards such as smoke, heat, and toxic gases as well as determining optimal procedure of the passenger evacuation.

Accurate prediction of the solid fuel mass loss rate is essential for CFD-based fire growth modeling because it determines the amount of gaseous fuel generated by the solid for the flames. Semi-empirical pyrolysis models are the dominant approach adopted in CFD-based modeling for modeling solid fuel. They consider simplified

descriptions of in-solid physical and chemical processes. In general, the pyrolysis model parameters are determined by finding the optimum agreement between the estimated model outputs, i.e. mass loss rate and temperature data, and the equivalent experimental value obtained from cone calorimeter test data.

In the present study, the limitations of current approaches in pyrolysis parameter estimation using optimization techniques are examined. Six semi-empirical model pyrolysis were developed to simulate the pyrolysis process of polyvinyl chloride (PVC). The parameter estimation approach is based on two optimization techniques– genetic algorithm and stochastic hill-climber algorithm. The six models provide similar mass loss rate predictions for conditions corresponding to calibration test data, i.e. high values of the radiation intensity, $G > 50$ kW/m^2, relatively thin samples, $L =$ 6 mm, and thermally insulated back surface conditions. The study then considers an evaluation of the predictive capability of the six pyrolysis models through a series of numerical experiments, including several cone calorimeter tests and one vertical (upward) flame spread problem. These configurations feature conditions that are significantly different from the reference conditions used in the model calibration phase. It is found that predictions from the PVC pyrolysis models start to diverge for conditions that lie outside of the calibration range. These results suggest that the domain of validity of semi-empirical pyrolysis models is limited to the conditions that were used during model calibration and that extrapolation to non-calibrated conditions may result in a significant loss of accuracy.

The thermal feedback from the flame is the driving mechanism of the pyrolysis process. In most fire scenarios, the flame grows in size and becomes turbulent. The influence of these turbulent fluctuations is pronounced on radiative heat flux and consequently the gas-to-solid rate of heat transfer features strong unsteady variations. As a result, the pyrolysis process takes place in a strongly unsteady environment. However, cone calorimeter test data are obtained using a constant incident heat flux and the unsteady aspect of the thermal load is neglected. The impact of an unsteady thermal load on the pyrolysis processes taking place inside solid flammable materials was examined in the present study. Harmonic periodic variations in irradiation

characterized by a mean value, an amplitude, and a frequency were considered. The responses of polymethyl methacrylate (PMMA) and polyvinyl chloride (PVC) samples were analyzed in terms of the amplitude of the fluctuations in both solid temperature and fuel mass loss rate. Results indicate that in a time-average sense, the oscillation in the incoming heat flux does not affect the rate of formation of flammable vapor. More precisely, the averaged mass loss rate under harmonic incident heat flux is approximately equal to averaged mass loss rate obtained under constant thermal load. Therefore the assumption of a constant incident heat flux in cone calorimeter experiments is valid. However, the timeline analysis of charring and non-charring materials response is quite different. In the case of PMMA, the effects of time-varying radiant exposure are pronounced during the entire pyrolysis process, from ignition to burn-out. In contrast, in the case of PVC, the effects of time-varying radiant exposure are only pronounced during a limited time. This limited time corresponds to a regime in which the pyrolysis front is within a certain spatial distance of the exposed surface of the material. The growing char layer formed a high thermal resistant layer between the front surface and the pyrolysis front wave, acting like a damper and diminishing the thermal oscillatory wave propagating from the front surface toward the solid slab. Additionally, a mathematical solution to a reference analog problem corresponding to heat conduction in a semi-infinite solid thermally loaded by an unsteady heat flux is used as the basis for data analysis. The analytical model was further modified to predict the amplitude of temperature and mass loss rate fluctuations for time dependent radiant exposure.

Appendix

G_A(kw/m2)	G_{mean} : 25 kw/m^2			
	f =0.1 Hz	f = 0.5 Hz	f =1Hz	f=10Hz
5:model	7.332	3.955	2.849	0.845
5:theory	8.636	4.020	2.864	0.876
10:model	14.642	7.905	5.698	1.689
10:theory	17.182	8.039	5.729	1.753
15:model	21.971	11.847	8.545	2.534
15:theory	25.770	12.051	8.592	2.750

Table A-1. The amplitude of surface temperature for $G_{mean} = 25\text{kWm}^2$: Case of 5 mm PMMA, theoretical value is shaded in gray.

G_A(kw/m2)	G_{mean} : 50 kw/m^2			
	f =0.1 Hz	f = 0.5 Hz	f =1Hz	f=10Hz
5:model	4.833	3.570	2.757	0.864
5:theory	8.653	3.979	2.737	0.996
10:model	9.671	7.084	5.482	1.729
10:theory	17.307	7.955	5.472	1.872
15:model	14.549	10.601	8.216	2.594
15:theory	25.962	11.932	8.199	2.747
20:model	19.600	14.120	10.947	3.460
20:theory	34.646	15.909	10.932	3.622

Table A-2. The amplitude of surface temperature for $G_{mean} = 50\text{kW/m}^2$: Case of 5 mm PMMA, theoretical value is shaded in gray.

G_A(kw/m2)	G_{mean} : 75 kw/m^2			
	f =0.1 Hz	f = 0.5 Hz	f =1Hz	f=10Hz
5:model	3.393	3.023	2.478	0.875
5:theory	8.733	3.973	2.720	0.995
10:model	6.900	5.961	4.940	1.750
10:theory	17.485	7.798	5.439	1.749
15:model	10.400	8.925	7.384	2.625
15:theory	26.226	11.681	8.158	2.623
20:model	cc	11.892	9.828	3.501
20:theory	34.965	15.448	10.878	3.497

Table A-3. The amplitude of surface temperature for $G_{mean} = 75\text{kW/m}^2$: Case of 5 mm PMMA, theoretical value is shaded in gray.

G_A(kw/m2)	G_{mean} : 100 kw/m^2			
	f =0.1 Hz	f = 0.5 Hz	f =1Hz	f=10Hz
5:model	2.650	2.508	2.275	0.876
5:theory	8.852	3.982	2.706	0.874
10:model	5.600	4.955	4.526	1.753
10:theory	17.705	7.964	5.412	1.747
15:model	8.500	7.700	6.634	2.631
15:theory	26.555	11.946	8.117	2.621
20:model	11.000	10.200	8.799	3.509
20:theory	35.433	15.928	10.823	3.494

Table A-4. The amplitude of surface temperature for $G_{mean} = 75 \text{kW/m}^2$: Case of 5 mm PMMA, theoretical value is shaded in gray.

G_A(kw/m2)	G_{mean}	
	25 kw/m^2	50 (kw/m^2
5:model	6.799442	4.2108
5:theory	8.745973	8.8289
10:model	13.6042	8.4449
10:theory	17.454	17.6697
15:model	20.458	12.7472
15:theory	26.1812	26.5032

Table A-5. The amplitude of surface temperature for $f = 0.1 \text{Hz}$: Case of 5 mm PMMA with h_p = 9 MJ/kg, theoretical value is shaded in gray.

G_A(kw/m2)	G_{mean} : 75 kw/m^2		
	f =0.1 Hz	f =0.5 Hz	f = 1.0 Hz
5:model	6.390	4.009	2.886
5:theory	8.210	3.921	2.820
10:model	12.495	8.003	5.773
10:theory	16.430	7.843	5.640
15:model	18.994	12.010	8.657
15:theory	24.652	11.764	8.460

G_A(kw/m2)	G_{mean} : 100 kw/m^2		
	f =0.1 Hz	f =0.5 Hz	f = 1.0 Hz
5:model	5.994	3.989	2.937
5:theory	8.322	3.891	2.714
10:model	11.955	7.966	5.870
10:theory	16.605	7.783	5.428
15:model	18.099	11.941	8.819
15:theory	25.102	11.675	8.142

Table A-6. The amplitude of surface temperature: Case of 50 mm PMMA with h_p = 0.9 kJ/kg, theoretical value is shaded in gray

Bibliography

[1] Surface Modelling for Composite Materials - SIAG GD – Retrieved at http://www.ifi.uio.no/siag/problems/grandine/

[2] Ilcewicz, L., Past Experiences and Future Trends for Composite Aircraft Structure, CS&TA Composites, FAA, Montana, 2009.

[3] Mouritz, A. P., Gibson, A. G., Fire Properties of Polymer Composite Materials, 3rd edition, Springer, 2006.

[4] R.E. Lyon, Fire-Resistant Materials: Progress Report, FAA report, DOT/FAA/AR-97/100, November 1998.

[5] The Aviation Maintenance Technician Handbook—Airframe, chapter 7, Department of Transportation, Federal Aviation Administration, Airman Testing Standards Branch, 2012.

[6] Lyon, R.E., Non-halogen fire-resistant plastics for aircraft interiors, Federal Aviation Administration, Springfield, VA 2008.

[7] Aircraft Materials Fire Test Handbook, Final Report DOT/FAA/AR-00/12, Federal Aviation Administration, April 2000.

[8] Troitzsch, J., Plastics Flammability Handbook: Principles, Regulations, Testing, and Approval, 3rd Edition, 2013.

[9] R.E. Lyon, Ranking Flammability of Aircraft Materials Using Microscale Combustion Calorimetry, FAA Seminar, 2005.

[10] R.E. Lyon, Fire-safe aircraft cabin materials. Fire and Polymers, ACS Symposium Series No. 599. G.L. Nelson, Washington DC: American Chemical Society, 1995, pp. 618-638.

[11] Federal Aviation Administration Fire research branch, http://www.fire.tc.faa.gov/research/

[12] T.R. Marker, Full-scale Fire Test Evaluation of Aircraft Fuel Fire Burnthrough Resistance Improvements, FAA-AR-98-52, 1999.

[13] R.G. Hill, G.R. Johnson and C.P. Sarkos. Post-crash fuel fire hazard measurements in wide-body aircraft cabin. FAA-NA-79-42.

[14] V. Babrauskas, Heat Release Rates, in The SFPE Handbook of Fire Protection Engineering (4th ed), P.J. DiNenno (ed), National Fire Protection Association, MA 02269, 2008, pp. 3-1-3-59.

[15] C. Di Blasi, Modeling and simulation of combustion processes of charring and non-charring solid fuels, Progress in Energy Combustion Science 19 (1993) 71-104.

[16] B., Moghtaderi, The state-of-the-art in pyrolysis modeling of lignocellulosic solid fuels, Fire and Materials 30 (2006) 1-34.

[17] C., Lautenberger, C., A generalized pyrolysis model for combustible solids, PhD Dissertation, University of California, Berkeley, CA (2007).

[18] C. Di Blasi, Modeling chemical and physical processes of wood and biomass pyrolysis, Progress in Energy Combustion Science 34 (2008) 47-90.

[19] C., Lautenberger, C. Fernandez-Pello, Pyrolysis modeling, thermal decomposition, and transport processes in combustible solids, in: M. Faghri, B. Sunden (Eds.), Transport Phenomena in Fires, WIT Press (2008) 209-259.

[20] C., Lautenberger, C. Fernandez-Pello, Generalized pyrolysis model for combustible solids, Fire Safety Journal 44 (2009) 819-839.

[21] S.I., Stoliarov, S., Crowley, R.E., Lyon, G. Linteris, Prediction of the burning rates of non-charring polymers, Combustion and Flame 156 (2009) 1068-1083.

[22] S.I., Stoliarov, S., Crowley, R.N., Walters, R.E., Lyon, Prediction of the burning rates of charring polymers, Combustion and Flame 157 (2010) 2024-2034.

[23] M., Chaos, M.M., Khan, N., Krishnamoorthy, J.L., de Ris, S., Dorofeev, Bench-scale flammability experiments: determination of material properties using pyrolysis models for use in CFD fire simulations, Interflam (2010) 697-708.

[24] S.R., Wasan, P., Rauwoens, J., Vierendeels, B., Merci, An enthalpy-based pyrolysis model for charring and non-charring materials in case of fire, Combustion and Flame 157 (2010) 715–734.

[25] M., Chaos, M.M., Khan, N., Krishnamoorthy, J.L., de Ris, S., Dorofeev, Evaluation of optimization schemes and determination of solid fuel properties for CFD fire models using bench-scale pyrolysis tests, Proceedings of the Combustion Institute 33 (2011) 2599-2606.

[26] C., Lautenberger, C. Fernandez-Pello, Optimization algorithms for material pyrolysis property estimation, Proceedings of the 10th International Symposium of Fire Safety Science, International Association for Fire Safety Science (2011) 583-595.

[27] A., Matala, S. Hostikka, Pyrolysis modeling of PVC cable materials, Proceedings of the 10th International Symposium of Fire Safety Science, International Association for Fire Safety Science (2011) 917-930.

[28] M., Chaos, M.M., Khan, S., Dorofeev, Pyrolysis of corrugated cardboard in inert and oxidative environments, Proceedings of the Combustion Institute 34 (2012), 2583-2590.

[29] P.A. Beaulieu, N.A. Dembsey, Effect of oxygen on flame heat flux in horizontal and vertical orientations, Fire Safety Journal 43 (2008) 410–428.

[30] G. T. Linteris. Numerical simulations of polymer pyrolysis rate: Effect of property variations, Fire and Materials (35) 463–480, 2011.

[31] A. Tewarson, Generation of Heat and Gaseous, Liquid, and Solid Products in Fires, in The SFPE Handbook of Fire Protection Engineering (4th ed), P.J. DiNenno (ed), National Fire Protection Association, MA 02269, 2008, pp. 3-109-3-194.

[32] C. Lautenberger, G. Rein, C. Fernandez-Pello, The application of a genetic algorithm to estimate material properties for fire modeling from bench-scale fire test data, Fire Safety Journal 41 (2006) 204-214.

[33] G. Rein, C. Lautenberger, C. Fernandez-Pello, J.L. Torero, D.L. Urban, Application of genetic algorithms and thermo-gravimetry to determine the kinetics of polyurethane foam in smoldering combustion, Combustion and Flame 146 (2006) 95-108.

[34] A., Matala, Estimation of solid phase reaction parameters for fire simulation, MS Thesis, University of Technology, Helsinki (2008).

[35] R., Webster, Pyrolysis model parameter optimization using a customized stochastic hill-climber algorithm and bench scale fire test data, MS Thesis, University of Maryland (2009).

[36] S.I., Stoliarov, N., Safronava, R.E., Lyon, The effect of variation in polymer properties on the rate of burning, Fire and Materials 33 (2009) 257–271.

[37] K., McGrattan, R., McDermott, S., Hostikka, S., and J. Floyd, Fire Dynamics Simulator (Version 5) users guide, NIST Special Publication 1019-5, National Institute of Standards and Technology, Gaithersburg, MD, 2010.

[38] National Institute of Standards and Technology, Fire Dynamics Simulator, *http://www.fire.nist.gov/fds/*

[39] P.K., Wu, L., Orloff, A., Tewarson, Assessment of material flammability with the FSG propagation model and laboratory test methods, in 13th Joint Panel Meeting of the UJNR Panel on Fire Research and Safety, NIST, Gaithersburg, MD, 1996.

[40] J.G. Quintiere, Fundamental of Fire Phenomena, John Wiley and Sons, Inc., 2006.

[41] Ghorbani, Z., Trouve, A., Webster, R., "Limitation in the Predictive Capability of Pyrolysis Model Based on a calibrated Semi-Empirical Approach", Fire Safety Journal, 61 (2013), pp. 274-288.

[42] Carslaw, H., Jaeger, J., Conduction of heat in Solids, second ed. Oxford University Press, 1959.